The

PHILOSOPHICAL MAGAZINE

FIRST PUBLISHED IN 1798

l. 2 Eighth Series No. 21 September 1957

A Journal of Theoretical Experimental and Applied Physics

PRICE £1 5s. 0d.
Annual Subscription £13 10s. 0d. payable in advance

ALERE FLAMMAM.
Printed and Published by
TAYLOR & FRANCIS LTD.
RED LION COURT, FLEET STREET, LONDON, E.C.4

The Charge Distribution of Multiply Charged Nuclei in the Primary Cosmic Radiation

Part I: The Light and Medium Nuclei†

By C. J. Waddington
H. H. Wills Physical Laboratory, Bristol

[Received June 20, 1957]

Abstract

The charge distribution of multiply charged nuclei in the cosmic radiation with charges of less than ten, has been investigated with a nuclear emulsion detector. The individual charges were determined by two independent methods of ionization measurement, δ-ray counting and blob-gap counting on the cores of tracks. The close similarity of the charge spectra obtained from these measurements provides an important check on the reliability of the charge determinations. The fluxes of nuclei of different charge groups are given, and it is shown that the ratio of light to medium nuclei at a mean depth in the atmosphere of 15 g/cm^2 is $0{\cdot}47 \pm 0{\cdot}07$, while at the top of the atmosphere it is $0{\cdot}37 \pm 0{\cdot}07$. These results are compared with those obtained by earlier workers. The use of charge indicating interactions in the calibration of the charge measurements is discussed in an Appendix.

§ 1. Introduction

Although it is nearly ten years since the existence of multiply charged nuclei in the primary cosmic radiation was demonstrated by Freier *et al.* (1948), the elucidation of the detailed features of the charge spectrum has proved surprisingly difficult. Previous experiments have been mainly concerned with the determination, at the top of the atmosphere, of the ratio of the abundance of lithium, beryllium and boron, the *L*-nuclei, to that of carbon, nitrogen, oxygen and fluorine, the *M*-nuclei, because of its importance in theories on the origin of cosmic radiation. Although a number of attempts have been made to determine this ratio, the quoted values have ranged from greater than unity to zero. In most of these experiments photographic emulsions were used as the detector, but counter arrays of various types have also been employed and have produced similarly conflicting results.

Owing to these disagreements it was decided to make a detailed investigation of the entire charge spectrum of cosmic ray nuclei. The present paper, called Part I, describes the results obtained on the relative

† Communicated by the Author.

abundances of L- and M-nuclei, while a later paper, Part II, will give those obtained on the charge distribution of heavier nuclei, the H-nuclei. Both these papers are based on data obtained from a single stack of photographic emulsions exposed at high altitude and at a geographic locality where the observed nuclei had relativistic velocities. Thus, the determination of charges depended only on a measurement of the ionization.

The ionization produced by the heavily charged nuclei was measured with a densitometer, and it will be shown in Part II that these measurements gave clear resolution between M- and H-nuclei. The ionization produced by the lighter nuclei was measured by delta-ray counting and by blob-gap counting on the core of the track. The comparison of the charges obtained by these two statistically independent methods provided an extensive check on the validity of the charge spectra.

Fig. 1

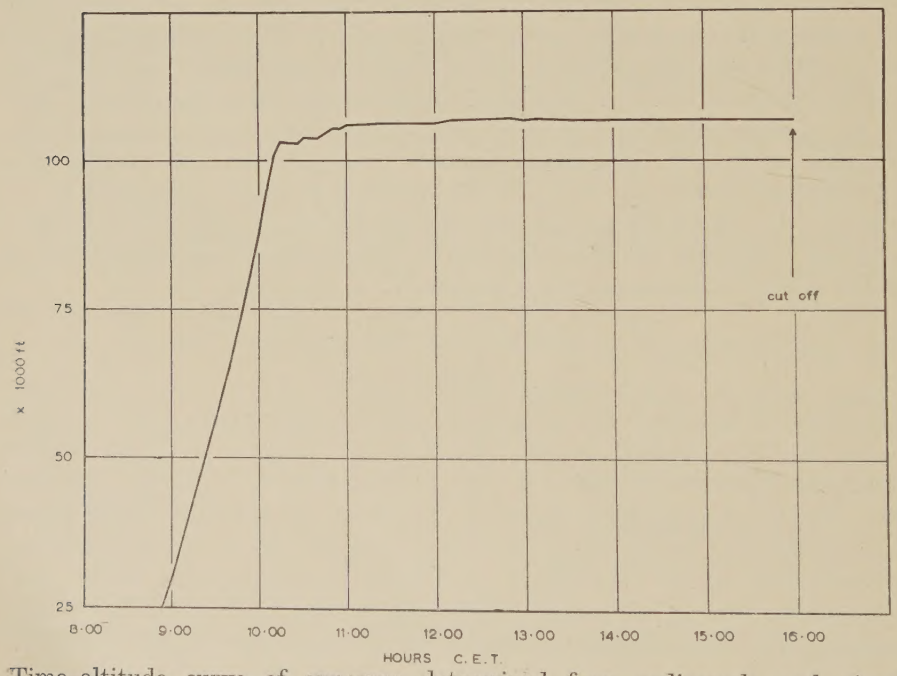

Time–altitude curve of exposure determined from radiosonde and visual observation.

§ 2. Stack and Exposure Details

The detector used in this experiment consisted of a stack of 80 stripped Ilford G5 nuclear emulsions measuring $20 \times 15 \times 0{\cdot}06$ cm, interleaved with single sheets of tissue paper. It was exposed, with the longer side vertical, over Northern Italy ($\lambda = 46°$N) on September 14, 1954, at a mean altitude of 106 000 feet. The time-altitude curve is shown in fig. 1.

From this curve it was estimated that approximately 6%, 8% and 10% of the observed H-, M- and L-nuclei had entered the stack while it was still rising to ceiling altitude, Waddington (1957).

The cut-off energy at the top of the atmosphere has been determined by Fowler and Waddington (1956) from measurements made in this stack, and shown to be $1{\cdot}55 \pm 0{\cdot}06$ Bev per nucleon. At such a cut-off energy less than 1% of the incident L- or M-nuclei which entered at ceiling had energies low enough to introduce any ambiguity in charges determined only from an ionization measurement. Although 10% to 20% of those L- and M- nuclei which entered the stack before it reached ceiling had lower energies, their presence was negligible when compared with the other uncertainties in the charge determinations.

§ 3. Detection of Particles

With the exception of two plates at each end of the stack, all plates were searched throughout their depth along a line parallel to, and one centimetre below the top edge, for tracks which satisfied the following criteria :

(i) The track should have a grain density greater than about seven times the minimum value as judged by a visual estimate.

(ii) The track should exceed a certain minimum length per plate. This length was varied from plate to plate, but was 2 mm in 49 emulsions, 4 mm in 14 and 6 mm in 13. Only those tracks longer than 6 mm per emulsion were considered in this experiment.

(iii) The track should have a zenith angle less than 75°. Only those tracks with zenith angles less than 60° were considered.

The scanning was done by trained observers, whose estimation of the minimum density acceptable was frequently checked. All tracks found were inspected and a visual estimate was made of the multiple scattering. In those few cases where this inspection did not clearly indicate the nature of the particle it was followed through several emulsions until definitely identified. All identified heavy nuclei with tracks longer than 4 mm per plate were then traced through the stack until they left, or interacted and were reduced to particles of charge two or less.

A total length of 907 cm was scanned in this manner. The same observers then re-examined 530 cm of this scanned length employing the same criteria as before, the minimum length accepted being kept constant at 3 mm per plate. These second scans were made, not on plates selected at random, but on those which, because of the lower number of background tracks found in them, were considered to have been less efficiently scanned. As a result, the corrections for scanning loss are somewhat uncertain, although, except for lithium nuclei, this uncertainty is not important, since no other nuclei had original detection efficiencies of less than 90%. The numbers of additional nuclei found

in these second scans are given in table 1, together with the numbers found in the first scan but not in the second. These figures show that the efficiency of the second scan was similar to that of the first. The suggested correction gives the limits arrived at by assuming that the detection efficiency was either 100% in those areas not rescanned, or the same as in the rescanned areas.

Table 1. Numbers of Particles found in One Scan but Not the Other

	Li	Be	B	C	N	O	F	$Z \geqslant 10$
Additional number found in second scan	5	1	2	2	2	1	0	0
Additional number found in first scan	3	0	2	1	0	0	0	0
Suggested correction	7–13	1–1·7	2–3·5	2–3·5	2–3·5	1–1·7	0	0

In making such a correction for scanning loss it is assumed that the missing of tracks is a purely random process and that all particles of a given charge are intrinsically as easy to detect. It may be objected that this assumption is not justified. For example, in emulsions, tracks near the glass are generally more difficult to detect than those near the surface, and short tracks are more likely to escape detection than long ones. However, the distributions in length and depth in the emulsions at which tracks were found have been determined for the L-nuclei, and show no evidence for any systematic missing. Therefore, it seems reasonable to assume, to a first approximation, that the missing of tracks was random and could be corrected for in the manner outlined above.

§ 4. Experimental Procedure

Measurements of charge made on the L- and M-nuclei found in this stack were as follows :

(i) A preliminary measurement of the δ-ray density was made on the tracks of all particles with a charge visually estimated to be less than ten.

(ii) Measurements of the blob-gap density were made on the tracks of all particles found from (i) to have a charge of seven or less.

(iii) Similar measurements were then made, in one half of the stack, on all the remaining tracks produced by particles which had a charge of less than ten from the densitometer measurements.

(iv) Careful δ-ray measurements were then made on the tracks of all particles with charges of less than eleven and more than four.

4.1. *Charge Determination From Blob-Gap Counts*

In order to make reliable measurements on the very dense cores of tracks caused by particles producing up to 64 times the minimum

ionization, the blob-gap method introduced by Fowler and Perkins (1955) has been employed. These authors found that a reliable parameter of the ionization produced by a particle, g, could be obtained by measuring the density of gaps H, with a length greater than a given length l, and the density of blobs B, where :—

$$g=\frac{1}{l}\ln\frac{B}{H}$$

and, that provided the number of blobs counted exceeded four times the number of gaps N_H :

$$\frac{dg}{g}=1/\sqrt{N_H}\ln B/H \quad \text{so that} \quad dg=1/l\sqrt{N_H}.$$

These authors showed experimentally that the value of g tended to a limit as Z, the charge, and thus the ionization, increased, and that this limiting value for g of about 5000 per mm was independent of the precise degree of development of the emulsion. Their results suggested that this limiting value should not be reached for a charge less than that of oxygen, and thus that there was a possibility of measuring the charges of L and M-nuclei.

Originally the blob-gap measurements were made on the tracks of those particles whose charges had been determined from the preliminary δ-ray counts to be seven or less, so that a practically unbiased sample of particles with charges of six or less was obtained. On each track 400 blobs and 100 gaps of length greater than 0·83 μ were counted. These measurements were made only in the central layers of the emulsions and in the majority of cases were made in at least two emulsions, thus reducing the possibility of a local fluctuation in the development seriously affecting the result. On some of the tracks it was impossible to count the full number of gaps and so the value obtained for g was of reduced statistical weight.

These measurements showed that the stack could be separated into two equal parts corresponding to development batches, which were distinguished by having different grain sizes. As a result, measurements on the tracks of particles of charge between seven and ten were made only in that half of the stack having the smaller grain size. This restriction was necessary owing to the inordinate length of track, greater than 3 cm, that would have been required in the other half.

The results of these and the earlier measurements are shown in fig. 2. In addition to a conventional histogram this figure also shows a smooth curve. This was obtained by representing each measurement as a triangle of constant area with a base width equal to twice the standard deviation. Such a method of representation assists in the appreciation of measurements of differing statistical weight. In order to compare the distribution obtained for the particles with charges of six and less with that obtained for those of higher charge, the latter have been increased by a factor of 1·87 to allow for the remaining unmeasured particles.

It should be noted that the possibility of the charge resolution obtained being the result of subjective 'pushing' of the measurements is not very great, since a knowledge of H or B alone is not sufficient to define the charge of the particle.

Fig. 2

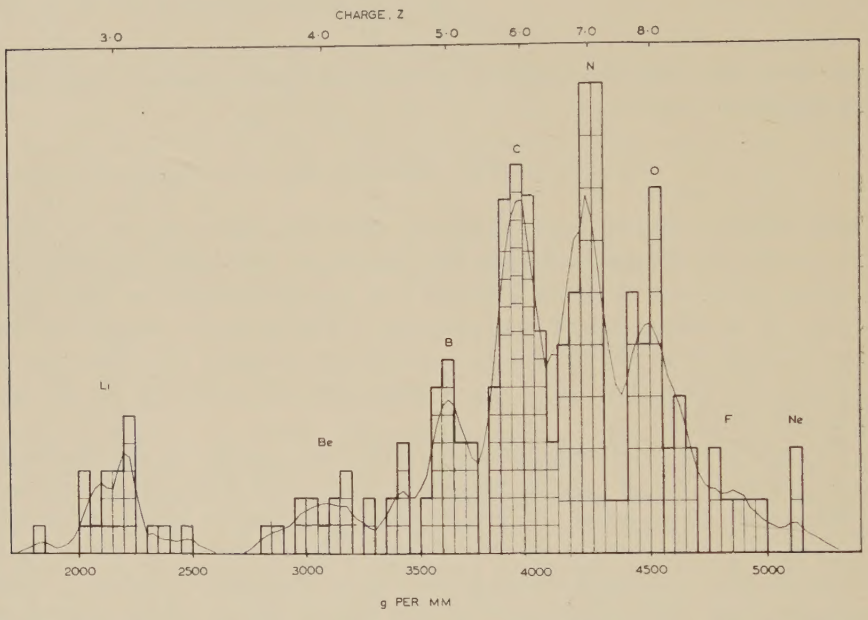

The distribution of blob-gap density, g, per mm. Those values of g greater than 4100 per mm have been increased by a factor of 1·87, as have a few with smaller values (see text).

4.2. *Charge Determination from Delta-Ray Counts*

In the present experiment, the convention employed required that a δ-ray should consist of four or more grains, since it was found that such a convention could be kept constant more readily than one which depended on the extension of the δ-ray from the track. In order to assist the maintenance of a consistent convention, measurements were confined to tracks having only a small range of δ-ray densities.

Careful measurements of the δ-ray density N_δ, were made on all the tracks of particles whose charges, as measured by the blob-gap counts, were between five and nine inclusive. In these measurements 100 δ-rays were counted on each track and great care was taken to verify that the counting convention did not change during the measurements. After every fifth track, a re-measurement was made on a track among the previous set of five. This re-measurement was made on the same portion of the track as before, and if it did not agree to within 5% of the original value the counting convention was adjusted and all five tracks in the set were re-counted. To check against a slow shift in the convention,

one of three standard tracks was re-measured after every set of ten, and once again, if there had been a greater than 5% change the entire group was re-measured. In practice, a stable convention was established relatively easily, so that re-measurement of sets of five or ten tracks was rarely necessary.

The results of these measurements are shown in fig. 3.

Fig. 3

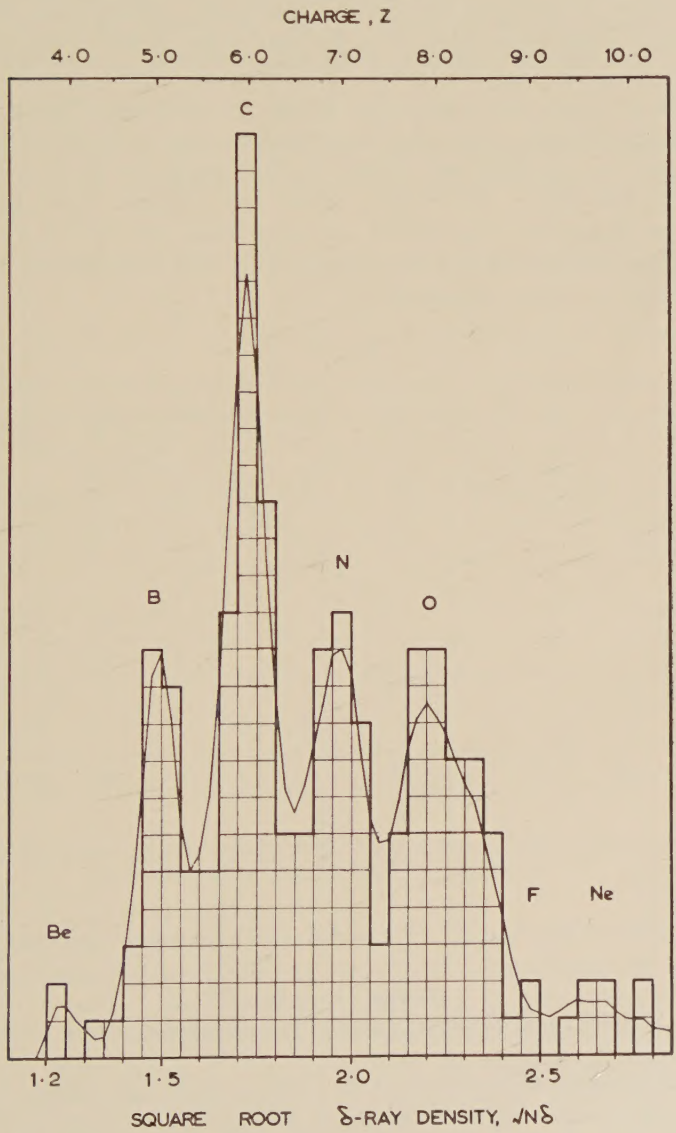

The distribution of the square root of the δ-ray density $\sqrt{N_\delta}$, for particles with a nominal charge between five and ten.

4.3. *Charge Calibration*

4.3.1. *Blob-gap measurements*

From measurements of the blob-gap density made on the tracks of singly charged primaries to ' jets ', the plateau value of g, g_0, was determined to be 234 ± 10 per mm. In a similar manner measurements made on tracks produced by α-particles with energies of greater than 5 Bev per nucleon, as measured by multiple scattering, gave $g_\alpha = 960 \pm 10$ per mm, and were constant throughout the stack. Hence over this range of ionization g was proportional to Z^2, and thus, if this proportionality was maintained to higher values, fast lithium nuclei should produce tracks with g about 2160 per mm. It can be seen from fig. 2 that the lightest group of tracks found in this experiment had $g = 2150 \pm 10$ per mm. Furthermore, no tracks were found of fast particles with values of g appreciably less than the above value, but greater than g_α. These tracks were therefore considered to have been produced by lithium nuclei. This identification was confirmed by the interactions produced by two of the particles (Appendix).

Fig. 4

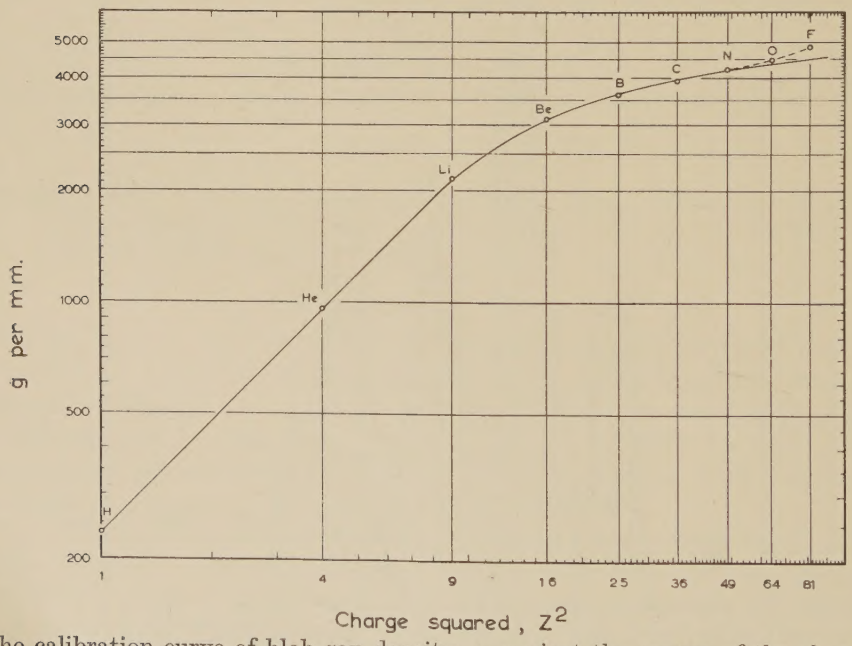

The calibration curve of blob-gap density, g, against the square of the charge.

If it is assumed that particles of all charges up to the highest measured were present in the sample considered, and fall in resolved peaks, then, since the charge of the lowest peak in the g distribution has been determined, those of the other peaks may be assigned. A calibration curve based on this assumption is shown in fig. 4. The regular form of this

curve as far as oxygen is supporting evidence for the above assumption, as are the interactions produced by some of the particles. In particular the position of the carbon peak is confirmed by two particles which produce interactions from which only α-particles are emitted (Appendix).

4.3.2. *Delta-ray measurements*

Measurement of the δ-ray density on the tracks of those two particles which were identified as lithium nuclei from their interactions, gave $N_\delta(\mathrm{Li})=1{\cdot}10\pm0{\cdot}05$ δ-rays per $100\,\mu$. Similar measurements on the tracks of those two particles which were identified as carbon nuclei from

Fig. 5

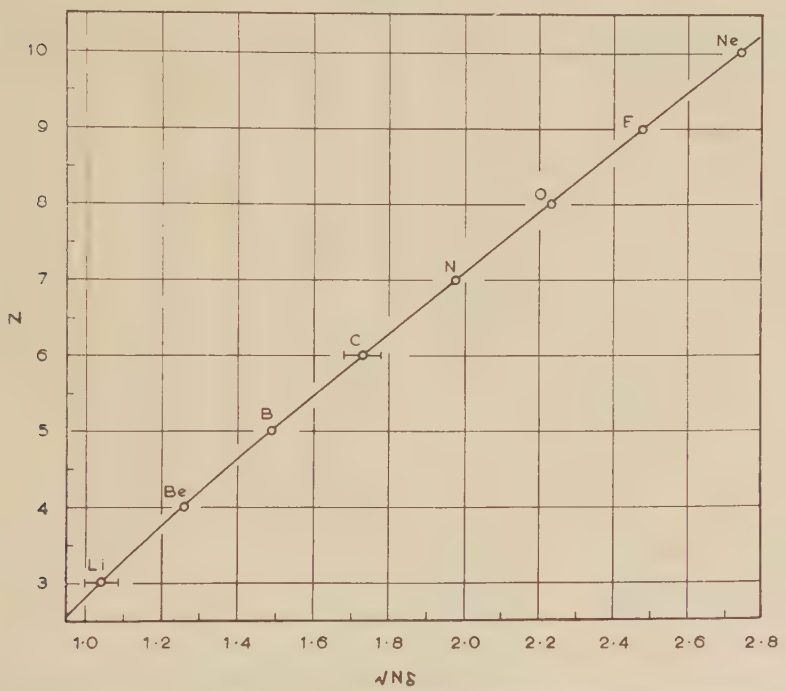

The calibration curve of the square root of the δ-ray density against the charge, from the relation $Z=3{\cdot}76(N_\delta-0{\cdot}46)^{1/2}$.

their interactions gave $N_\delta(\mathrm{C})=3{\cdot}00\pm0{\cdot}07$ δ-rays per $100\,\mu$. Thus, when the relation between the δ-ray density and the charge was expressed in the form $Z=a(N_\delta-b)^{1/2}$, a and b equalled $3{\cdot}76\pm0{\cdot}11$ and $0{\cdot}46\pm0{\cdot}07$ respectively. The calibration curve derived from this relation is shown in fig. 5. A comparison of this curve with the data displayed in fig. 3 shows the close agreement between the positions of the observed peaks and the predicted values from the above relation; at least as far as oxygen, although the position of the higher charge peaks are not well defined.

4.4. *Comparison of Charge Determinations*

The determinations of the δ-ray density were made after those of the blob-gap density, and particular care was taken to ensure that *the precise charge as determined from the blob-gap density was unknown while the δ-ray density was being measured*, although, of course, it was known that the particles being measured had charges of between ten and five. Thus, any agreement between the charges determined by these two methods can hardly be attributed to the subjective influence of a knowledge of the first charge determination, but must represent the agreement of two independent charge determinations.

Fig. 6

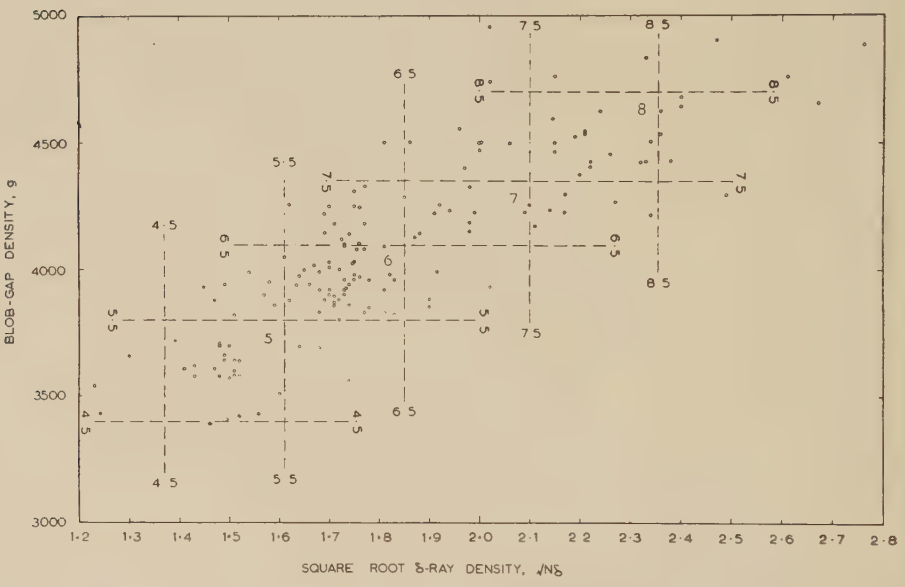

The comparison of $\sqrt{N_\delta}$ with g. The dashed lines represent values of half integral charge (see text).

In all there were 153 tracks on which both g and N_δ were measured. The comparison of these values is shown in fig. 6, which is a plot of the blob-gap density against the square root of the δ-ray density. The dashed lines shown on this figure are the values of g and $\sqrt{N_\delta}$ corresponding to half integral charges. Those points that lie inside the completed squares bounded by these lines represent tracks on which both measurements gave the same integral charges. Owing to the breakdown of the charge calibration curves at charges of greater than eight, in this comparison points with an apparent charge greater than 8·5 by either determination have been neglected. Out of the remaining 139 particles, 90 gave the same integral charge in both determinations, 48 changed by one charge, and 1 changed by two charges.

As a further illustration of the agreement between these results fig. 7 shows a histogram of the difference between the charge determined from the blob-gap measurements Z_g, and that determined from the δ-ray measurements Z_δ. From this plot of $Z_g - Z_\delta$ the standard deviation of an individual charge determination was found to be about half a charge, compared with the value of about a third of a charge derived from the widths of the peaks in the two charge spectra. There is a slight indication of a systematic difference in the charge values, the ratio of positive to negative values of $Z_g - Z_\delta$ being 1·29, but examination of fig. 6 shows that this is primarily due to differences within the M group of nuclei. It will be seen later, table 2, that the L/M ratios determined from δ-counting and blob-gap counting differ by less than 10%.

Fig. 7

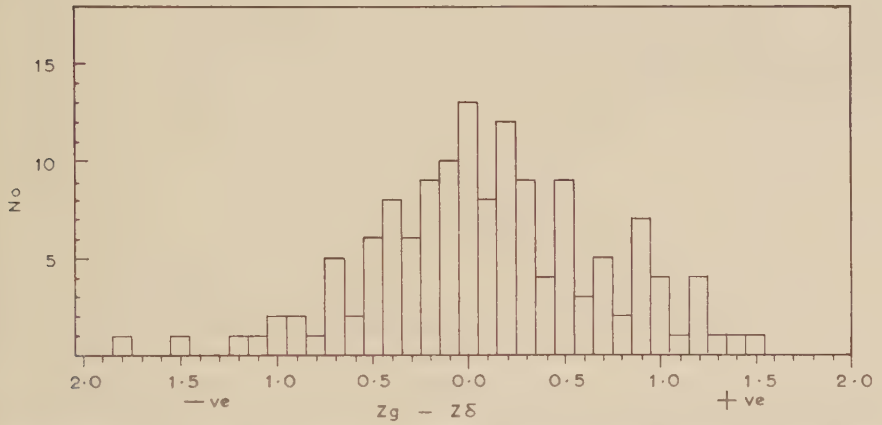

Histogram of $Z_g - Z_\delta$ for those particles on which both g and N_δ had been measured.

§ 5. Results

The number of particles of each charge determined by the two measurements are shown in table 2, in which the actual numbers of tracks on which the blob-gap density was measured are given in brackets. This table shows that the greatest discrepancy between the two charge distributions was for nitrogen nuclei, and that the difference between the total

Table 2. Numbers of Particles found from δ-Ray Counts N_δ, and Blob-gap Counts N_g

	Li	Be	B	C	N	O	F	$Z \geqslant 10$†
N_δ	20	18	30	64	41	48	9	45
N_g	20	15	29	56 (53)	54 (28)	46 (24)	10 (6)	45
$\overline{N}$	20	16·5	29·5	60	47·5	47	9·5	45

† From densitometer measurements.

numbers of L- and M-nuclei was negligible. Thus, since for no charge does taking the mean number $\overline{N}$, introduced a systematic error which is greater than the statistical uncertainty, the means have been used in calculating the fluxes. From these means, plus the correction for scanning loss (§ 3), there were subtracted those particles which entered the stack while it was rising to ceiling altitude (§ 2).

The flux of particles observed to cross the scanned area of the emulsions is given by :

$$J_n x = \frac{N}{ta\gamma} \cdot \frac{\int_0^{\theta_{\max}} \sec\theta \, d\theta}{\int_0^{\theta_{\max}} d\theta} = 2{\cdot}67 \ 10^{-2} N \text{ particles/m}^2 \text{ ster sec}$$

where N is the total number of particles of type n crossing a detecting area a, t is the time of exposure in seconds, γ is the solid angle of collection, θ is the zenith angle and $J_n x$ is the flux of n-type particles at a depth in the atmosphere of x g/cm^2.

Thus, making the maximum correction for scanning loss, the fluxes observed in the emulsions were :

$$J_L x = 2{\cdot}02 \pm 0{\cdot}24 \text{ particles/m}^2 \text{ ster sec}$$
$$J_M x = 4{\cdot}29 \pm 0{\cdot}33 \text{ particles/m}^2 \text{ ster sec}$$
$$J_H x = 1{\cdot}14 \pm 0{\cdot}17 \text{ particles/m}^2 \text{ ster sec}$$

and therefore $J_L x / J_M x = 0{\cdot}47 \pm 0{\cdot}07$. However, the densitometer measurements were actually made on all tracks longer than 4 mm per plate, and 74 particles of charge ten or greater were observed. As a result the value taken for the flux of H-nuclei in the emulsions was $1{\cdot}35 \pm 0{\cdot}16$ particles/m^2 ster sec.

These flux values have been extrapolated to the top of the atmosphere through 4·8 g/cm^2 of emulsion and 12 g/cm^2 of air and packing material—cardboard and aluminium. To make this extrapolation the diffusion equations given by Kaplon *et al.* (1954) for a parallel beam of nuclei suffering no ionization loss, have been used, together with the fragmentation probabilities and mean free paths found in this stack by Fowler *et al.* (1957). In making this extrapolation the errors in the flux values and those quoted for the fragmentation probabilities have been propagated through the calculations. The resulting flux values at the top of the atmosphere were :

$$J_{L^\circ} = 2{\cdot}3 \pm 0{\cdot}4 \text{ particles/m}^2 \text{ ster sec}$$
$$J_{M^\circ} = 6{\cdot}1 \pm 0{\cdot}6 \text{ particles/m}^2 \text{ ster sec}$$
$$J_{H^\circ} = 2{\cdot}5 \pm 0{\cdot}3 \text{ particles/m}^2 \text{ ster sec}$$

and therefore :

$$J_{L^\circ}/J_{M^\circ} = 0{\cdot}37 \pm 0{\cdot}07 \text{ and } J_{H^\circ}/J_{M^\circ} = 0{\cdot}41 \pm 0{\cdot}06.$$

It should be noted that the above value of J_{L° and thus that of J_{L°/J_{M°, is very dependent on what values are assumed for the fragmentation

probabilities. For example, if the values reported by Noon and Kaplon (1955) had been used instead of those found in this laboratory, then J_{L^0} would be about zero, although J_{M^0} and J_{H^0} would hardly be affected. However, the values quoted by Fowler *et al.* (1957) for these parameters in air are believed to be upper limits, and thus, if this is correct, J_{L^0} is unlikely to be less than the value quoted.

§ 6. Discussion

Since the α-particle flux derived from measurements in this stack of emulsions is not significantly different from that observed over America at a geomagnetic latitude of 41°N, (Fowler and Waddington 1956), the fluxes of heavy nuclei determined in this experiment should be comparable with those obtained at the above locality. The values for the M- and H-nuclei are shown in table 3 and are in good agreement.

Table 3. Fluxes at the Top of the Atmosphere of M- and H-nuclei Observed at a cut-off Energy of about 1·5 Bev per Nucleon

Reference	J_{M^0} particles/m² ster sec	J_{H^0} particles/m² ster sec	Detector
Kaplon *et al.* (1952)	$5{\cdot}3 \pm 0{\cdot}6$†	$2{\cdot}2 \pm 0{\cdot}3$†	Emulsions
Kaplon *et al.* (1954)	$5{\cdot}9 \pm 1{\cdot}1$†‡	$2{\cdot}9 \pm 1{\cdot}0$†‡	Emulsions
Noon *et al.* (1957)	$5{\cdot}1 \pm 0{\cdot}8$	$3{\cdot}0 \pm 0{\cdot}6$‡	Emulsions
This expt.	$6{\cdot}1 \pm 0{\cdot}6$	$2{\cdot}5 \pm 0{\cdot}3$	Emulsions
Stix (1954)	$10{\cdot}2^{+4{\cdot}5}_{-3{\cdot}5}$		Cloud chamber
Linsley (1956)	$7{\cdot}4 \pm 1{\cdot}7^{\alpha}$	$4{\cdot}2 \pm 2{\cdot}0$	Cloud chamber and Cerenkov counter
Webber (1956)	$9{\cdot}2 \pm 1{\cdot}2$		Cerenkov counter

† Corrected for particles entering during ascent.

‡ Corrected to place neon in H-group, assuming flux of neon is 8% that of M-nuclei from data in present experiment.

$\alpha = 6 \leqslant Z \leqslant 8$.

However, there is no such agreement between the reported values of the ratio of L- and M-nuclei. Nor indeed is there agreement between the detailed features of the charge distribution within the M group of nuclei. These details are shown in table 4, in which the number of particles of each charge, as measured in eight different experiments, are represented as fractions of the total number of M plus boron nuclei observed in that experiment.

These charge spectra have been measured at depths in the atmosphere which ranged from 32 g/cm², Fay (1955) to 12 g/cm², Noon *et al.* (1957), and it is not at once apparent that they are directly comparable. Moreover, insufficient is known of the detailed diffusion parameters to permit

Table 4. Relative Frequencies of Different Nuclei, expressed as a Fraction of the Total Number of M plus Boron Nuclei observed in the Experiment

	Author	Depth g/cm²	Probable cut-off energy Bev/nucleon	Li	Li (corr)	Be	Be (corr)	B	C	N	O	F	$Z \geqslant 10$
1	Fay (1955)†	32	~ 2·3	0·13 ±0·05	0·26 ±0·10	0·21 ±0·06	0·26 ±0·08	0·48 ±0·11	0·24 ±0·07	0·16 ±0·05	0·06 ±0·03	0·05 ±0·03	0·16 ±0·05
2	Kaplon *et al.* (1954) I	30	1·5	0·21 ±0·06	—	0·20 ±0·06	—	0·14 ±0·05	0·38 ±0·09	0·21 ±0·06	0·24 ±0·07	0·03 ±0·02	0·14 ±0·05
3	Kaplon *et al.* (1954) II	21	⩽0·15	0·27 ±0·10	—	0·19 ±0·08	—	0·27 ±0·10	0·27 ±0·10	0·32 ±0·10	0·14 ±0·07	0·05 ±0·03	0·16 ±0·07
4	Bradt and Peters (1950)	20	1·5	0·04 ±0·03	—	0·06 ±0·03	—	0·07 ±0·04	0·39 ±0·10	0·09 ±0·04	0·37 ±0·10	0·07 ±0·04	0·25 ±0·10
5 (*a*)	Dainton *et al.* (1952) I	19	⩽0·15	0·12 ±0·03	0·36 ±0·09	0·24 ±0·04	—	0·36 ±0·06	0·29 ±0·06	0·19 ±0·05	0·10 ±0·04	0·05 ±0·02	0·15 ±0·04
(*b*)	II	30	⩽0·15	0·10 ±0·03	0·40 ±0·12	0·25 ±0·05	—	0·40 ±0·06	0·29 ±0·05	0·17 ±0·04	0·11 ±0·03	0·03 ±0·02	0·12 ±0·03
6	Webber (1956)‡	18·5	1·5	—	0·23 ±0·04	—	0·30 ±0·05	0·15 ±0·03	—	0·85±0·10		—	0·30 ±0·05
7	Noon *et al.* (1957)	12	1·5	0·03 ±0·02	0·08 ±0·06	0·14 ±0·05	—	0·42 ±0·09	0·41 ±0·09	0·04 ±0·02	0·08 ±0·04	0·04 ±0·02	0·31 ±0·08
8 (*a*)	This expt. I	15	1·5	0·10 ±0·02	0·16 ±0·03	0·08 ±0·02	0·09 ±0·02	0·16 ±0·04	0·31 ±0·04	0·25 ±0·04	0·24 ±0·04	0·05 ±0·02	0·22 ±0·04
(*b*)	II	15+23 of emul. (30)	1·5	0·14 ±0·04	—	0·09 ±0·03	—	0·16 ±0·04	0·34 ±0·07	0·24 ±0·05	0·23 ±0·05	0·04 ±0·02	0·22 ±0·05

† Only zenith angles between 0°–60° included, due to postulated local matter over emulsions for zenith angles less than 0°.
‡ Cerenkov counter, assuming that J_H/J_M at this depth is 0·26 from data in present experiment.

an extrapolation of individual charges to a standard depth. For this reason the spectrum of Dainton *et al.* (1952) at a mean depth of 19 g/cm² is compared with the independent spectrum obtained by the same authors in the same experiment at 30 g/cm² ; and the distribution obtained in the present experiment is compared with that observed lower in the same stack of emulsions. This second distribution was obtained by finding the charge spectrum of those nuclei which crossed a hypothetical scan line 6 cm below the original scan line on which the nuclei, or their parents, were detected. A comparison of these distributions shows that the passage of particles through this amount of matter does not appreciably change the charge spectrum, and that it is, therefore, permissible to make a direct comparison of the various spectra.

Fig. 8

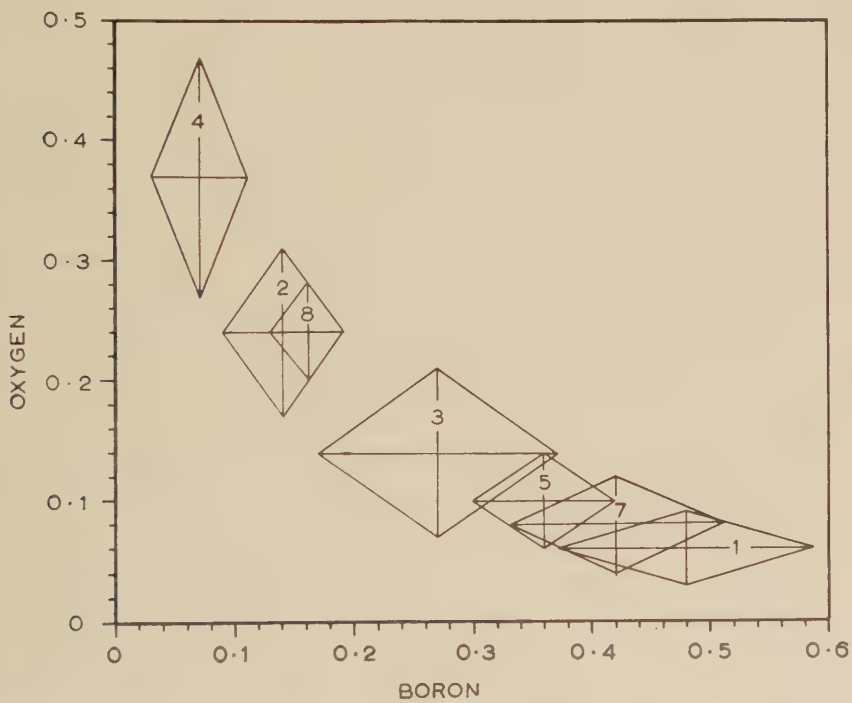

Relative abundance of oxygen against that of boron as observed in seven different experiments. The sizes of the standard deviations are shown. For references see table 4.

Certain features are at once apparent. With the exception of fluorine and the *H*-nuclei, the frequencies of the different nuclei fluctuate far more than could be expected on a purely statistical basis. These fluctuations are exemplified in fig. 8, which shows the frequency of oxygen nuclei as a function of that of boron nuclei. It can be seen from this figure that the total frequency of oxygen plus boron is roughly constant,

but that the individual frequencies vary widely. This observation suggests that many workers must have made serious errors in the charge determinations within the charge region from five to eight. It is plausible that if there should be such errors they would occur within this range of charges, since in emulsion work lithium and beryllium nuclei are comparatively easy to identify, while errors of one charge between oxygen and neon will not be serious due to the low abundance of fluorine. In some of the experiments the resolution obtained between nuclei of different charges was as good as, or even better than, that obtained in the present experiment, although only in this experiment were the majority of charges determined by two different methods. It must be accepted, therefore, that in some of these experiments the apparent charge resolution is spurious, and is due to the subjective nature of the measurements. There must either have been a consistent ' pushing-down ' of the measured charges, or a similar ' pushing-up '. It is difficult to see how such a process can have occurred in some of the earlier experiments, but it is doubly difficult to imagine such a process occurring in the present experiment with its two independent sets of charge determinations. It therefore appears that experiments where the charge determinations were not checked in this manner may be seriously in error.

It must be admitted that the assumption that some, at least, of the earlier experiments give radically incorrect charge spectra is only justified by the almost complete inconceivability of variations with time existing in the charge distribution of the primary cosmic radiation. If a model which predicted such variations could be constructed the experimental results displayed in table 4 would represent strong evidence in its favour.

Acknowledgments

The author is grateful to Professor C. F. Powell, F.R.S., for affording him the hospitality and facilities of his laboratory, and to R. R. Hillier for helpful discussions on specific points. He acknowledges with gratitude the valuable help rendered by the observers, Miss B. Bolt, Mrs. A. Boult, Mrs. H. Burrows, Miss P. Curry and Miss C. Rothwell, without whose careful scanning this experiment would have been impossible. The assistance of his wife in the presentation of this paper must also be acknowledged with gratitude. Finally he must thank the Royal Society for the award of a Mackinnon Research Studentship.

References

Appa Rao, M. V. K., Daniel, R. R., and Neelakontan, K. A., 1956, *Proc. Ind. Acad.*, **43,** 181.

Bradt, H. L., and Beters, B., 1950, *Phys. Rev.*, **80,** 943.

Dainton, A. D., Fowler, P. H., and Kent, D. W., 1952, *Phil. Mag.*, **43,** 729.

Fay ,H., 1955, *Z. Naturf.*, **10a,** 572.

Fowler, P. H., Hillier, R. R., and Waddington, C. J., 1957, *Phil. Mag.*, **2,** 293.

Fowler, P. H., and Perkins, D. H., 1955, *Phil. Mag.*, **46**, 587.
Fowler, P. H., and Waddington, C. J., 1956, *Phil. Mag.*, **1**, 637.
Freier, P., Lofgren, E. J., Ney, E. P., Oppenheimer, F., Bradt, H. L., and Peters, B., 1948, *Phys. Rev.*, **74**, 213.
Kaplon, M. F., Noon, J. H., and Racette, G. W., 1954, *Phys. Rev.*, **96**, 1408.
Kaplon, M. F., Peters, B., Reynolds, H. L., and Ritson, D. M., 1952, *Phys. Rev.*, **85**, 295.
Linsley, J., 1956, *Phys. Rev.*, **101**, 826.
Noon, J. H., Hertz, A. J., and O'Brien, B. J., 1957, *Nuovo Cimento*, **5**, 854.
Noon, J. H., and Kaplon, M. F., 1955, *Phys. Rev.*, **97**, 769.
Perkins, D. H., 1949, *Phil. Mag.*, **41**, 138.
Stix, T. H., 1954, *Phys. Rev.*, **95**, 782.
Waddington, C. J., 1957, *Nuovo Cimento* (in the press).
Webber, W. R., 1956, *Nuovo Cimento*, **4**, 1285.

APPENDIX

Charge Indicating Interactions

In its passage through the emulsion a heavy particle may interact with a free proton or a peripheral nucleon. In such interactions there will in general be at most one slow singly charged particle emitted ($N_h \leqslant 1$). Furthermore, all the constituant particles of the incoming nucleus should appear among the secondary products, and its charge should be given by the sum of the charges of these particles. Unfortunately, it is usually impossible to make a clear distinction between the singly charged particles belonging to the incoming nucleus, mesons produced in the interaction and the recoiling nucleon. As a result, the charge of the incident nucleus is well defined only when all the fast fragments are multiply charged, and even in such interactions the possibility of unlikely processes cannot be completely neglected.

Events of this type are, in any case, rare ; so, to increase the number of charge indicating interactions, an analysis has been made of a number of interactions in which $N_h \leqslant 1$. The angular distribution of the singly charged particles emitted from these disintegrations is shown in fig. 9. The data from which this distribution was obtained was the result of measurements made on 73 such interactions observed in this stack and another exposed under very closely similar conditions. These interactions were considered only if they were at least $30\,\mu$ away from an interface of the emulsion, and were so situated that the track of the incident nucleus extended at least $500\,\mu$ in the emulsions, and had a potential range of at least $500\,\mu$ after the interaction.

This angular distribution is similar in form to that observed by Appa Rao *et al.* (1956) from an examination of disintegrations produced by α-particles, and may be interpreted in a similar manner. The mesons

produced in these interactions will be emitted isotropically in the C-system of the interaction, and thus, at the mean energy of the nuclei incident on this stack, the number of particles per unit solid angle observed in the L-system should be approximately constant for small angles. Hence the large peak in the angular distribution at small angles must be due to protons from the incident nucleus. If the angular distribution of these protons is considered to be that represented in fig. 9 by the line marked p, then the r.m.s. angle of emission is $2{\cdot}0\pm0{\cdot}12°$, and, assuming that the

Fig. 9

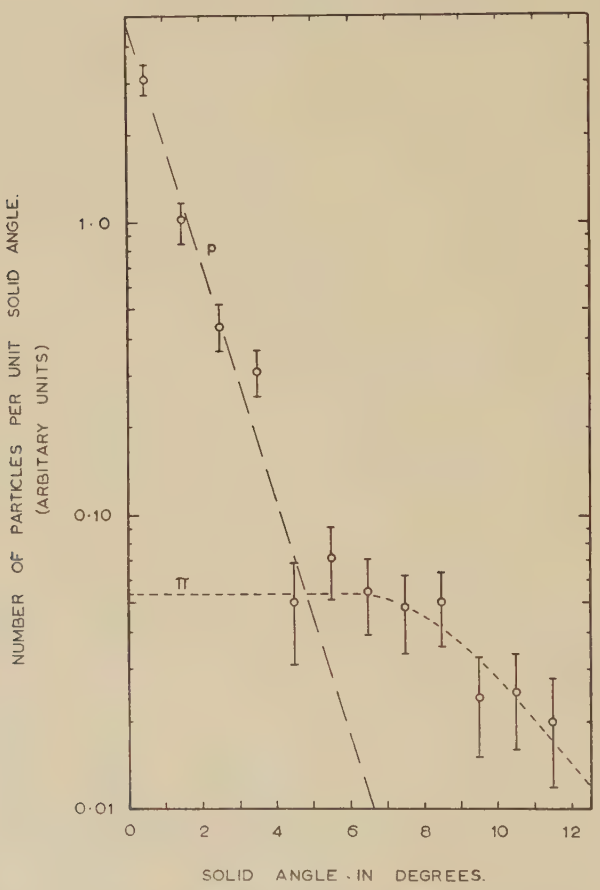

The angular distribution of singly charged particles emitted from interactions with $N_h \geqslant 1$. The suggested contributions due to protons and mesons are shown by the dashed lines marked p and π respectively.

mean momentum of the producing particles is 3150 Mev/c per nucleon, Fowler *et al.* (1957) the kinetic energy of emission of the protons in the C-system of the incident nucleus is 10 ± 1 Mev, assuming isotropy of emission in this system. This value is in good agreement with that

found by Perkins (1949) for the mean energy of emission of protons from excited nuclei.

It can be seen from fig. 9 that in a typical interaction of the type considered, 90% of the singly charged particles emitted within an angle

Table 5. The Comparison of Measured Charges with those Deduced from the Characteristics of Interactions

No.	Interaction	Deduced charge	Z_δ	Z_g	Remarks
1	1+3α+0	6	6·15	6·45	
2	4+3α+0	6	5·65	6·2	All N_h short, black
3	0+α+1	3	—	3·1	
4	0+α+1	3	—	2·9	
5	0+2α+1	5	5·3	4·7	Not hydrogen collision
6	0+2α+1	5	—	4·4	Not hydrogen collision
7	1+Li+α+1	5	—	5·3	N_h black, slow
8	1+Be+α+1	7	7·05	7·0	N_h black, slow; Z_Δ=4·4 (g)
9	1+C+α+1	8	8·35	—	N_h grey; Z_Δ=5·7 (g)
10	0+α+2	3	—	4·0	Apparent hydrogen collision
11	0+2α+2	5	5·55	7·1	Apparent hydrogen collision
12	0+2α+2	5	5·0	5·1	Apparent hydrogen collision
13	0+3α+2	7	8·15	7·1	Apparent hydrogen collision
14	1+Li+a+2	5	7·0	—	N_h light grey, mins at wide angle; possible hydrogen collision
15	0+α+3	5	6·05	4·9	Not hydrogen collision
16	0+2α+3	4	4·95	4·9	All mins at wide angle
17	1+2α+4	5	8·15	—	N_h black, slow; three mins wide angle
18	1+2α+4	8	7·65	8·7	N_h grey, probable hydrogen collision
19	0+C+4	7	6·1	6·6	Three mins wide angle Z_Δ=6·0 (g)
20	1+5	2	—	3·9	N_h black, slow; three mins wide angle
21	0+α+5	3	6·0	5·9	Four mins wide angle, possible hydrogen collision
22	0+2α+5	6	5·6	5·2	Three mins wide angle
23	0+2α+6	8	8·2	—	Two mins wide angle
24	0+Be+7	8	8·05	—	Three mins wide angle; Z_Δ=4·0 (g)
25	0+Li+8	9	7·9	8·2	Two mins wide angle
26	0+9	3	6·0	6·1	Six mins wide angle
27	0+17	12	7·1	8·0	Twelve mins within 3°
28	1+23	4	7·15	8·0	N_h black, slow; wide spray of mins

of 5° will be protons belonging to the incoming nucleus. The number of such particles, together with any fast multiply charged fragments emitted, has been taken as giving the total charge of the primary nucleus.

A lower limit to the charge is set by that carried by the multiply charged fragments, while an upper limit is set by the total visible charge. Frequently this upper limit can be reduced with fair confidence when one of the minimum tracks is at a much wider angle than any of the others, since it is then most probably the track of a recoil proton, and the interaction is one with free hydrogen. In what follows it will be arbitrarily assumed that if there is a minimum track with at least twice the angle of any of the others, and that if these others all have angles less than 5°, then the event is a hydrogen collision without meson production.

The charges of twenty-seven of the particles producing these interactions had been determined and were either those of L- or M-nuclei. The disintegrations produced by them are shown in table 5, in which the following nomenclature is adopted. Each disintegration is represented by $N_h+\Delta+\beta\alpha+n_s$; where Δ represents the type of fragment produced, β is the number of α-particles and n_s is the number of showers particles.

In this table the charge deduced from the considerations outlined above is compared with that determined from the measurements on the track of the particle. The following features can be seen :

(i) Events 1 to 4, for which the deduced charge is almost certainly correct, confirm the identification of the carbon and lithium peaks in the δ-ray and blob-gap distributions.

(ii) Although the distinction between hydrogen collisions and others is comparatively efficient for simple disintegrations, with few shower particles, events 5, 6, 10–13, it is not perfect, event 10.

(iii) The reliability of the deduced charges decreases as the number of shower particles increases.

(iv) Only in one case, event 11, does the charge as measured by one method exceed the upper limit set by the disintegration.

It would appear that the overall agreement between these deduced charges and those measured is strong confirmation of the essential correctness of the charge spectra obtained by the measurements.

Nuclear Alignment of Ytterbium 175†

By M. A. Grace, C. E. Johnson, R. G. Scurlock and R. T. Taylor
Clarendon Laboratory, Oxford

[Received June 17, 1957]

Abstract

Nuclear alignment of ^{175}Yb has been obtained by cooling a single crystal of ytterbium ethyl sulphate to about 0·014°K, and was detected by observing the anisotropic angular distributions of the two most energetic γ-rays. A relationship between the mixing ratios δ(M2/E1) for these γ-rays is obtained. γ–γ angular correlation measurements for the 282 and the 114 kev γ-rays show sensibly the same value for the correlation coefficient A_2 of $+0{\cdot}205\pm0{\cdot}015$ for solid and liquid sources containing ^{175}Yb. Using $|\delta|=0{\cdot}17\pm0{\cdot}03$ for the 282 kev γ-ray determined from the angular correlation measurements the mixing ratio for the 396 kev γ-ray is found to be $+0{\cdot}10\pm0{\cdot}03$. The nuclear moment of ^{175}Yb is $0{\cdot}15\pm0{\cdot}04$.

§ 1. Introduction

The low temperature nuclear alignment method for studying radioactive nuclei is mainly confined to elements which form paramagnetic ions. Amongst the rare earths successful experiments have been reported on isotopes of cerium and neodymium. These were incorporated into single crystals of cerium magnesium nitrate (Ambler *et al.* 1956) and of neodymium ethyl sulphate (Cacho *et al.* 1955, Bishop *et al.* 1957). When the crystals are cooled to temperatures of the order of 0·01°K, nuclear alignment arises through the anisotropy of the magnetic hfs. This paper shows that the method may be extended to ytterbium and describes some experiments on the nuclide ^{175}Yb which provide information on its decay scheme.

§ 2. Decay Scheme of ^{175}Yb

Several authors agree on the basic features of the decay scheme of ^{175}Yb which are shown in fig. 1. (See for instance Hatch *et al.* 1956.) There are only two strong γ-rays, γ_2 and γ_3, of energy greater than 150 kev and the present experiment has been confined to these. The assignment of spins to the first two excited states of ^{175}Lu was made from the results of internal conversion data and Coulomb excitation measurements and seems quite definite. The internal conversion data further shows that

† Communicated by the Authors.

γ_2 and γ_3 are mixed E1 and M2 radiations with M2/E1 mixing ratios $|\delta_2|=0{\cdot}17\pm0{\cdot}03$ and $|\delta_3|=0{\cdot}60\pm0{\cdot}20$; these are averaged values from different authors. The 396 kev state must have odd parity and from the existence of a transition γ_4 to the $11/2^+$ state its spin must be 7/2 or 9/2 ; the conversion coefficient of this γ-ray suggests that it is E1 and this would limit the spin to 9/2. Angular correlation measurements (Åkerlind *et al.* 1955) favour this assignment but are too insensitive to small values of δ_2 to enable its sign to be determined. The assignment of $7/2^+$ to the ground state of ^{175}Yb is based on the comparative half-lives of the β-transitions.

Fig. 1

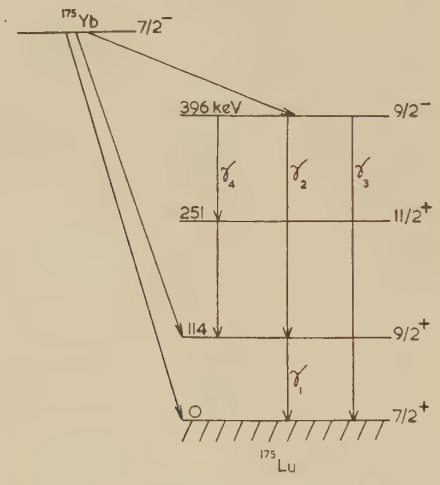

Decay scheme of ^{175}Yb.

Chase and Wilets (1956) have shown that these spin assignments and also those of other levels in ^{175}Lu known from ^{175}Hf decay can be understood in terms of the collective model and the energy levels of a single particle in a deformed potential well. Such an interpretation leads to strong inhibition of the E1 transition rate and gives rise to the observed competition between M2 and E1 radiation.

§ 3. The Crystals

The double nitrates and the ethyl sulphates are two groups of crystals containing rare earth ions, which have been shown to be magnetically anisotropic and which are therefore suitable for nuclear alignment. Since ytterbium will not crystallize easily in the double nitrate lattice it had to be grown in an ethyl sulphate crystal. Cooke and Park (1956) report that paramagnetic resonance absorption in ytterbium ethyl sulphate cannot be observed so its magnetic properties are known only from susceptibility measurements (McKim and Wolf 1955) which show

that the spectroscopic splitting factors are $g_{\parallel}=3{\cdot}4$ and $g_{\perp}=0$. The zero value for $g_{\perp}$ explains the absence of resonance and confirms that the lowest ionic state has $J_z=\pm 3/2$. Although the hfs cannot be measured directly the susceptibility measurements suggest that it must be completely anisotropic ($B=0$). The hfs coupling parameter, A, can be estimated from the results of Cooke and Park on ytterbium acetate since A/g is constant along a principal axis for any J_z level in any surroundings, provided the $J=7/2$ manifold is well separated from $J=5/2$. It is found that $A=0{\cdot}151\,\mu/I$ °K where μ and I are the nuclear moment and spin. At very low temperatures nuclear alignment, with an excess of nuclei in the $I_z=\pm I$ state, will occur. Johnson and Scurlock (1957) have shown that sufficient cooling may be obtained by adiabatic demagnetization of ytterbium ethyl sulphate at 1°K from 25 kilogauss applied along the crystal axis, when temperatures down to 0·014°K may be produced.

§ 4. Experimental

A single crystal of ytterbium ethyl sulphate was grown from a solution containing ytterbium which had been irradiated in the form of ' Specpure ' Yb_2O_3 in the Harwell pile. The active ytterbium contained both 4·2 day ^{175}Yb and 30 day ^{169}Yb so that quick crystal growing was necessary in order that the experiment could be done with a high proportion of ^{175}Yb. The initial activity of our crystal was about 20 microcuries.

The crystal was mounted in the low temperature cryostat and was cooled to various temperatures in the range 0·014°K to 1°K by demagnetizing from different fields. The angular distributions of γ_2 and γ_3 were measured with a pair of NaI (T1) scintillation counters mounted along and perpendicular to the axis of alignment (the crystal axis). The temperature T was determined from measurements of the d.c. susceptibility of the crystal and the T–T^* data of Johnson and Scurlock, and only changed by about 15% over the measuring time of six minutes. At the end of this time the crystal was warmed up to the helium bath temperature to obtain the counting rate for isotropic emission and all counting rates were normalized to this.

The pulse height distribution showed well resolved peaks at 282 and 396 kev (12% full width at half height) and the counting rate due to each of these was separately determined using two discriminators set in the trough below each peak. From these counting rates the anisotropies of the two γ-rays were evaluated as functions of temperature. It was necessary to correct the counting rate in the channel covering the 282 kev peak for two effects : (i) for pulses due to γ_3 lying within the channel ($\sim$21%) and (ii) for the 308 kev γ-radiation from the ^{169}Yb contamination (10% to 30% depending on the age of the source). Both these corrections can be made reliably and lead to an increase in the magnitude of the anisotropy of γ_2 by a factor lying between 1·3 and 2·0 depending on the amount of ^{169}Yb. These corrections do not affect γ_3.

Auxiliary experiments showed that the 308 kev radiation from ^{169}Yb is emitted isotropically ; this isotropy is to be expected since the transition is fed through a state of 0·7 microsecond half-life. No evidence for any other contamination was found.

§ 5. Results and Discussion

The dependence of the anisotropy $\epsilon=1-I(0)/I(\frac{1}{2}\pi)$ of γ_2 and γ_3 on 1/T is shown in fig. 2. It is seen that the two anisotropies are of opposite sign, the magnitude of that of γ_2 being greater than that of γ_3. Now the

Fig. 2

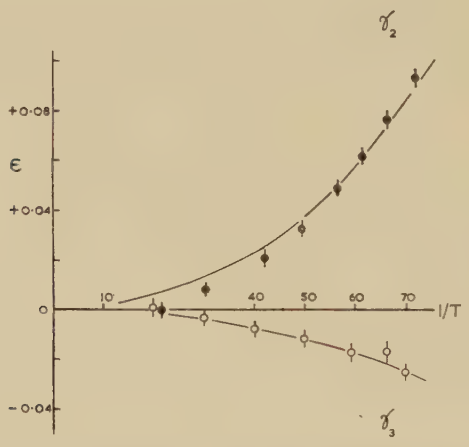

The dependence of the anisotropy on temperature for the γ-rays (γ_2, γ_3) from ^{175}Yb.

angular distribution of the γ-radiation at any temperature may be expressed as

$$I(\theta)=1+A_2P_2(\cos\theta)+A_4P_4(\cos\theta)$$

where $P_2(\cos\theta)$ and $P_4(\cos\theta)$ are Legendre polynomials and

$$A_2=B_2U_2F_2(1+3\alpha\delta-3\beta\delta^2)/(1+\delta^2).$$

B_2 is temperature dependent and describes the degree of alignment. U_2 is a function of the spins involved in the β-transition. F_2, α and β are functions of the spins and multipolarity of the γ-ray transition, and δ is the M2/E1 mixing ratio (Cacho *et al.* 1955).

From the counting rates on the two counters at the lowest temperature reached (0·014°K) the following values of A_2 and A_4 are obtained :

γ-ray energy	A_2	A_4
282 kev (γ_2)	$-0{\cdot}061\pm0{\cdot}003$	$-0{\cdot}004\pm0{\cdot}004$
396 kev (γ_3)	$+0{\cdot}017\pm0{\cdot}003$	$-0{\cdot}002\pm0{\cdot}004$

In this experiment U_2 is the same for both γ-transitions since they originate in the same level. F_2, α and β are known for γ_2 and γ_3 and hence from the values of A_2 for each γ-ray measured at the same temperature (i.e. for the same value of B_2) the following relationship between δ_2 and δ_3 is obtained :

$$\frac{0{\cdot}061}{0{\cdot}017} = \frac{(4{\cdot}4+6{\cdot}0\delta_2-2{\cdot}7\delta_2{}^2)}{(3{\cdot}0-18{\cdot}7\delta_3-0{\cdot}2\delta_3{}^2)} \cdot \frac{(1+\delta_3{}^2)}{(1+\delta_2{}^2)}.$$

The A_4 terms are too small to furnish any information about δ.

This relationship is incompatible with the values for δ_2, δ_3 derived from internal conversion data which when combined with the spin assignment of fig. 1 lead to an anisotropy for γ_3 greater in magnitude than that for γ_2. Moreover with the value of $0{\cdot}6\pm0{\cdot}2$ for δ_3 no real value for δ_2 can be obtained. The corrections applied to the anisotropy of γ_2 cannot explain this discrepancy, and one is led, therefore, to consider the possibility of attenuation of the angular correlation in the measurements of Åkerlind *et al.* through coupling between the nuclear moment and the surrounding fields. Their measurements were made in an aqueous solution of $Yb(NO_3)_3$ where attenuation effects might be expected to be smaller than in a solid source. Angular correlation measurements were made, therefore, on different solid sources of ^{175}Yb to see whether any change in the angular correlation could be observed. Since the results showed negligible contribution ($<0{\cdot}02$) due to $P_4(\cos\theta)$ terms the analysis has been made on the basis of a $P_2(\cos\theta)$ term only. This gave the following values for the angular correlation parameter A_2 :

Source	A_2
$Yb(NO_3)_3$ in water	$+0{\cdot}202\pm0{\cdot}015$
Yb_2O_3	$+0{\cdot}207\pm0{\cdot}015$
$Yb(C_2H_5SO_4)_3 \cdot 9H_2O$	$+0{\cdot}206\pm0{\cdot}021$

Corrections have been applied for the finite angles ($\pm23°$) subtended by the counters at the source. It is seen that these values agree amongst themselves and with that obtained by Åkerlind *et al.* ($+0{\cdot}202\pm0{\cdot}012$). Since no difference is found between solid and liquid sources it is believed that this value must indeed represent the full angular correlation. This conclusion has been reached independently by Wiedling (1957). The conversion coefficients for γ_1 show that δ_1 is about 0·5. Combining this with the angular correlations results shows that δ_2 must lie in the range $-0{\cdot}2$ to $+0{\cdot}2$. This is in satisfactory agreement with the internal conversion data and together with our nuclear alignment result yields

$$\delta_3 = +0{\cdot}10\pm0{\cdot}03$$

which, as already pointed out, cannot be reconciled with the value ($0{\cdot}60\pm0{\cdot}20$) deduced from internal conversion measurements. This disagreement can be removed by assuming the spin of the 396 kev state

to be $7/2^-$ but then the values of δ_2 disagree. Since all the information on this level favours 9/2 and since all the data on the γ_2–γ_1 cascade are self-consistent it seems preferable to assume that it is the interpretation of the data leading to the value of δ_3 that is in error.

For a given value of δ_2, B_2 can be deduced from A_2 at any temperature. The hfs constant A and hence the nuclear magnetic moment can be determined from a knowledge of the temperature, since B_2 is a known function of A/T and the spin I. Thus for γ_2 at 0·014°K, $A_2=-0{\cdot}061$: hence $B_2=0{\cdot}142$, $A=0{\cdot}0064$°K and the magnetic moment of ^{175}Yb is

$$\mu=0{\cdot}15\pm0{\cdot}04 \text{ nuclear moment}$$

The error arises from the uncertainty in the sign of δ_2. The theoretical dependence of ϵ on $1/T$ using this value for the moment, is shown in the solid curves and the experimental points are seen to be in close agreement.

Acknowledgments

We are indebted to Dr. N. Kurti for many stimulating discussions. We acknowledge gratefully the encouragement and interest taken in this work by the late Professor Sir Francis Simon.

References

Åkerlind, L., Hartmann, B., and Wiedling, T., 1955, *Phil. Mag.*, **46,** 448.
Ambler, E., Hudson, R. P., and Temmer, G. M., 1956, *Phys. Rev.*, **101,** 196.
Bishop, G. R., Grace, M. A., Johnson, C. E., Lemmer, H. R., and Perez, J., 1957, *Phil. Mag.*, **2,** 534.
Cacho, C. F. M., Grace, M. A., Johnson, C. E., Knipper, A. C., Scurlock, R. G., and Taylor, R. T., 1955, *Phil. Mag.*, **46,** 1287.
Chase, D. M., and Wilets, L., 1956, *Phys. Rev.*, **101,** 1038.
Cooke, A. H., and Park, J. G., 1956, *Proc. phys. Soc. Lond.* A, **69,** 282.
Elliott, R. J., and Stevens, K. W. M., 1957, *Proc. phys. Soc. Lond.*, A, **64,** 205.
Hatch, E. N., Boehm, F., Marmier, P., and Du Mond, J. W. M., 1956, *Phys. Rev.*, **104,** 745.
Johnson, C. E., and Scurlock, R. G., 1957 (to be published).
McKim, F. R., and Wolf, W. P., 1955, reported by A. H. Cooke at the Conference of Low Temperature Physics, Paris.
Wiedling, T., 1957, *Thesis*, University of Stockholm.

The 4·77 MeV Level in Boron 10†

By H. Warhanek
Cavendish Laboratory, Cambridge, England‡

[Received June 6, 1957]

Abstract

The angular distribution of the γ-rays in $^{6}Li(\alpha\gamma)^{10}B$ has been measured for the 500 kev resonance. Spin and parity of the 4·77 Mev level in ^{10}B are 2+ or 3+. The intensity of the direct transition to the ground state is less than 3% of the intensity of the 4·05 Mev γ transition. The width of the level $\omega\Gamma_\alpha\Gamma_\gamma/\Gamma_\alpha+\Gamma_\gamma$ is about 5×10^{-2} ev. The 4·05 Mev E2 transition is at least twice as strong as one would expect from the Weisskopf formula.

§ 1. Introduction

The low-lying levels of ^{10}B are shown in fig. 1 (Ajzenberg and Lauritsen 1955). From decay scheme and isotopic spin considerations one would expect the 4·77 Mev level to be 1+ (Wilkinson and Jones 1953). But this assignment does not fit into the level scheme calculated by Kurath on the basis of the shell model in intermediate coupling (Kurath 1956). This theoretical level scheme is in good agreement with experiment for the first five levels of ^{10}B, but in the region of the 4·77 Mev level it contains no 1+ state.

Fig. 1

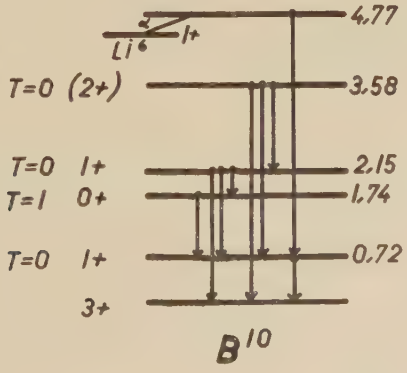

† Communicated by D. H. Wilkinson, F.R.S.
‡ Permanent address: Institut für Radiumforschung und Kernphysik, Vienna 9, Austria.

§ 2. Angular Distribution

In order to determine the spin and parity of this level in a more direct way the angular distribution of the γ-rays from it has been measured following its formation in the reaction $^{6}\mathrm{Li}(\alpha\gamma)^{10}\mathrm{B}$ at an α-particle energy of 500 kev.

The possible assignments for this level are: $0-$, $1\pm$, $2\pm$, $3+$. $0+$ cannot be formed by an α transition from a $1+$ state, and $3-$ can be excluded because of the absence of the cross over which would be E1 while the observed 4·05 Mev γ-ray would be M2. The inhibition of the isotopic spin selection rule would not be adequate. Also the observed radiative width excludes an M2 transition completely.

In the theoretical distribution of the 4·05 Mev γ-ray

$$W(\theta)=1+\sum_{k=1}^{n} a_{2k}P_{2k}(\cos\theta)$$

$n\leqslant 2$ for all cases except for $3+$ where $n=3$. But as we shall see later, a_6 would be quite small in this case†. One can therefore assume, that the distribution contains only terms with $k\leqslant 2$.

2.1. *Experimental Method*

^{6}Li targets were bombarded in a Cockcroft–Walton generator. The cross section of the beam was defined by a slit 15 mm long and 2·3 mm wide normal to the plane of the movable detector. The target was mounted at 45° to the α-particle beam. The γ-rays were detected by a NaI(Tl) crystal (2·5 × 1·75 in.). The distance of the near end of the crystal from the target was about 4 cm. Another crystal was used for monitoring. Measurements were made at 0°, 45° and 90° to the α-particle beam.

2.2. *Corrections*

A correction for the finite solid angle of the γ detector was evaluated from Rose's formulae (Rose 1953). The formula for full absorption was used taking as the solid angle a mean value between the solid angle subtended by the near end of the crystal and the one subtended by the far end.

A small correction for the different absorption in the target in the 0° and 90° and in the 45° detector position was applied in the case of the 4·05 Mev γ-ray. The 720 kev γ-ray was measured only at 0° and 90°.

No correction was applied for the finite size of the target.

2.3. *Result*

2.3.1. 4·05 Mev *γ-ray*

The experimental distribution is

$$W(\theta)=1+(0{\cdot}46\pm 0{\cdot}035)P_2(\cos\theta)-(0{\cdot}28\pm 0{\cdot}06)P_4(\cos\theta).$$

† Mixtures with the next higher possible angular momentum transition are taken into account in both, the α and the γ transition.

This excludes certainly 0−, 1+, and 1−. 0− would have an isotropic distribution and for spin 1 no fourth-order term would appear. Also it is impossible to get this distribution with the assignment 2− whatever reasonable mixing ratio in the α and in the γ transition one may assume.

For 2+ with an E2 to M1 intensity ratio of 0·64 the theoretical coefficients are (no α-mixing occurs)

$$a_2=0{\cdot}46, \qquad a_4=-0{\cdot}30$$

in agreement with the experimental finding.

For 3+ one obtains theoretically with no mixing in either transition :

$$a_2=0{\cdot}50, \qquad a_4=-0{\cdot}30, \qquad a_6=0$$

again in agreement with experiment†.

One has therefore 2+ and 3+ as possible assignments.

2.3.2. 720 kev *γ-ray*

The theoretical distributions are almost isotropic for all the possibilities mentioned. Experimentally the ratio of the counting rates at 0° and 90° was found to be $1\pm0{\cdot}1$.

§ 3. Search for the Direct Transition to the Ground State

For both the possible assignments 2+ and especially for 3+ the absence of the direct transition to the ground state is surprising. A search for this cross over was made measuring the γ spectrum with the $2{\cdot}5\times1{\cdot}75$ in. crystal in bad geometry at 45° to the α particle beam. The intensity of the cross over appeared to be less than 3% of the intensity of the 4·05 Mev γ-ray.

§ 4. Level Width

The cross section of the 500 kev resonance in $^6\mathrm{Li}(\alpha\gamma)^{10}\mathrm{B}$ was roughly measured. A thick target of pure natural lithium was bombarded ; the secondary electrons were captured in a Faraday cage. The γ-spectrum was measured at 45° to the α-particle beam‡. The result was

$$\omega\Gamma=5\times10^{-2}\ \text{ev}, \qquad \Gamma=\frac{\Gamma_\alpha\Gamma_\gamma}{\Gamma_\alpha+\Gamma_\gamma}$$

(corrected for angular distribution) which should be accurate within 50%. This is somewhat smaller than the value estimated in Jones and Wilkinson (1954). But the difference can—at least partially—be explained by the highly anisotropic angular distribution.

---

† It is very reasonable to assume both mixing ratios to be very small. The ratio of the α-particle penetrations would be $\sim10^{-3}$ and the γ transition would be a mixture of E2 and M3.

‡ The spectrum of the 8·9 Mev γ-ray coming from the 400 kev resonance in ^{7}Li has to be subtracted. The width of the 8·9 Mev level in ^{11}B determined in this reaction is $\omega\Gamma=9\times10^{-3}$ ev. (No correction for angular distribution was considered.)

With this value and with the assumption $\Gamma_\gamma \ll \Gamma_\alpha$ one obtains for the γ width of the 4·05 MEV transitions.

For 2+ :

$$\Gamma_\gamma(\mathrm{M1}) = 1{\cdot}8 \times 10^{-2}\ \mathrm{ev} = 1{\cdot}3 \times 10^{-2}\ \Gamma_{\gamma W},$$

$$\Gamma_\gamma(\mathrm{E2}) = 1{\cdot}1 \times 10^{-2}\ \mathrm{ev} = 4\Gamma_{\gamma W},\dagger$$

$\Gamma_{\gamma W}$ = width obtained from the Weisskopf formula.

For 3+ :

$$\Gamma_\gamma(\mathrm{E2}) = 2{\cdot}1 \times 10^{-2}\ \mathrm{ev} = 7{\cdot}5\Gamma_{\gamma W}.$$

Since successful competing of α-decay with γ-decay occurs in the region around 7 MEV excitation, the assumption $\Gamma_\gamma \ll \Gamma_\alpha$ is probably not fulfilled and Γ_γ is probably even larger.

These very strong E2 transitions seem to be another indication for collective motion in ^{10}B (Bloom *et al.* 1957). Since in ^{10}B neutrons and protons are just filling half a shell it may be reasonable to believe in collective motion even in such a light nucleus.

For the cross over one obtains (neglecting a possible E2 contribution) the very small values

$$\Gamma_\gamma(\mathrm{M1}) < 8{\cdot}8 \times 10^{-4}\ \mathrm{ev} \doteq 3{\cdot}8 \times 10^{-4}\Gamma_{\gamma W} \quad \text{for} \quad 2+,\ddagger$$

and

$$\Gamma_\gamma(\mathrm{M1}) < 6{\cdot}3 \times 10^{-4}\ \mathrm{ev} = 1{\cdot}7 \times 10^{-4}\Gamma_{\gamma W} \quad \text{for} \quad 3+.\ddagger$$

With the assumption $\Gamma_\alpha \ll \Gamma_\gamma$ one obtains for the reduced α-width

$$\omega\gamma^2 = 1{\cdot}2 \times 10^{-3}(\hbar^2/MR)$$

as a lower limit for both assignments.

Although the assignment 2+ is favoured in view of the lack of the cross over and in view of the E2 width as compared with the Weisskopf formula, the assignment 3+ cannot be excluded.

Acknowledgments

The author wishes to thank Dr. D. H. Wilkinson for suggesting the problem and for very stimulating and helpful discussions. He is grateful to the British Council for a scholarship.

References

Ajzenberg, F., and Lauritsen, T., 1955, *Rev. mod. Phys.*, **27**, 77.
Bloom, S. D., Turner, C. M., and Wilkinson, D. H., 1957, *Phys. Rev.*, **105**, 232.
Jones, G. A., and Wilkinson, D. H., 1954, *Phil. Mag.*, **45**, 703.
Kurath, D., 1956, *Phys. Rev.*, **101**, 216.
Rose, M. E., 1953, *Phys. Rev.*, **91**, 610.
Wilkinson, D. H., and Jones, G. A., 1953, *Phys. Rev.*, **91**, 1575.

† If one takes all experimental values just on the limit of their experimental error, one still obtains Γ_γ (E2) $= 2\ \Gamma_{\gamma W}$.

‡ These values may be too small again because of the assumption $\Gamma_\gamma \ll \Gamma_\alpha$.

K-Capture in Carbon 11

By J. Scobie and G. M. Lewis
Department of Natural Philosophy, University of Glasgow

[Received June 17, 1957]

Abstract

K-capture in ^{11}C has been observed and the K/β^+ ratio found. Comparison with theory leads to a value for the ratio of the Fermi coupling constants. Proportional counters were employed with a gaseous source, and two anti-coincidence systems were used, in turn, to reduce wall effects. One made use of a multi-wire ring type counter and the other utilized an envelope of scintillating material coupled to a photomultiplier. The K β^+ ratio has been determined at $(1{\cdot}9\pm0{\cdot}3)\times10^{-3}$, and accords closely with the theoretical value based on the vanishing of interference terms. A comparison shows that the factor b in beta-decay theory, which determines the ratios of decay coupling constants, is $(-0{\cdot}03\pm0{\cdot}10)$. In this decay between mirror nuclei the Fermi matrix element predominates, and the ratio of the two Fermi coupling constants C_v/C_s has been deduced at $(-0{\cdot}02\pm0{\cdot}09)$, from data on the better known Gamow–Teller constants. The pulse height distribution obtained in these experiments showed that little ionization was produced by the nuclear recoil following neutrino emission, though the recoil energy could be comparable with the 180 ev capture x-ray energy.

§ 1. Introduction

A search for K-capture and a direct measurement of the K/β^+ ratio in ^{11}C was of interest for several reasons. In the first instance, the transition ^{11}C–^{11}B occurs between mirror nuclei with zero spin change. Both Fermi and Gamow–Teller terms can be expected, but the Fermi matrix element predominates (cf. below). A comparison of the experimental value of the K/β^+ ratio with the theoretical one is therefore important in beta-decay theory, as it allows an assessment of the Fierz interference term for the Fermi interaction.

The decay of ^{11}C is a simple one with a linear Fermi plot (Wong 1954), and it is superallowed since the half-life value of 20·7 min (Kundu *et al.* 1953) is associated with a log ft value of 3·6. Whilst results are available on the K/β^+ ratio for several nuclei (cf. the review by Radvanyi 1955), direct investigations and measurements on simple allowed transitions have been rare. More recently work of this type has been carried out on ^{18}F (Drever, Moljk and Scobie 1956), which has a Gamow–Teller decay.

† Communicated by Professor P. I. Dee, F.R.S.

One of the primary objectives in beta-decay and K-capture investigations is an assessment of the coefficients of the decay interaction

$$H=\sum_{n=1}^{5}(C_nH_n+C_n'H_n')$$

where the suffices refer to the S, V, A, T, P forms, and the accented terms are the additional parity-non-conserving terms introduced by Lee and Yang (1956). Following De Groot and Tolhoek (1950), and Lee and Yang (1956), the allowed β^+ spectrum emitted by a nucleus of low atomic number is given by

$$N(W)\,dW=\alpha F(Z,W)pW(W_0-W)^2\,dW[1-(b/W)] \quad . \quad . \quad (1)$$

where α and b are functions of the C_n, C_n' and the matrix elements (cf. eqn. (4) below). If for instance C_V, C_V' and C_A, C_A' vanish, b is zero. The probability of K-capture is

$$P_K=\tfrac{1}{2}\pi\alpha(\text{available energy})^2f_K^2(1+b) \quad . \quad . \quad . \quad . \quad (2)$$

where f_K is the value of the bound electron wave function at the nucleus.

Limits on b have been set from considerations of the beta-spectrum shape, but criticisms of the accuracy of this method exist (cf. Winther and Kofoed-Hansen 1953). Davidson and Peaslee (1953) assessed $|C_A/C_T|<4\%$; and found $|b|<20\%$ for the case of ^{13}N, which also has a Fermi interaction.

The K/β^+ ratio can yield fresh evidence of the validity of the theory, and provides a method of determining mixing ratios, since

$$\frac{P_K}{P_{\beta^+}}=\frac{1+b}{1-b(1/W)_{av.}}\left(\frac{P_K}{P_{\beta^+}}\right)_{b=0} \quad . \quad . \quad . \quad . \quad . \quad (3)$$

Deductions concerning the Gamow–Teller coefficients have already been reported in this connection. Sherr and Miller (1954) deduced a value for the Gamow–Teller coefficients, C_A/C_T of $(-1\pm2)\%$ for ^{22}Na by a subtraction method, assuming the transition to be an allowed one. Observations on ^{18}F by Drever, Moljk and Scobie (1956) led to a value C_A/C_T of $(0{\cdot}4\pm2)\%$. (These values do not take into consideration the parity-non-conserving terms.)

Accord between the experimental K/β^+ value for ^{11}C and that given by eqn. (3), where b is small, would be of interest. The predicted K/β^+ value is $2{\cdot}0\times10^{-3}$ for b zero (cf. below). From this a limit can be specified on the ratio of the two Fermi coupling constants C_V/C_S. For this it is necessary to know the relative contributions of the Fermi and Gamow–Teller interactions. Information on this latter subject can be obtained from studies of decay times of mirror nuclei with one free nucleon (Winther and Kofoed-Hansen 1953).

In the decay of ^{11}C by K-capture there is another matter of interest. The K x-ray energy of ^{11}B is 180 ev (cf. Compton and Allison 1935), and this is released mainly as an Auger effect (cf. Burhop 1952). As the disintegration energy is near 2 MeV the neutrino is capable of imparting

appreciable recoil energy. For a free radioactive atom this recoil energy is 190 ev. It seemed of interest to determine whether any detectable ionization effects would be produced by ^{11}B ions formed from free ^{11}C atoms, or whether the motion of the ions would be too slow for these to appear.

Previous to the present work the lowest energy electron capture radiation reported was the L-capture radiation of ^{37}A with an energy of 240 ev, first observed by Pontecorvo *et al.* (1949). Since there is no positron emission accompanying this decay, the electron capture peak can be readily observed in a conventional proportional counter. However, where the ratio of electron capture to positron emission is small, the capture peak is superimposed on a substantial continuous background due to the positrons. Due to limitations on the size of the counter and the gas pressure the majority of the positrons have path lengths large compared with the counter dimensions, and therefore lose only a fraction of their energy in the counter. This wall effect gives rise to a continuous pulse spectrum which rises steeply at low energies. Previous work on electron capture in ^{18}F showed that this rising background would obscure any low energy electron capture peak with an intensity less than about 1%. Large reductions in wall effect can be effected by the use of a multi-wire ring type counter (cf. Drever, Moljk and Curran 1957), and measurements with a counter of this type are referred to below.

Another type of counter has also been constructed here, which employs scintillation techniques to reduce wall effects. In this counter the gas envelope consists of scintillating material coupled to a photomultiplier. Proportional counter pulses from beta-particles which leave the gas can be eliminated by a gate, operated by the photomultiplier pulses. The particular counter used was a small prototype model, but the case of ^{11}C seemed a good one to test its potentialities. A plastic walled counter should have an advantage over a ring type counter in that the β^+ count, which appears in the K/β^+ ratio, can be found directly by using the inner counter only.

§ 2. Apparatus

2.1. *Multi-wire Counter*

Recently, Drever, Moljk and Curran (1957) have constructed counters in which the above-mentioned wall effects are almost completely eliminated. The main counter is surrounded by a second proportional counter system in anti-coincidence ; all the counters being enclosed in one metal case. The counting volume of the main counter is defined by a ring of wires joined to the case, and further wires divide the layer of gas surrounding the central counter into separate proportional counters of approximately square cross section. Beta-particles escaping from the central counter are detected in the anti-coincidence ring counters, the pulses from which are used to gate the pulses from the central counter. The counter used in the present work was similar to those described in Drever, Moljk and

Curran, but was smaller and simpler, the total diameter being 7·5 cm and the sensitive length 50 cm.

Due to the presence of the gaseous source in the anti-coincidence ring, some of the pulses from the central counter are due to particles which originate in the ring counter. The volume of the central counter is approximately one-third of the total counter volume, and it has been verified, in a separate experiment with a ^{37}A source, that the sensitive volumes of the central and ring counters are in the ratio one to two. Since the electron capture radiations from ^{37}A have ranges very small compared with the counter dimensions the counting rates from the two counter systems are in the ratio of the sensitive volumes.

By adding electrically the pulses from the central and ring counters the total number of disintegrations in the counter is obtained, irrespective of the range of the particles. The number of disintegrations in the central counter is then obtained by multiplying the total number by the ratio of the volume of the central counter to the total volume.

2.2. *Plastic Counter*

The walls and ends of this counter consisted of $\frac{1}{2}$ in. thick plastic scintillator (cf. fig. 1). It was 6 in. long and 1 in. diameter inside, and

Fig. 1

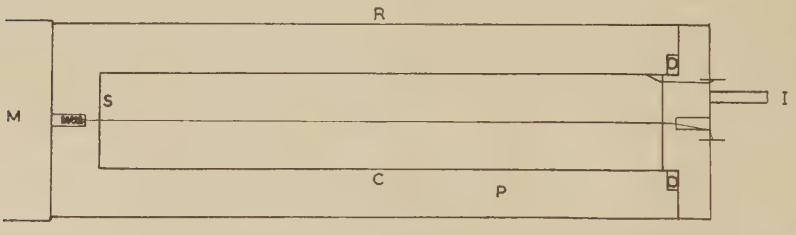

Construction of plastic counter. C, cathode of aluminium foil; P, plastic scintillator; M, photomultiplier; S, thin black polythene screen; R, reflector; I, gas input.

the aluminium cathode was 0·0002 in. thick. Because of the small size of this prototype counter, no guard rings were provided. The counter was sealed at one end and at the other was mounted in optical contact with a Dumont photomultiplier type 6292. An aluminium reflector was used at the sides, and a diffuse insulating reflector at the distant end; black polythene and wrappings of Lassovic tape elsewhere made the whole light tight. A thin window had to be provided in the fabric to permit the entry of ^{71}Ge x-ray calibrating radiation. Preliminary work showed that electrons of energy greater than 25 kev in the plastic would operate the anti-coincidence unit satisfactorily.

Like the ring-type counter this plastic type of counter has considerable promise in low background applications. For such work it is necessary to insert thin sheets of black polythene at the inside end surfaces to

prevent the small light pulses generated in the proportional tube discharge from reaching the photomultiplier. The effectiveness of the system was first judged by surrounding the counter by about 3 in. of lead. With an argon–methane mixture at one atmosphere the counting rate fell from 30 counts per minute to one count per minute when the anti-coincidence system was switched in. In the present K/β^+ application it was advantageous to omit the black polythene sheets, in order to reduce end effects. The proportional counter pulses from which light could be picked up were considerably larger than the pulses which concern us here.

2.3. *Electronics*

The pulses from the central counter were fed, through amplifiers and a delay of 20 μsec, to a linear anti-coincidence gate. Pulses from the outer counter were similarly amplified and fed to an amplitude discriminator. The output was amplified to 80 v and lengthened to 200 μsec by a double Schmitt circuit, and was fed to the gate valve, thus removing those pulses from the central counter in coincidence with pulses from the outer counter. The circuit was so arranged that pulses from the central counter with amplitudes greater than 50 v were fed through to the anti-coincidence side of the circuit and were eliminated. This had the effect of considerably reducing the number of pulses with which the analysing system had to deal, and also avoided the presence, in the later stages of the electronics, of very large pulses. The overshoots of the baseline which follow such large pulses are of considerably greater duration than the pulses themselves, and a smaller pulse following closely behind such a pulse is liable to be considerably distorted. Due to the cut-off at 50 v, however, such an event is not transmitted to the analysing system.

The spectrum of pulses which passed through the gate was analysed in two completely separate ways ; by a Hutchinson–Scarrott 100 channel kick-sorter, and by photography. The pulses were photographed on a commercial oscilloscope whose timebase was triggered by the pulses themselves. To enable the front edge of each pulse to be clearly seen the input pulses to the oscilloscope were delayed by 10 μsec relative to the trigger pulses. In view of the doubtful stability of the triggering level in the commercial oscilloscope the trigger pulses were obtained from an external discriminator whose bias was stable and accurately known. With this method the whole of each pulse is seen on a separate sweep, and, since the proportional counter pulse is of a well-defined shape and length, any extraneous pulses due to pick-up may be rejected. Where a gating system is in operation this method has also the advantage of eliminating those pulses which have arrived in coincidence with the edges of the gate pulse and which have in consequence been distorted. Such spurious pulses were small in number.

The pulse-heights were measured in a micro-film reader and sorted into thirty energy channels. The discriminator providing the trigger pulse

to the oscilloscope was set at the same triggering level as the lower level of the kick-sorter in order that the two pulse-height spectra obtained would be readily comparable. A block diagram of the electronic system is shown in fig. 2.

Fig. 2

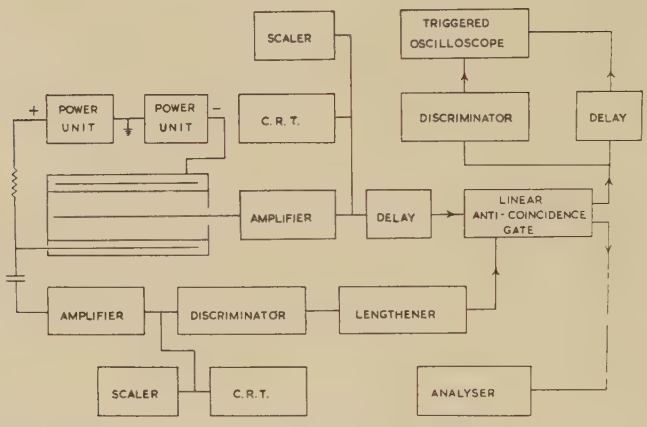

Block diagram of the electronic equipment.

Throughout the experiments the proportional counters were calibrated using the 9·2 kev x-rays emitted in the electron capture decay of ^{71}Ge. In order to calibrate the filmed spectrum pulses from a pulse generator were fed simultaneously to the triggered oscilloscope and to the kick-sorter and adjusted so that they fell in the same kick-sorter energy channel as the 9·2 kev peak. The pulses on the oscilloscope were then filmed, giving an accurate energy calibration.

§ 3. Experimental Procedure

The ^{11}C was made by (γ, n) reaction on carbon using the gamma beam from the Glasgow 350 Mev electron synchrotron. A glass bottle, filled to various pressures of propane, was irradiated for periods of about half an hour. The flux available was sufficient to give initial counting rates as high as 30 000 counts/min in the proportional counter with a partial propane pressure of about 10 cm. The propane was admitted to the counter and the pressure increased to one atmosphere by adding argon. Propane was employed because of its fairly high carbon content and density, and because the main impurities are similar hydrocarbons.

The gain of the counter was adjusted, using the 9·2 kev x-rays from ^{71}Ge for energy calibration, and the low energy end of the pulse spectrum examined by increasing the gain of the amplifier by a factor of twenty. At the very high counter gain used in the experiments it was found that the energy resolution, as defined by the width of the 9·2 kev peak, was rapidly deteriorating with increase of gain, showing the effect of local variations of gain due to space-charge. This effect set an upper limit to

the gain of the whole system, since an increase of amplifier gain would have meant an approach to amplifier noise level.

In the case of the plastic counter it had been shown that, for the multiplier gain and proportional counter voltage employed, the light pulses from the discharge produced by particle energies above a few kev were occasionally large enough to operate the anti-coincidence gate. It was desirable in carrying out the energy calibration with the 9·2 kev x-rays to disconnect the anti-coincidence system. It was ascertained that no pulses were lost due to this effect in the energy region being studied.

During the first experiments a total gas pressure of about two atmospheres was used in the proportional counter with the object of reducing the effects of particles escaping from the end of the counter. However the reduction of pressure to one atmosphere has the advantage that the average pulse size is halved, and the fluctuations in the level of the amplifier baseline due to very large pulses is reduced. Also, any distortion of the pulses due to space charge effects is reduced due to the decreased ionization density along the particle tracks.

During the experiments the counting rate in the central counter was about 3000 counts/min and of these about 15 counts/min were allowed through the gate to the analysing system. The total counting rate and the peak area were observed for several half-lives and found to decay with a half-life of 20 min. No appreciable radioactive impurity was present. The pulse spectrum due to natural background was examined after the source had decayed and was found to be very small in magnitude and flat over the energy region under study.

Since it could not be assumed that the propane–argon mixture used obeyed a linear relationship of pulse height to energy over the wide range of energy covered in the experiment, separate calibrations were made using a ^{37}A electron capture source. A trace of ^{37}A was admitted to the counters which were then filled with the same argon–propane mixture as used during the experiments. For each counter the gain was adjusted until the peak due to the 9·2 kev x-rays from ^{71}Ge was in the same kick-sorter channel as was used during the experiments, and the position of the peak due to the 2·8 kev K radiations of Cl was noted. The amplifier gain was increased by a factor of twenty and the position of the peak due to the 240 ev L radiations of Cl was noted. The position of this latter peak relative to the 9·2 kev peak provided a very convenient and accurate calibration in the search for the 180 ev peak.

Since it is essential for the measurement of low energy Auger electrons that the source be in gaseous form, a separate experiment was performed to check this point. The usual propane source was introduced, the counter was filled to the usual pressure, and the counting rate noted. The counter was then pumped out, filled as before, and the counting rate again noted. No significant increase over the background counting rate was observed, indicating that none of the source had been adsorbed on the counter wall.

In another experiment it was verified, by irradiating the empty glass bottle, that none of the source activity was due to dust or adsorbed gases coming off the walls of the glass bottle.

§ 4. Results

The low energy end of the pulse spectrum obtained with the multi-wire counter was analysed as described above and a broad peak was observed at about 180 ev which was attributed to the K x-radiations of boron emitted in the electron capture decay of ^{11}C. That part of the spectrum in the energy region between 40 ev and 600 ev is shown in fig. 3, which is the result of three successive runs.

Fig. 3

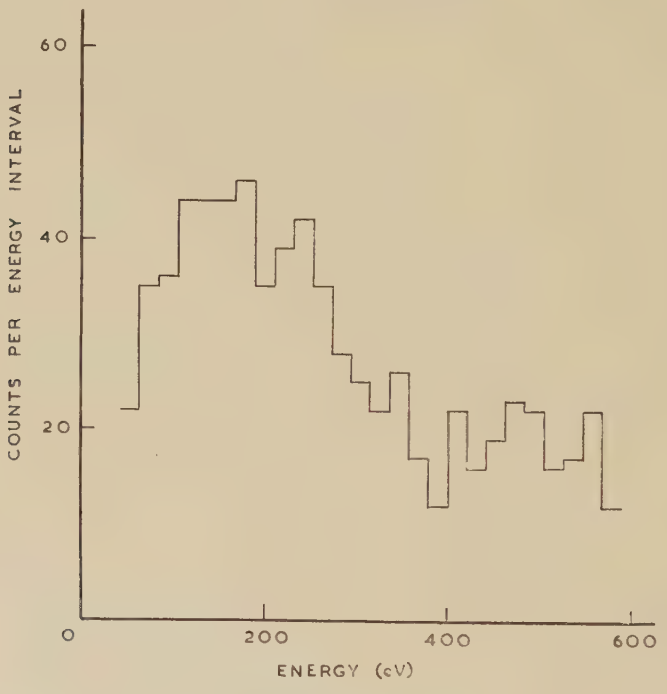

^{11}C K-peak obtained with the multi-wire counter.

The intensity of K-capture was obtained from the number of counts in the peak and the number of positrons (177 000) was obtained as described in § 2., after correcting for background. The observed ratio of K-capture to positron emission is $0{\cdot}0019 \pm 0{\cdot}0003$. Errors in the measurement are almost entirely due to the uncertainty in estimating the area of the peak. The natural background spectrum is flat at low energies and accounts for about three counts per energy interval in fig. 3. The remainder of the spectrum under the peak is largely due to those positrons which escape from the ends of the counter. Small corrections have been included for the time the gating unit was shut, and for those positrons

which enter the sensitive volume from the insensitive regions at the ends of the counter. These amounted to about 2% each.

No contribution to the energy of the peak was observed due to the nuclear recoil, indicating that little or no ionization was produced by the ions.

The pulse height distribution from the plastic counter showed a small peak near 180 ev consistent with the presence of K-capture in the above intensity. Again no shift in energy was observed.

§ 5. Discussion and Conclusions

The experiments described above reveal K-electron capture in ^{11}C. The experimental value for K β^+ ratio of $(1{\cdot}9\pm0{\cdot}3)\times10^{-3}$ agrees closely with the theoretical value of $2{\cdot}0\times10^{-3}$, when cross terms are absent. The theoretical value is based on a beta end point energy of 970 kev (cf. Wong 1954; cf. also Townsend 1940, Siegbahn and Bohr 1944, Richards *et al.* 1950), and a correction for electron screening has been applied by writing the effective Z value for the 1s electron of ^{11}C as 5·69 (cf. Duncanson and Coulson 1944, Torrance 1934, Tubis 1956). A comparison between the experimental and theoretical values for the K β^+ ratio indicates that b of eqn. (3) is $(-0{\cdot}03\pm0{\cdot}10)$. Possible slight error in the theoretical value due to variation in the β^+ end point determination has been allowed for. Whilst the results obtained by the various authors for the screening correction agree, some error might arise from the choice of method of approximation. No allowance has been made for this.

b can be written

$$b=2\frac{(C_S C_V+C_S'C_V')|M_F|^2+(C_T C_A+C_T'C_A')|M_{G-T}|^2}{(C_S^2+C_V^2+C_S'^2+C_V'^2)|M_F|^2+(C_T^2+C_A^2+C_T'^2+C_A'^2)|M_{G-T}|^2} \quad . \quad . \quad . \quad . \quad (4)$$

in the notation of Lee and Yang (1956), where C_n, C_n' are taken to be real, corresponding to the preservation of time reversal invariance. Previous to the parity-non-conservation work, the small value of b implied a small or zero value of two coefficients, usually taken to be C_V and C_A. This does not necessarily follow from eqn. (4). If, however, one includes additionally the results of recoil experiments on ^{6}He (Rustad and Ruby 1953) a small value for b implies that C_A and C_A' are small. Recent parity measurements (Wu *et al.* 1957) show that C_T and C_T' are of opposite sign and the results could be consistent with $C_T=-C_T'$. At the present time one cannot be appreciably more specific. The customary expression, used before the work on parity, is obtained by supposing equally simple conditions to hold between the other coefficients. This would follow if the two-component neutrino theory is valid (cf. Lee and Yang 1957). The expression for b can then be tentatively written, as in the past

$$b=2\frac{C_S C_V|M_F|^2+C_T C_A|M_{G-T}|^2}{C_S^2|M_F|^2+C_T^2|M_{G-T}|^2} \quad . \quad . \quad . \quad . \quad . \quad (4')$$

where small quantities are neglected, and C_S and C_T are taken as the large components. The results of other investigators can then be incorporated.

The *ft* value of a transition can be expressed in the form

$$ft\{(1-x)|M_F|^2+x|M_{G-T}|^2\}=B$$

where x is $C_T^2/(C_S^2+C_T^2)$, and B will not vary appreciably from nucleus to nucleus if b is small. Winther and Kofoed-Hansen (1953) plotted B against x for those mirror nuclei with one free nucleon, from a knowledge of the experimental *ft* value and from a mathematical evaluation of the matrix elements. They found that B was 2650 ± 85, and x was $0{\cdot}50\pm0{\cdot}05$. The treatment below is based on these results. Since $|M_F|^2=1$ for the mirror nucleus ^{11}C, one can assess $|M_{G-T}|^2$ empirically for this nucleus from the *ft* value. In this way one obtains $|M_{GT}|^2/|M_F|^2<0{\cdot}47$. (Theoretical computations of $|M_{GT}|^2$ exist, based on various models, cf. Winther and Kofoed-Hansen 1953, Trigg 1952 ; but because of the theoretical difficulties involved in considering a complex mirror nucleus like ^{11}C, reliance is placed here on the empirical method.)

By inserting this result in eqn. (4) and by utilizing the known data on C_A/C_T from the Introduction, e.g. the value found by Drever, Moljk and Scobie (1956) of $(0{\cdot}4\pm2)\%$, one can specify C_V/C_S. This procedure leads to a value for C_V/C_S of $(-0{\cdot}02\pm0{\cdot}09)$.

The peak in the pulse height distribution is seen to be centred near the K x–ray energy of 180 ev. The calibration and statistical accuracies are too low to specify the energy liberated with precision. The pulse height distribution shows no ionization effects from the recoil of the ion. The radioactive ^{11}C atoms formed in the initial photodisintegration process may well have become attached to gas molecules. Alternatively it seems likely that ionization caused by ^{11}B ions would be small because their low speeds would produce an adiabatic change only in the collision process (cf. Massey and Burhop 1952), and the energy is more rapidly expended in mechanical collisions. Direct ionization experiments which have been reported in the literature with various ions and gases, which are difficult to perform at low energies, seem to support this view (cf. the review by Massey and Burhop 1952).

Lastly, from a technical aspect, the plastic counter showed adequate promise in both the low background and electron capture fields of study and a larger model is now under construction.

Acknowledgments

We would like to thank Professors P. I. Dee and J. C. Gunn for their interest, also Dr. W. McFarlane and the Synchrotron crew for carrying out the irradiations. We are also grateful to Mr. R. W. P. Drever for suggestions and helpful discussions, and to Dr. A. Moljk for useful discussions at an early stage of the work. One of us (J. S.) in indebted to the University of Glasgow for a scholarship.

References

Burhop, E. H. S., 1952, *The Auger Effect* (Cambridge : University Press), pp. 48–51.

Compton, A. H., and Allison, S. K., 1935, *X-rays in Theory and Experiment* (New York : Van Nostrand), pp. 784, 792.

Davidson, J. P., and Peaslee, D. C., 1953, *Phys. Rev.*, **91,** 1232.

De Groot, S. R., and Tolhoek, H. A., 1950, *Physica*, **16,** 456.

Drever, R. W. P., Moljk, A., and Curran, S. C., 1957, *Nucl. Inst.*, **1,** 41.

Drever, R. W. P., Moljk, A., and Scobie, J., 1956, *Phil. Mag.*, **1,** 942.

Duncanson, W. E., and Coulson, C. A., 1944, *Proc. roy. Soc. Edin.*, **62,** 37.

Kundu, D. N., Donaven, T. W., Pool, M. L., and Long, T. K., 1953, *Phys. Rev.*, **89,** 1200.

Lee, T. D., and Yang, C. N., 1956, *Phys. Rev.*, **104,** 254 ; 1957, *Ibid.*, **105,** 1671.

Massey, H. W. S., and Burhop, E. H. S., 1952, *Electronic and Ionic Impact Phenomena* (Oxford : Clarendon Press), pp. 521–533.

Pontecorvo, B., Kirkwood, D. H. W., and Hanna, G. C., 1949, *Phys. Rev.*, **75,** 982.

Radvanyi, P., 1955, *Ann. Phys.*, **10,** 584.

Richards, H. T., Smith, R. V., and Browne, C. P., 1950, *Phys. Rev.*, **80,** 524.

Rustad, B. M., and Ruby, S. L., 1953, *Phys. Rev.*, **89,** 880.

Sherr, R., and Miller, R. H., 1954, *Phys. Rev.*, **93,** 1076.

Siegbahn, K., and Bohr, E., 1944, *Ark. Nat. Astr. Fys.*, **30***B*, 3.

Torrance, C. C., 1934, *Phys. Rev.*, **46,** 388.

Townsend, A. A., 1940, *Proc. roy. Soc.*, **177,** 357.

Trigg, G., 1952, *Phys. Rev.*, **86,** 506.

Tubis, A., 1956, *Phys. Rev.*, **102,** 1049.

Winther, A., and Kofoed-Hansen, O., 1953, *Dansk. Mat. Fys. Medd.*, **27,** 14.

Wong, C., 1954, *Phys. Rev.*, **95,** 765.

Wu, C. S., Ambler, E., Hayward, R. W., Hoppes, D. D., and Hudson, R. P., 1957, *Phys. Rev.*, **105,** 1412.

Decay Effects in Barium Titanate Ceramics†

By H. L. Allsopp
H. H. Wills Physics Laboratory, University of Bristol‡

[Received June 18, 1957]

It has been pointed out by Mason and Wick (1954) that the usefulness of ceramic $BaTiO_3$ for both condenser and transducer elements is limited by the variation, over long periods, of its dielectric and electro-mechanical constants. Variations arise from a number of causes, but this note is concerned with one type only, the spontaneous variation which results during the period immediately following the application of a strong alternating electric field to a ceramic specimen. This type of variation, in so far as it concerns the dielectric properties, has been described by Rzhanov (1949), Young (1951) and McQuarrie (1953), and the more important of their observations are summarized below. When an alternating field of the order of 5 kv/cm or greater is first applied to a ceramic specimen it is found that (*a*) both the maximum polarization and the dielectric constant ϵ (as measured with a small field) gradually increase in value, (*b*) the hysteresis (D/E) loops become more nearly rectangular, and (*c*) where the D/E loops are initially propellor-shaped, and it is found that the central constriction in these loops fades away when a field is applied. If the material is heated above the Curie temperature, and then allowed to cool with the same field applied, the effects (*a*), (*b*) and (*c*) become more pronounced. After the field has been applied for a certain time (for a few minutes at room temperature) a new stable state is reached; but if the field is then removed the material gradually reverts to its original state in a time of the order of a few hundred hours. We have given the name 'decay effect' to this latter process.

McQuarrie (1953) has interpreted these observations by supposing that there exists a preferred configuration of domains, and, that though the domains may be re-oriented by a strong field (or by other means), they always revert gradually to the original configuration when there is no field applied.

Experiments made in this laboratory have confirmed the above observations, and also extended them in some respects, viz. :—

(1) The electro-mechanical response of ceramic specimens is subject to similar time-dependent variations. It will be shown elsewhere (Allsopp and Gibbs 1957) that the polarization–strain (D/x) loops

† Communicated by the Author.

‡ Now at The Bernard Price Institute of Geophysical Research, University of the Witwatersrand, Johannesburg.

pertaining to most ceramics differ from the ideal parabolic form in that there is a marked flattening of the loops in the vicinity of the vertex. Here we are concerned only with the fact that the extent of the flatness becomes exaggerated when a strong alternating field is first applied, but when the field is removed the loops gradually revert, with the same time-constant as for the D/E loops, to their original (approximately parabolic) form. Figure 1, Pl. 41 shows the nature of the changes in both the D/E and the D/x loops.

It is thought that both the tendency for the D/x loops to become flattened at the vertex and for the D/E loops to become more nearly rectangular indicate that the proportion of c-domain reversals (180° changes in polarization direction) relative to a-domain rotations (90° changes in polarization direction) has increased. This theory is held because the internal stresses that are necessarily associated with a-domain rotations lead one to expect that a-domain changes occur less freely than c-domain changes. Thus we consider that in some of these domains which first undergo a 90° rotation so as to become approximately aligned with the field-direction, the polarization is subsequently reversed at each half-cycle by a single 180° reversal, rather than by successive 90° changes. But after the removal of the field the stresses set up by the original 90° rotation reassert themselves and these domains gradually revert to their original orientation. According to this theory the observed decay in the polarization and also the changes in the loop-shapes can be identified with the latter process.

(2) The decay-effect occurs at all temperatures between the Curie point and −150°C, but it is not known whether the time-constant of the decay is temperature-dependent. However, when a strong field is first applied to a ceramic the time required to reach the new stable state does depend on the temperature, as is shown by the following approximate figures : 1 hour at −150°C, $1\frac{1}{2}$ minutes at 20°C and 10 seconds at 100°C.

Whereas Young (1951) reports that the initial stable condition is not restored by heating the specimen for one hour at 400°C, we find that heating at 1000°C for about the same time does restore the original state.

(3) The decay-effect has been observed in all the ceramics investigated ; however its magnitude varies widely among different samples, and in certain cases the effect is negligible for most practical purposes. The ceramics investigated included samples of widely different grain-sizes, and also samples containing various additives, but there exists no direct correlation between either of these factors and the magnitude of the decay effect. The general tendency is for the effect to be relatively great in samples of high dielectric constant.

A few multi-domain single crystals were also investigated. When a strong alternating field is applied to a virgin crystal both its D/E and its D/x loops undergo changes similar to those observed with ceramics, but the changes are greater in extent, as may be seen from fig. 2, Pl. 42. However, in contrast with the ceramics, the loops pertaining to these

samples do not revert to their original shape when the crystals are stored for long periods. This is in accordance with the fact that in crystals 90° rotations may occur without the establishment of internal stresses.

(4) The polarization initially attainable with some particularly pure $BaTiO_3$ ceramics is significantly smaller than that attainable when they have reached a stable condition after a field has been applied at least once. With these specimens the original virgin state cannot be restored either by prolonged heating at temperatures up to 1250°C or by storage for periods of up to a year. Instead a new stable state is reached, and the material gradually reverts to this state after every subsequent field-application.

References

Allsopp, H. L., and Gibbs, D. F., 1957, *Phil. Mag.* (to be published).
Mason, W. P., and Wick, R. F., 1954, *Proc. Inst. Radio Engrs*, **42**, 1606.
McQuarrie, M., 1953, *J. appl. Phys.*, **24**, 1334.
Rzhanov, J., 1949, *J. Exptl. Theortl. Phys.* (*U.S.S.R.*), **19**, 335.
Young, D. R., 1951, *J. appl. Phys.*, **22**, 523.

Observations on the Distribution of Slip in Polycrystalline Copper†

By D. S. Kemsley
Department of Supply, Aeronautical Research Laboratories, Fishermen's Bend, Melbourne‡

[Received 11 June, 1957]

The slip process in metals produces a macroscopic hardening, a higher stress being required for further slip. However, the amount of shearing in the bands which are first active, increases with increasing deformation (Yamaguchi 1928), and Brown (1952) considers that this continued shearing is due to the initiation of slip on planes close to the active ones, resulting in a lamellar structure of the slip bands. Lamellae have been observed, using the electron microscope, in slip bands in several pure metals, including copper which has been subjected to either unidirectional (Kuhlmann-Wilsdorf and Wilsdorf 1953) or cyclic (Kemsley 1956) stress. Slip therefore is encouraged by prior deformation, rather than prohibited, on planes close to the first active ones.

Brown and Honeycombe (1951) have shown that slip bands in single crystals of pure aluminium only form on the surface when the metal has been previously deformed, either by mechanical abrasion or by prior tensile deformation. The surfaces of annealed crystals subjected to small amounts of strain exhibited evenly dispersed fine slip lines. These workers showed that a similar change in the distribution of slip occurred in single crystals of copper when the surface was abraded. The parallel effect of prior tensile deformation in copper single crystals is apparent from the photographs of Blewitt *et al.* (1954).

The following observations on polycrystalline copper demonstrate that slip bands are formed more readily as strain increases.

Specimens for tensile and rotating-cantilever fatigue tests were machined from high-conductivity copper, and were mechanically polished and then polished electrolytically in orthophosphoric acid solution for 45 minutes. Annealing was carried out in a vacuum at 650°C for 30 minutes. The surfaces retained their high polish after annealing, and no further surface preparation was given prior to testing. A Vickers hardness impression was then made in each annealed specimen, by applying a $2\frac{1}{2}$ kg load for 15 sec. Figure 1, Pl. 43 shows a typical impression (D.P.N. 36·6), diffuse slip bands being visible near the impression at this magnification ($\times 150$).

† Communicated by the Author.

‡ At present at Department of Geophysics, Australian National University, Canberra, Australian Capital Territory.

The tensile specimen was given a plastic strain of 1% and electrolytically polished to remove all slip traces. A hardness impression made on this surface is shown in fig. 2, Pl. 43 (D.P.N. 45·6), sharper slip traces being visible around the impression, and extending over the area of the photograph. Figure 3, Pl. 43 shows a further impression (D.P.N. 94·1) made after training to 30% elongation and electrolytic polishing. Abundant clearly defined slip bands are present, the area exhibiting slip being less than that in fig. 2, Pl. 43.

The fatigue specimen was stressed at $\pm 11\,000$ p.s.i. for 6 000 000 cycles (20% of the expected life) at a frequency of 6000 c.p.m. After electrolytic polishing to remove fatigue slip traces, a hardness impression was made (D.P.N. 71·3). Figure 4, Pl. 43 shows that many clearly developed slip traces have been formed in a relatively small area around the impression. The absence of traces opposite one face of the indentation may be due to an orientation effect of the crystals in that region.

It is clear that the concentration of slip into bands increases with increasing prior tensile and fatigue deformation.

The present observations may account for the fact that, during fatigue testing of electrolytically-polished copper specimens, indications of slip are not visible through the light microscope until the first 1000 cycles of stress are complete (Bullen, Head and Wood 1953). It is suggested that 1000 cycles are required to produce a hardness sufficient for slip bands to form, and that in this initial period, slip occurs on a fine scale, as envisaged by Wood (1955).

Acknowledgment

Thanks are due to the Chief Scientist, Department of Supply, for permission to publish this note.

References

Blewitt, T. H., Coltman, R. R., and Redman, J. K., 1954, *Rept. Conference Defects in Crystalline Solids*, p. 369.

Brown, A. F., 1952, *Advanc. Phys.*, **1**, 427.

Brown, A. F., and Honeycombe, R. W. K., 1951, *Phil. Mag.*, **42**, 1146.

Bullen, F. P., Head, A. K., and Wood, W. A., 1953, *Proc. roy. Soc.* A, **216**, 332.

Kemsley, D. S., 1956–7, *J. Inst. Metals*, **85**, 153.

Wood, W. A., 1955, *Phil. Mag.*, **46**, 1028.

Yamaguchi, K., 1928, *Sci. Papers, Inst. Phys. Chem. Research*, **8**, 289.

On the Longitudinal Polarization of β-particles†

By P. E. Cavanagh, J. F. Turner, C. F. Coleman, G. A. Gard, and B. W. Ridley
Atomic Energy Research Establishment, Harwell

[Received June 19, 1957]

§ 1. Introduction

One of the consequences of parity violation in weak interactions is that β-particles, even from unaligned sources, should be longitudinally polarized. This was pointed out by Jackson *et al.* (1957), also independently by two of us (Cavanagh and Coleman 1957). Calculations by Jackson *et al.* and also by Mandl and Skyrme (private communication), assuming the two component theory of the neutrino, and with certain assumptions concerning the relative magnitudes of the various β-interaction constants, showed that the longitudinal polarization is equal to $-v/c(=-\beta)$, where v is the velocity of the β-particle, for both scalar and tensor interactions. The electron spin points backwards for negatrons and forward for positrons. The polarization becomes complete for high relativistic energies.

§ 2. Design of the Experiment

We have adopted the classical method of studying the electron polarization, in which transverse polarization is detected by measuring the asymmetry in wide angle Coulomb scattering from a high atomic number material (Tolhoek 1956). Since the electron is a Dirac particle it is difficult to turn its spin with respect to its direction of motion in a pure magnetic field. This may, however, be achieved readily in a transverse electric field. In the method employed by Frauenfelder (1957) the electrostatic field established between coaxial cylinders served not only to reorient the spin, but also as an energy selector. This arrangement is however rather inflexible, since the focusing condition differs from that required to turn the spin through 90°.

In the arrangement described here the electrons pass through crossed electric and magnetic fields established at right angles to the trajectories, with the ratio $E/H=\beta$ chosen so that electrons of a particular energy corresponding to β pass through undeflected, while the absolute values of the fields are chosen such that the electron spins are rotated through 90° in traversing the region. The electrons are injected into the crossed fields from a thin lens spectrometer, set so that it also selects a momentum corresponding to β. This is chosen to be $\beta=0{\cdot}6$, since calculations are available for this energy (Sherman 1956), and also since the scattering asymmetry at 90° is a maximum for this energy. The electrons emerging from the crossed fields pass through a field free region, and fall on a thin

† Communicated by the Authors.

gold scatterer placed at an angle of 60° to the beam. The experiment in principle then, consists in the observation of the asymmetry in the scattering of electrons at 90° to the beam. The so-called transmission position was chosen so as to minimize the effects of plural scattering.

§ 3. The Source

^{60}Co was used in this experiment not only because it is a pure Gamow–Teller transition, but also because the maximum intensity in the β-spectrum is at about $\beta=0{\cdot}6$, corresponding to an energy of 128 kev. The thickness of the source (less than $\sim$1 mg/cm^2) is limited by considerations of depolarization due to multiple and to wide angle scattering in the source material. The maximum diameter of the source ($\sim$6 mm) is determined finally by the geometry of the spin-rotator and the H. T. supply available for the electrostatic field. Using 30 curies/g material from Chalk River, a 7 mc source was electroplated on to 1·2 mg/cm^2 aluminium, for which the backscattering should be sufficiently small ($\sim$1%).

§ 4. The Spectrometer and Spin Rotator

Rather than use the crossed fields as a spectrometer we chose to inject from a thin lens spectrometer. This, we anticipated, would not only gain a factor of about five in the transmission, but would also have a very great advantage in reducing both the γ-ray background and the scattering of electrons from the electric field plates. The magnification of the spectrometer was chosen in conjunction with the source diameter so as to optimize the flux of electrons emerging from the crossed fields. The electric field plates were 20 cm long with a gap of 2·8 cm, across which potentials of up to 70 kv were applied symmetrically. The H.T. was kept manually within $\pm\frac{1}{4}$%. The transverse magnetic field of $\sim$100 oersteds was provided by two Helmholtz coils. The magnetic fringing field was matched to the electrostatic one by suitably shaped soft iron shields, the design of which was determined partly by calculation and partly by model experiments. The coil current, as also the spectrometer current, was supplied from amplidyne generators, with a stability of $\sim$1 in 10^3. Stability in the crossed field supplies is important because the energy selection has already been made by the spectrometer.

It had been expected that one half of the electrons passed through the crossed fields would be lost, since there is no lateral focusing. In fact the transmission was reduced by a further factor of about four owing to the effect of fringing fields. Moreover the beam was not symmetrical with respect to the axis of the instrument. A useful consequence of this was that the beam emerged in a much narrower pencil than anticipated, $\sim10^4$ electrons/sec falling within a spot of diameter 1 cm, at the position of the scatterer, 15 cm beyond the exit from the spin rotator. The correct value of the electrostatic field was calculated, and did not require to be set accurately, since only the cosine of the spin angle is involved in the scattering measurement. The corresponding magnetic field was fixed by optimizing the counting rate in a scintillation counter placed on the axis a few inches behind the scatterer position. The usual precautions were taken

to avoid difficulties associated with hysteresis in the soft iron field limiters. The structure of the electron image and the inclination of the beam to the axis were studied by exposing x-ray films in the scatterer position.

§ 5. The Scatterer and the Scattered Electron Detector

Relativistic calculations of the scattering of electrons in a Coulomb field by Mott (1932) and by Bartlett and Watson (1940) have shown that in scattering from mercury, the spin dependent asymmetry at 90° to the direction of incidence is a maximum for an electron energy corresponding to $\beta=0{\cdot}6$. Later calculations by a number of authors, especially Sherman (1956), have shown that particularly at higher energies, the asymmetry increases with increasing angle. However, the scattering cross section also diminishes rapidly with increasing angle, and this, coupled with the difficulties met by Ryu *et al.* (1953) in working at large angles, persuaded us to work at 90°.

The permissible thickness of the scattering foil is determined primarily, it is believed, by the relative importance of plural and single scattering. For a given foil thickness the effects of plural scattering can be minimized by working in the transmission position, scattered electrons emerging from the foil on the side opposite to incidence. References to earlier work on this subject are given by Tolhoek (1956). Such experiments as have been done suggest that foil thicknesses of $\sim$100 μg/cm^2 are required to ensure that corrections due to secondary processes do not become excessive. We have in fact used a range of thicknesses from $\sim$100 μg/cm^2 to $\sim$1 mg/cm^2 in order to estimate the corrections.

These foils, which were made by vacum evaporation of gold on to 20 μg/cm^2 nylon film, were placed at 60° to the incident beam. The thicknesses were determined both by weighing and also by an irradiation technique at the end of the experiment. Arrangements were made so that, without disturbing the vacum, either a gold or an aluminium scatterer could be placed in the beam, or alternatively a 20 μg/cm^2 nylon film alone, carried on an identical supporting frame. The latter served to make background measurements.

A plastic scintillator of thickness equal to the electron range was used to detect the scattered electrons. This subtended a solid angle of 0·01 sphere and linear angles of $\pm 10°$ at the scatterer. The pulse spectrum indicated that mainly elastically scattered electrons were observed, though a low energy tail became more obvious for the thicker scatterers, especially for aluminium. Only counts due to the elastic peak were recorded.

The scatterer holder and detector assembly were arranged so that the azimuthal scattering angle could be varied continuously without affecting the vacuum. A suitably shaped baffle prevented electrons from the walls of the scattering chamber from entering the detector.

§ 6. Instrumental Asymmetries

The principal causes of instrumental asymmetry were :

(i) The electron beam was displaced from the axis: one effect of this was to cause a variation in the solid angle subtended by the detector with azimuth.

By taking the ratio of the scattering from gold and aluminium a quantity was obtained which is independent of this solid angle. The spin dependent asymmetry is reduced by only 10% in taking this ratio. The thicknesses of the two foils were chosen to give comparable counting rates. A second effect was that different parts of the scatterers were exposed to the beam as the azimuth was altered, so variations in foil thickness could be significant. The measurements were repeated with the foils turned (in their planes) through 180°. Then an analysis showed that if the asymmetry is measured by

$$A \sin \phi = \frac{R(\phi) - R^1(\phi+\pi)}{R(\phi) + R^1(\phi+\pi)} \quad . \quad . \quad . \quad . \quad . \quad . \quad (1)$$

where A is the amplitude of the asymmetry, ϕ is the azimuthal scattering angle, and R, R^1 are the ratios of the counting rates from the gold and aluminium scatterers, for the two foil orientations, the effect of the variation in foil thickness is eliminated.

Fig. 1

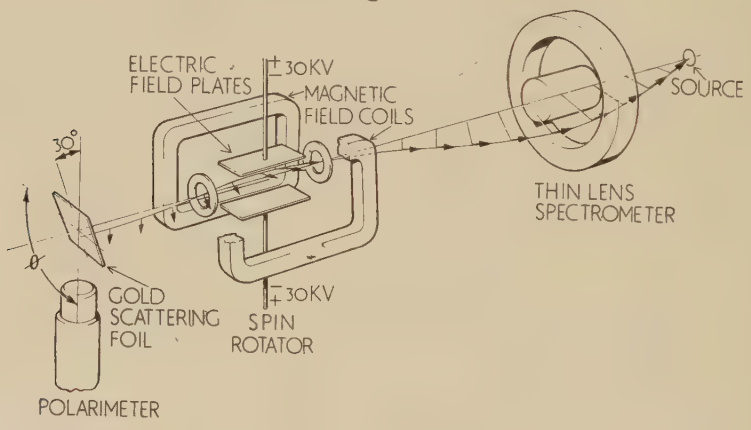

A line drawing of the equipment.

(ii) The beam made a small angle (~3°) with the axis : this caused the polar scattering angle to vary with azimuth, with a corresponding variation in scattering. For an identical dependence of the scattering on polar angle this asymmetry is also eliminated by taking the gold/aluminium ratio. However differences even in single scattering arise due to relativistic and screening effects. Sherman's calculations (which however neglect screening) indicate that the ratio of scattering from gold and aluminium will change by 1% for every 1° off axis of the beam. These effects will be accentuated by plural scattering. The phases of the instrumental asymmetry produced in this way, and the spin dependent asymmetry, will differ in general. If the polar angle of the beam is α and its azimuthal angle is γ, then the resultant asymmetry can be written as

$$A \sin \phi - k\alpha \cos(\phi - \gamma) \quad . \quad . \quad . \quad . \quad . \quad . \quad . \quad (2)$$

where k is a factor which for thin scatterers is 1% per degree, and A is,

as before, the spin dependent part of the asymmetry. The phase and amplitude of this expression are :

$$S=\{A^2+k^2\alpha^2-2Ak\alpha \sin\gamma\}^{\frac{1}{2}} \quad . \quad . \quad . \quad . \quad . \quad (3)$$

$$\tan X=\frac{-k\alpha \cos\gamma}{A-k\alpha \sin\gamma} \quad . \quad . \quad . \quad . \quad . \quad . \quad (4)$$

and we have the relation

$$S \cos X=A-k\alpha \sin\gamma. \quad . \quad . \quad . \quad . \quad . \quad . \quad (5)$$

An investigation of the position of the electron image, using x-ray film, showed that γ changes sign with the spin rotator fields, and that α changes sign with the spectrometer field. Taking an average of quantities measured with opposite signs of γ we have

$$A=\overline{S} \cos \overline{X}. \quad . \quad . \quad . \quad . \quad . \quad . \quad (6)$$

§ 7. Experimental Results

Preliminary measurements were made with very thin scatterers, $\sim 60\,\mu g/cm^2$ gold and $600\,\mu g/cm^2$ aluminium. Under these circumstances the scattered electron counting rate was found to be equal to the background of 1 count/sec. Measurements were confined to four scattering angles at 90° intervals. Immediately effects of the predicted magnitude were observed. The left-right asymmetry in the gold/aluminium counting rate ratio of ~25%, reversed in sign when the electron spin direction was inverted (by reversing the sign of the crossed fields). The sign of the asymmetry was such as to indicate that the β-particles were emitted with backward directed spins, in agreement with theory. These results were reported at the Rochester Conference (1957).

Measurements were now made with thicker scatterers with the purpose of determining corrections due to secondary processes. These were thought to be small at least for $60\,\mu g/cm^2$ gold. Results for $180\,\mu g/cm^2$ gold compared with 1·4 mg/cm² aluminium scattering foils are shown in fig. 2, and confirm the earlier measurements. The experimental points are well fitted by a sine curve with amplitude ~11%, the phase of which changes by 180° when the electron spin direction is reversed, the amplitude remaining essentially unchanged. We have plotted the average of results obtained with opposite signs of spectrometer fields, for which the asymmetry should have the form, obtained by averaging (2) for opposite signs of γ,

$$A \sin\phi-k\alpha \cos\gamma \cos\phi, \quad . \quad . \quad . \quad . \quad . \quad . \quad . \quad (7)$$

i.e. the instrumental and spin dependent asymmetries are 90° out of phase. The phase angle differs only by ~25° from that expected just from spin dependent scattering, indicating that this is the dominant effect.

In the results from thicker scatterers the asymmetry amplitude remains practically constant while the phase angle increases rapidly to ~60° for $770\,\mu g/cm^2$ gold (fig. 3). This shows that the instrumental asymmetry becomes relatively more important for thicker scatterers. Indeed, it

actually increases in absolute magnitude, while the spin dependent term decreases rapidly. One important reason for this decrease is the occurrence of plural scattering. If electrons are scattered twice before entering the detector the spin dependent asymmetry will be very small. It can be shown that A will fall off as $1/(1+ct)$, where c is a constant and t the scatterer thickness, if double scattering is the dominant secondary process. That it does in fact behave in this way is shown in fig. 4, where the reciprocal of the asymmetry is plotted against the scatterer thickness. In this graph corrections have been made for the residual asymmetry expected from the rather thick aluminium comparison scatterers. The spin dependent asymmetry for gold, extrapolated to zero scatterer thickness, is therefore given by the reciprocal of the intercept.

Fig. 2

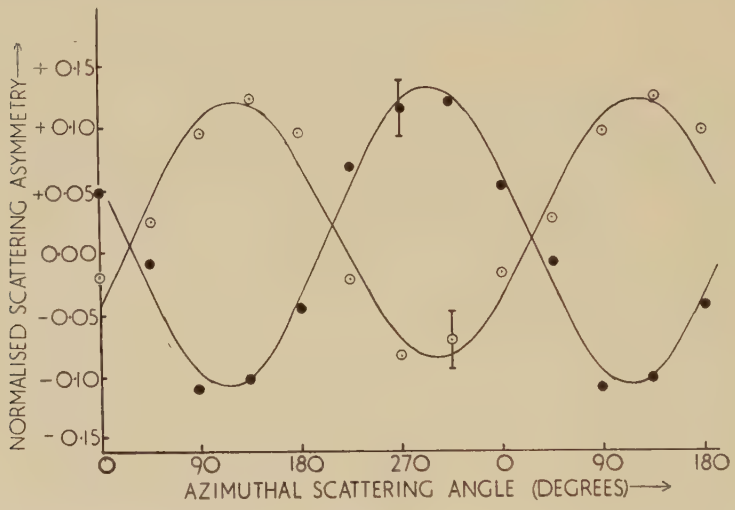

Scattering of 129 kev β-particles by 180 μg/cm^2 gold foil.
● Spins up. ⊙ Spins down.

The contribution of double scattering to the total counting rate can be determined by measuring the latter as a function of foil thickness. One half of the fall off in asymmetry can be ascribed to double scattering on this basis. Depolarization due to multiple scattering in the foil is another possible cause, though a first order calculation based on the Molière theory indicates that this is not likely to exceed 10% for the thickest foil. There is also an uncertainty in the slope of the line since it depends rather critically on the zero from which the angle X is measured. When all these factors and uncertainties are considered, it appears still that about one-third of the fall off in asymmetry remains unaccounted for. Under these circumstances some doubt must remain, concerning the validity of the extrapolation to zero scatterer thickness on the basis of a least squares fit to a straight line through the points.

The value of the asymmetry obtained from the intercept must be corrected for depolarization due to multiple and wide angle scattering in

Fig. 3

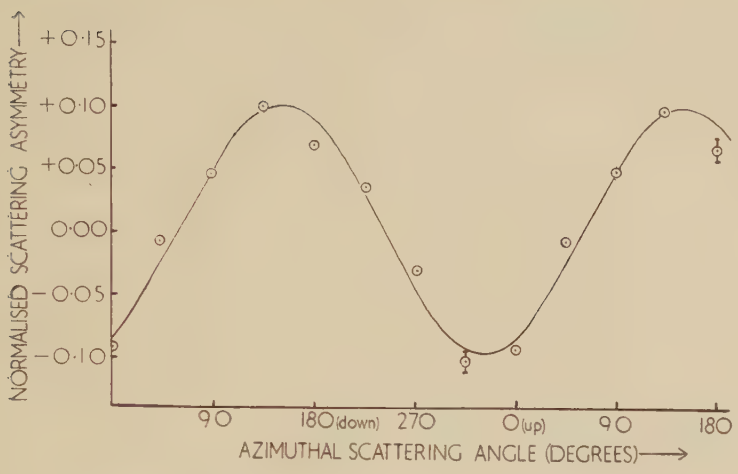

Scattering of 129 kev β-particles by 770 μg/cm² gold foil. Spins down.

Fig. 4

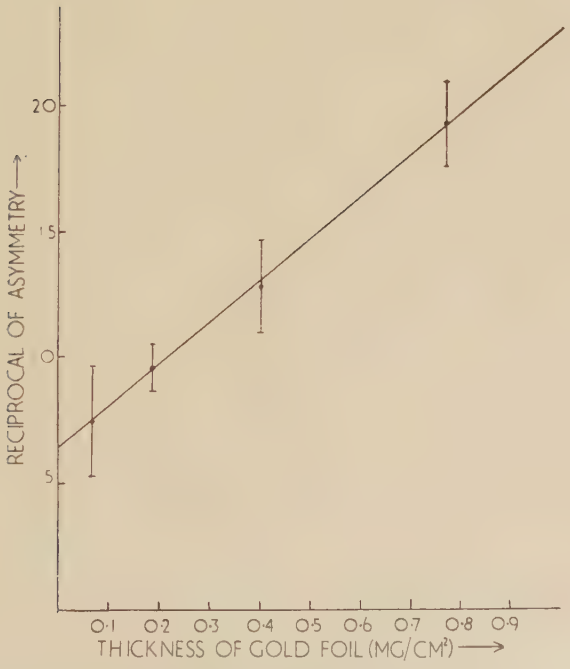

Reciprocal of asymmetry *versus* scatterer thickness.

the source. A first order calculation by Mr. J. S. Bell gave 10% for this correction. The asymmetry is then $(17{\cdot}3\pm3{\cdot}5)\%$, where the inaccuracy quoted arises partly from statistics and partly from the uncertainty in the depolarization correction. Taking Sherman's calculated value for $Z=79$, $\beta=0{\cdot}6$, and for scattering at 90°, of 0·267 we obtain a value for the polarization of $65\pm13\%$. Screening is not included in these calculations. Mohr and Tassie (1954) have made calculations assuming an exponential screening factor, which show differences of $\sim5\%$ at about this energy and scattering angle. We can afford to neglect this correction at present, but it will become important when a really accurate measure of the asymmetry is obtained.

The value is in good agreement with the two component neutrino theory, if the axial vector part of the interaction is assumed to be small. The results of Frauenfelder *et al.*, and Alichanoff, presented at the Rochester Conference at the same time, are also in agreement. The figure obtained by de Waard and Poppema (preprint) of $0{\cdot}49\pm0{\cdot}11$ for $\beta=0{\cdot}66$, measured with a 200 $\mu g/cm^2$ gold scatterer, would be brought into much better agreement if a correction for effects of scatterer thickness were made.

§ 8. Conclusion

Longitudinal polarization of β-particles as a consequence of non-conservation of parity has been demonstrated conclusively. Some of the problems which lie in the way of an accurate determination of the polarization have been investigated. The value obtained for the degree of polarization is an agreement with the two-component theory of the neutrino, and the sign indicates that the β-particles are emitted with backward pointing spins.

Acknowledgments

We would like to acknowledge the help given to us by Drs. T. H. R. Skyrme and F. Mandl in discussions of the theory ; Dr. L. C. W. Hobbis for help in the design of the H.T. set and provision of many of the components ; the several workshops which made the equipment ; Messrs. Boyce, Cox and Schomberg for general assistance in the experiment ; Mr. W. S. Eastwood for obtaining the ^{60}Co. Finally we would like to express our thanks to Sir John Cockcroft who enabled us to undertake the experiment.

References

Cavanagh, P. E., and Coleman, C. F., 1957, *A.E.R.E.* N/M 80.
Bartlett, and Watson, 1940, *Proc. Amer. Acad. Art. Sci.*, **74,** 53.
Frauenfelder, H., *et al.*, 1957, *Phys. Rev.*, **106,** 386.
Jackson, J. D., Treiman, S. B., and Wyld, H. W., 1957, *Phys. Rev.*, **106,** 517.
Mohr, C. B. O., and Tassie, L. F., 1954, *Proc. phys. Soc. Lond. A*, **67,** 711.
Mott, N. F., 1932. *Proc. roy. Soc.* A, **135,** 429.
Ryu, N., Hashimoto, K., Nonaka, I., 1953, *J. Phys. Soc. Japan*, **8,** 575.
Sherman, N., 1956, *Phys. Rev.*, **103,** 1601.
Tolhoek, H. A., 1956, *Rev. mod. Phys.*, **28,** 277.

Note added in proof.—We have now made a measurement of the polarization of 129 kev electrons from ^{198}Au. We obtain a value $P(v/c)=-0{\cdot}97\pm0{\cdot}20$.

The Velocity of Sound in Metals at High Temperatures†

By J. F. W. Bell
The Royal Naval College, Greenwich, S.E.10

[Received in revised form July 9, 1957]

Abstract

A pulse method of measuring the velocity of sound in thin rods over a wide temperature range, in some cases to the melting point, has been developed. The results of measurements on aluminium, brass, nickel, iron, lead, solder and thallium show that, in the strain free condition, the method is a sensitive indication of physical and structural changes.

The changes associated with the onset of a liquid phase, the Curie point, order–disorder and other structural changes are described.

§ 1. Introduction

Plane sound waves can be propagated at a number of velocities which depend on the form of the strain, the boundary conditions and the material. Of the longitudinal velocities two are normally considered. In a rod these have limiting values when the wavelength to diameter ratio approaches zero and infinity. The former can be measured by using a quartz crystal to introduce the vibrations into the material (Mason and McSkimin 1947). The latter can be measured by a resonance method (Bordoni and Nuovo 1954) or by the pulse method described here. The pulse method is particularly suitable for high temperatures when internal damping makes the resonant method very difficult.

§ 2. Method

Composite magnetostrictive delay lines consisting of a nickel tube for launching and receiving pulses and a specimen on which a shoulder was machined at a known distance from the end of the rod were used. The energy of a forward pulse enters the specimen and is echoed back from the shoulder and the end. As the acoustic discontinuities are both of high to low resistance the echoes are of the same polarity. The energy of a pulse in the other direction is damped out by soft pads held in contact with the nickel tube. The received echoes were displayed on a cathode ray oscilloscope.

A typical display is shown in fig. 1. The signal A is due to the passage of the forward pulse through the receiving coil. B is the echo from the junction. C is from the shoulder on the rod and D is the echo from the end. E is a double echo made up of the shoulder–junction–end and the end–junction–shoulder reflections. F is the end–shoulder–end echo.

† Communicated by the Author.

The time delay between C and D is twice the time taken for the pulse to travel from the shoulder to the end. By maintaining this part of the rod at a uniform temperature, the velocity at that temperature can be found. Temperature gradients in the part of the rod leading into the uniform temperature region do not introduce errors as the path is common to both echoes.

Fig. 1

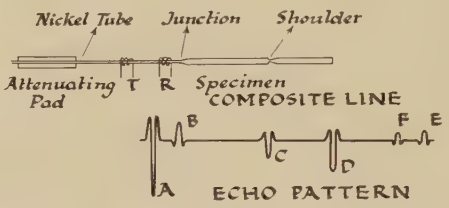

The magnetostrictive line and the corresponding echo pattern. (Polarizing magnets are not shown.)

Fig. 2

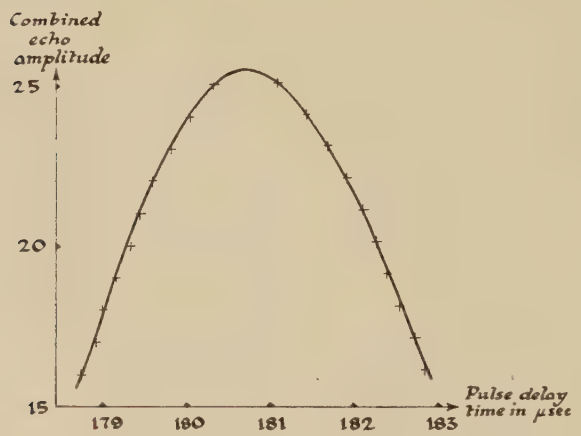

The plot used to determine the echo time interval.

To measure the time interval accurately the pulses were transmitted in pairs. When the pulse delay time is near the C–D echo delay time the first echo from the end combines with the second echo from the shoulder to give a large signal. The combined echo amplitude as a function of pulse delay time is shown in fig. 2. The curve has a well defined peak with a high degree of symmetry. The sensitivity of the time measurement was found to be one part in three or four thousand for an interval of 100 μsec and a pulse length of a few microseconds.

§ 3. Reverberation

The echo pattern has a number of features, not shown in fig. 1, which are important to the accuracy of the measurement. There is a general reverberation background of low amplitude and random structure which

changes with temperature and pulse interval. It is a complex interference pattern of echoes from discontinuities and scattering centres in the line (new reverberations) and high order multiple echoes (old reverberations). The latter are eliminated to a considerable extent by allowing a large time interval between the transmission of pulse pairs. At high temperatures attenuation reduces echo strengths without much reduction in reverberation. This sets the upper limit to observations. With present techniques the limit for iron is 800°C.

§ 4. Electronic Details

Figure 3 shows the block diagram of the circuit for producing the pulse pairs of accurately known interval. The r.f. signal from a crystal calibrated interpolating oscillator is scaled down by a factor of sixteen or twenty-four to give an audio frequence wave of variable frequency from 6 to 11 kc/sec. This wave is converted to pulses and gated to give the pairs of negative current pulses used. The transmitter coil was made aperiodic by a diode across it.

Fig. 3

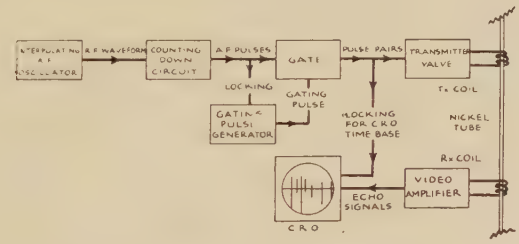

The block diagram of the electronic circuits.

The receiver consists of a coil similar to the transmitter, feeding to a three stage video amplifier. The decrement of the coil was set to a suitably high value by a parallel resistance.

To avoid the dispersion of velocity and the propagation of complex modes it is necessary to keep the pulse length greater than the diameter of the rod. This factor was investigated by trying pulses of various lengths on low velocity specimens. With pulses less than twice the diameter a marked deterioration in echo shape occurred. Pulses longer than about three times the diameter gave well defined echoes and measured velocities independent of pulse length. As the velocity of the specimens used varied from 800 to 5000 m/sec it was necessary to use different pulse lengths for different specimens.

The length of the coils determines the minimum pulse length. Other factors are the resonant frequency of the coils and the duration of the negative pulse applied to the transmitter coil. Having made a coil of chosen length, adjustments of resonant frequency, pulse duration and receiver coil damping were made until the best echoes, judged by

strength and symmetry were obtained. Thick walled nickel tubing gave best results for long pulses, thin for short ones. The echo shape and frequency spectrum of the shortest pulse used is shown in fig. 4.

Fig. 4

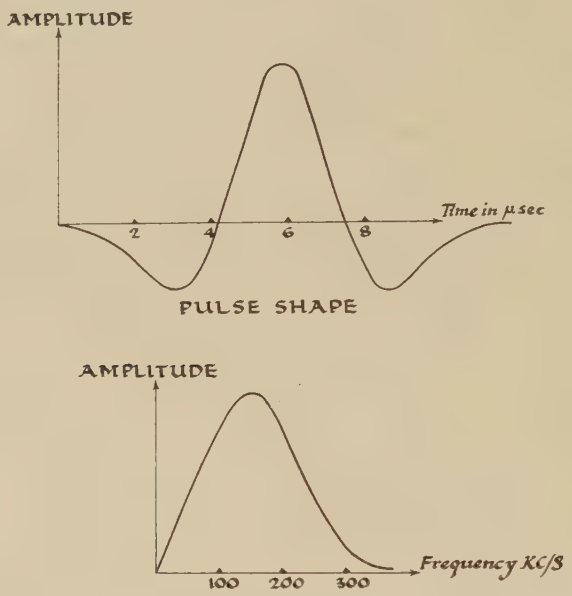

A typical received pulse shape and its frequency spectrum.

§ 5. The Heating System

For temperatures up to 250°C a silicone liquid bath was available. It was used in cases where it was necessary to protect an easily oxidized metal. For the diameters of specimen used the loading of the liquid has a negligible effect on velocity and signal strength.

For most measurements a cylindrical electric furnace was used. It was fitted with a metal heating block 12 in. long with a $\frac{1}{4}$ in. concentric hole for the specimen and thermometers. By careful positioning of the block within the furnace and adjustment of the insulation at the ends, the temperature could be made uniform to within 2°C at 500°C over a 10 in. specimen.

Two pairs of chromel–alumel thermojunctions were used to measure temperature. Figure 5 shows a series of measurements on 70–30 brass for rising and falling temperatures. The coincidence of the readings shows the overall consistency of the measurements and the absence of any significant thermal lag between specimen and thermometers.

§ 6. Results

Measurements were carried out mainly on metals and alloys which are known to have structural and other changes with temperature. A

Fig. 5

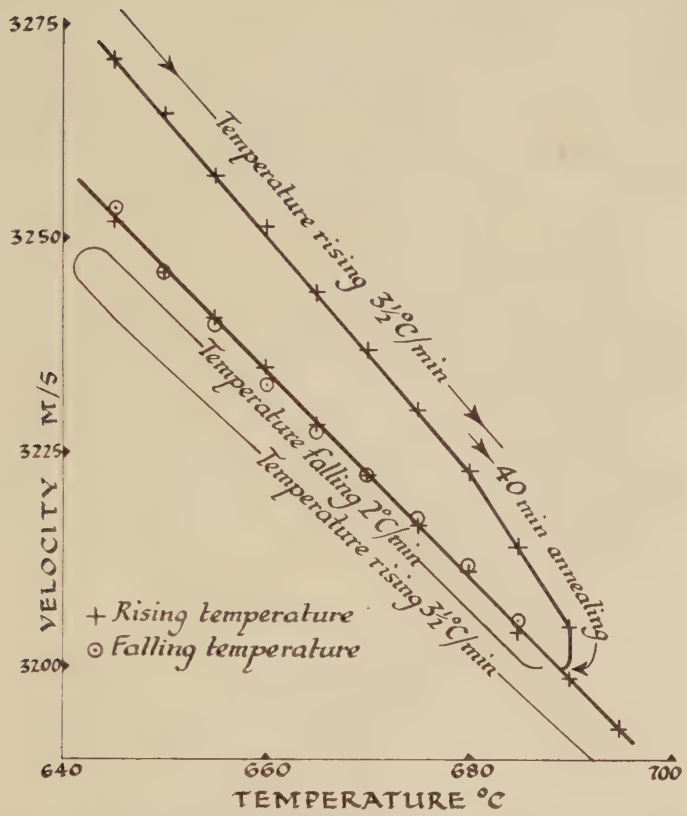

Rising and falling temperature measurements on 70–30 brass.

Fig. 6

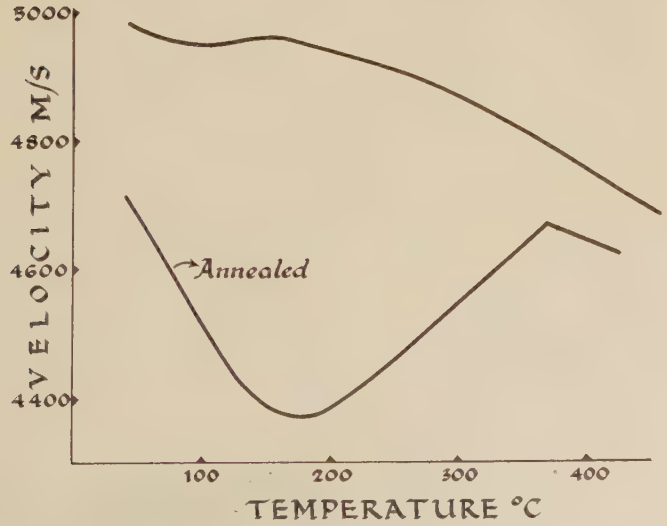

Velocity temperature curves for high purity nickel.

corresponding change in elasticity and hence velocity of sound could be expected.

A good example is the ferromagnetic element nickel. This has a Curie point at 358°C and shows a specific heat anomaly in the region of this temperature. The results on a high purity specimen are shown in fig. 6. These are in almost complete agreement with the results of other investigators. The elasticity at the Curie point found by Siegel and Quimby (1936)—who used a composite resonator technique—was within 2% of the value found here.

§ 7. Lead, Aluminium and 70–30 Brass

Measurements on lead and aluminium were carried out right up to the melting point. Changes due to annealing and, in aluminium, crystal growth were observed. On a well annealed specimen results could be represented by the formula $V=V_{20}(1+a(\theta-20)+b(\theta-20)^2)$ to within the limits of experimental accuracy. The 20°C temperature datum was used as it was at this temperature that the measurements of length were carried out. Values of a, b and V_{20} are given in the table for lead aluminium and 70–30 brass, which also followed the quadratic law.

	V_{20}(m/sec.)	$-a\times10^3$	$-b\times10^6$
Lead	1579	0·43	1·06
Aluminium	5114	0·485	0·102
70–30 Brass	3760	0·153	0·358

It was observed in aluminium that, just below the melting point, the echoes disappeared within a fraction of a degree rise in temperature. They reappeared with equal suddenness as the temperature fell. Metallurgical inspection showed that no melting had taken place. This effect could have been caused by melting at the crystal boundaries where, due to the accumulation of impurities, the melting point would be lower than that of the pure metal.

To test the effect of partial melting throughout a solid the transmission through a junction of two brass rods joined by 50–50 lead–tin solder was investigated. The echoes from beyond the junction cut-off at 180°C, the temperature of the lead–tin eutectic. Thus the acoustic mismatch due to only a thousandth of an inch or so of the solid–liquid mixture was enough to reduce transmission by many tens of decibels. This method thus lends itself to the measurement of eutectic temperatures, even when the composition of the eutectic is not known.

§ 8. Order–Disorder Effects in Brass

60–40 brass is a mixture of the α and β components in the ratio, near the transition region, of about 4 to 1. As the solid is cooled down from

a high temperature the β phase, disordered at high temperatures, begins to become ordered below 454°C.

Measurements on a specimen annealed at 650°C for a few hours were reproducible for rising and falling temperatures. Rates of change of temperature from $-1{\cdot}7$ to $+2{\cdot}7$ degrees per minute were used. A region of the velocity temperature curve is shown in fig. 7. Outside the temperature region where the order–disorder change occurs the curve is similar to that of 70–30 brass. In the region of the change the velocity falls short of the interpolated value by as much as 54 m/sec. This leads to the rather surprising conclusion that a mixture of the two β components has a lower elasticity than either component would have separately.

A further investigation or order—disorder effects is proposed.

Fig. 7

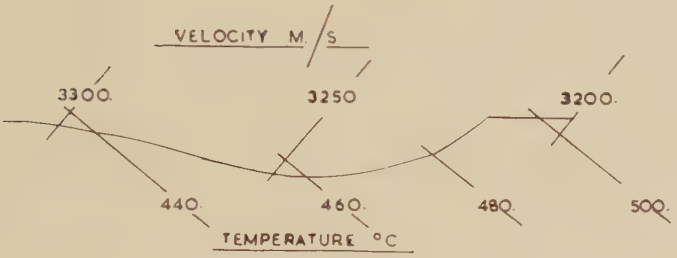

Velocity temperature curves for 60–40 brass in the region of order–disorder change.

§ 9. Thallium

Thallium was chosen because of the structural change from close packed hexagonal to body-centred cubic which it undergoes at 235°C. A short thin rod of thallium was welded, using nitric acid as a flux, to the flat silvered end of a brass rod of the same diameter. The other end of the brass rod was joined to the nickel tube from which the pulses were launched.

Using the longest pulse available, good echoes of the same polarity were obtained from the brass–thallium junction and from the end of the thallium rod. Reverberations were about one-tenth of the echo heights and originated mainly in the thallium.

A typical series of measurements is shown in fig. 8. The complete lack of reproducibility from one temperature cycle to another is at once apparent. This is explained by assuming that the rod, which was only 5 cm long consisted of only a few crystals. The number of these crystals and their orientation would change with each transition and, being elastically anisoptropic, a wide range of velocities would result.

Just below the transition temperature seventeen recrystallizations gave velocities ranging from 840 m/sec to 1050 m/sec. For a similar number of recrystallizations in the body-centred cubic condition the range was 920 m/sec to 1040 m/sec.

During these measurements it was observed that there were great changes in the reverberations between the two echoes. In some cases a well defined echo of either polarity presumably originating at a crystal boundary, would appear. The magnitude of the end echo changed by a factor of about two, being least when reverberations were strong and

Fig. 8

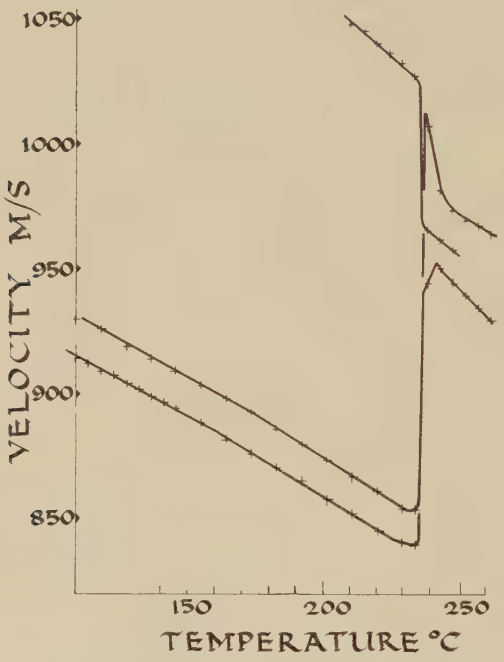

The 235°c phase change in thallium.

greatest when they were small. By observing these features it was possible to deduce the results of recrystallization as it occurred. There were strong indications that on some occasions the specimen consisted of one single crystal.

It is hoped to develop this into a technique for observing crystal growth.

Acknowledgments

The author wishes to thank Professor G. F. Nicholson and the Research Committee of the College for the generous facilities provided, and to thank him and other colleagues for their helpful discussions. The specimens were prepared by Mr. S. G. Smith in the departmental workshop.

References

Bordoni. P. G., and Nuovo, M., 1954, *Nuovo Cim.*, **11,** 127.
Mason, W. P., and McSkimin, H. J., 1947, *J.A.S.A.*, **19,** 464.
Siegel, S., and Quimby, S. L., 1936, *Phys. Rev.*, **49,** 663.

Electron Diffraction from Crystals containing Stacking Faults : I†

By M. J. Whelan and P. B. Hirsch
Crystallographic Laboratory, Cavendish Laboratory, Cambridge, England

[Received June 15, 1957]

Abstract

The dynamical theory of electron diffraction is applied to the case of a plate-like crystal containing a stacking fault. The effect of the fault is to produce a phase difference in the electron waves diffracted by the two parts of the faulted crystal. Expressions for the wave functions and for the corresponding intensities, predicting interference fringes in the region of overlap of the two parts are derived. It is shown that the problem is one of the interference of three coherent waves, in contrast to the case of the wedge crystal where only two waves are involved. At the Bragg reflecting position the spacing of the fringes is half that corresponding to the extinction distance in the crystal. At large deviations from the Bragg position the predictions of the dynamical theory are asymptotic to those of the kinematical theory. The case of two or more stacking faults on neighbouring atomic planes is also considered.

§ 1. Introduction

Interference fringes on transmission electron micrographs of crystalline materials have been studied by several workers. The effects observed so far fall into two well defined categories :

(i) Equal inclination or thickness fringes, commonly called extinction contours, observed in bent plate-like crystals or wedge shaped crystals. These have been discussed theoretically and experimentally by Heidenreich (1949). Kato (1952 a, b, 1953) has developed the dynamical theory of electron diffraction in a form suitable for interpreting the fringes shown by polyhedral crystals, and has applied the theory to explain the fine structure of the electron diffraction patterns.

(ii) Moiré fringes, observed in the region of overlap of two crystals with either different lattice parameters or orientations, (Mitsuishi *et al.* 1951, Seki 1953, Dowell *et al.* 1956, 1957, Hillier 1954, Gard 1956, Hashimoto and Uyeda 1957, Pashley *et al.* 1957). It is generally accepted that these fringes are produced by the interference of electron -waves after successive Bragg reflections in the composite crystal. A distinction between equal thickness and moiré fringes is obtained by noting that in wedge shaped

† Communicated by Professor N. F. Mott, F.R.S.

crystals the former fringes run parallel to the vertex of the wedge, regardless of the operative Bragg reflection, whereas this is not necessarily true of moiré fringes.

In recent work on the transmission microscopy of thin metal foils (Hirsch *et al.* 1956, Bollmann 1957, Whelan *et al.* 1957) fringes have been observed at grain boundaries and stacking faults running obliquely across the foils. These fringes arise as a result of diffraction by two overlapping wedge crystals, and the effects both due to overlap (i.e. as in moiré patterns) and to variation in thickness in the wedge crystals (i.e. as for extinction contours) are important. In order to explain the interference effects in detail it was found necessary to apply the dynamical theory of electron diffraction to the case of overlapping wedge crystals. In this paper the theory is developed for the particular case of a stacking fault in a crystal plate. This case is particularly relevant to the interpretation of the contrast effects observed on transmission micrographs of metals of low stacking fault energy, in which faults can be produced dynamically by splitting of dislocations into partials under the action of the thermal stresses induced by the electron beam.

In the first part of this paper the relevant kinematical theory is developed, and the results are extended to the case of the dynamical theory by simple arguments. The second part of the paper deals with the dynamical theory applied to the Laue case ; absorption is neglected. In the following paper the results are discussed in detail for the case of a stacking fault in a face-centred cubic crystal and are compared with experiments.

Notation†

$\psi(\mathbf{r})$	Electron wave function belonging to crystal wave vector $\mathbf{k}_0$.
$\psi_I(\mathbf{r})$	Incident wave function of wave vector $\boldsymbol{\chi}$.
$\psi_e(\mathbf{r})$	Crystal wave function.
$\mathbf{r}_s$	Position vector at entrance surface.
$\mathbf{r}_e$	Position vector at exit surface.
$\Phi_0(\mathbf{r}_e)$, $\Phi_g(\mathbf{r}_e)$	Wave functions at lower surface of crystal 2.
$\xi_0(\mathbf{r}_e) \equiv \Phi_0(\mathbf{r}_e)/\psi_I$; $\xi_g(\mathbf{r}_e) \equiv \Phi_g(\mathbf{r}_e)/\psi_I$.	
ψ_I	Incident wave amplitude.
$\psi_0^{(i)}$, $\psi_g^{(i)}$ $\psi_0'^{(i)}$, $\psi_g'^{(i)}$	Wave amplitudes of direct (suffix 0) and diffracted (suffix g) waves in crystal 1.
$\phi_0^{(i)}$, $\phi_g^{(i)}$ $\phi_0'^{(i)}$, $\phi_g'^{(i)}$	Wave amplitudes of direct (suffix 0) and diffracted (suffix g) waves in crystal 2.
$\boldsymbol{\chi}$	Incident wave vector ($\chi^2=2meE/h^2$).
$\mathbf{K}$	Kinematical refracted wave in crystal. ($K^2=2me(E+V_0)/h^2=\chi^2+U_0$).
$\mathbf{k}_0^{(i)}$, $\mathbf{k}_g^{(i)}$ $\mathbf{k}_0'^{(i)}$, $\mathbf{k}_g'^{(i)}$	Crystal wave vectors.
$\mathbf{g}$, $\mathbf{h}$	Reciprocal lattice vectors.
$\mathbf{R}$	Shear of crystal 1 relative to crystal 2.

† Vectors are denoted by bold upright type ; the corresponding moduli by normal italic type, e.g. $\mathbf{K}$ and K.

$\alpha \equiv 2\pi \mathbf{g} \cdot \mathbf{R}$	Phase difference between diffracted waves from either side of fault.
$V(r)$	Lattice potential in volts.
V_h	Fourier coefficients of lattice potential. ($U_h \equiv 2me V_h/h^2$).
$\mathbf{n}_1$, $\mathbf{n}_2$	Normals to entrance surface and faulting plane.
$C_1^{(i)}$, $C_1'^{(i)}$	Reflection coefficients for crystal 1.
$C_2^{(i)}$, $C_2'^{(i)}$	Reflection coefficients for crystal 2.
Δk_0	Separation of dispersion surfaces at zone boundary.
$t_0 \equiv 1/\Delta k_0 = K \cos\theta/\lvert U_g \rvert$	Extinction distance for Bragg reflection $\mathbf{g}$.
$t_0' \equiv t_0/\sqrt{(1+x^2)}$	
$\Delta\mathbf{k}_1 \equiv \mathbf{k}_0^{(2)} - \mathbf{k}_0^{(1)}$ $\Delta\mathbf{k}_2 \equiv \mathbf{k}_0'^{(2)} - \mathbf{k}_0'^{(1)}$	Crystal wave vector differences.
θ	Bragg angle for a crystal wave.
$\delta\theta$	Deviation from Bragg angle for crystal wave.
t	Crystal thickness.
t'	Thickness of crystal 1 at a point on fault.
z	Distance measured from centre of foil along direction of t. ($z = \frac{1}{2}t - t'$.)
s	Distance of reciprocal point $\mathbf{g}$ from reflecting sphere in direction t.
y	Perpendicular distance of wave point from zone boundary. ($y \simeq s/2 \tan\theta$.)
x	Parameter indicating deviation from Bragg angle. ($x = 2y \tan\theta/\Delta k_0 \simeq t_0 s = K^2 \sin 2\theta\, \delta\theta/\lvert U_g \rvert$.)

§ 2. Kinematical Theory

Consider a crystal plate with a stacking fault running across it as in fig. 1. The intensity of the transmitted wave at the lower crystal surface in the region of overlap can be obtained by calculating that of the wave diffracted from a column of crystal normal to the surface, shown shaded in fig. 1. The symmetrical Laue case is considered, where the incident and diffracted beams are inclined at approximately the same angle θ to the normal (fig. 2). The amplitude of the wave diffracted from the top half of the column is

$$\exp\{-i\alpha\} \exp\{\pi i(t-t')s\} \sin(\pi t's)/\pi s$$

(where s is the distance along the direction t from the reciprocal lattice point, corresponding to the reflection, to the reflecting sphere), and from the bottom half

$$\exp\{-\pi i t's\} \sin\pi(t-t')s/\pi s.$$

In the first expression $\exp\{-i\alpha\}$ is the phase factor introduced by the relative translation of the two lattices. If $\mathbf{g}$ is the reciprocal lattice

vector corresponding to the reflection excited, and **R** is the shear of crystal 1 relative to crystal 2 (fig. 1), $\alpha = 2\pi \mathbf{g} \cdot \mathbf{R}$.

The total amplitude from the column of crystal is therefore

$$A = (\pi s)^{-1} \exp\{-i\tfrac{1}{2}\alpha\}[\sin(\pi ts - \tfrac{1}{2}\alpha) + \sin\tfrac{1}{2}\alpha \exp\{2\pi is(\tfrac{1}{2}t - t')\}] . \quad (1)$$

and the intensity I is

$$I = (\pi s)^{-2}\{\sin^2(\pi ts - \tfrac{1}{2}\alpha) + \sin^2\tfrac{1}{2}\alpha + 2\sin\tfrac{1}{2}\alpha \sin(\pi ts - \tfrac{1}{2}\alpha)\cos 2\pi zs\} \quad (2)$$

where $z = \frac{1}{2}t - t'$ is equal to the distance measured from the centre of the foil (fig. 1).

Fig. 1

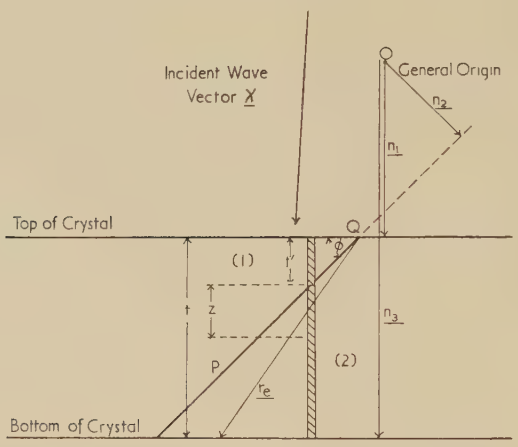

Illustrating the effect of stacking fault on the plane P. The waves scattered by the shaded column in 1 are out of phase by a factor $2\pi \mathbf{g} \cdot \mathbf{R}$ with those scattered by the column in 2, where **R** is the displacement of crystal 1 relative to 2.

A more complete kinematical treatment, taking into account the finite lateral dimensions of the column of crystal, and integrating the intensity scattered over the reflecting sphere, leads to the same expression multiplied by a factor $\pi|U_g|^2/K^2\cos^2\theta$, where U_g is a Fourier coefficient of the lattice potential defined in the notation, and K is the incident electron wave vector after refraction at the surface. It is to be noted that in the kinematical case the term U_g enters in connection with the atomic scattering factors (for electron waves) of the atoms in the unit cell.

The intensity of the transmitted beam is $1-I$, and as z varies along the fault, it is clear that fringes are produced with spacing $\Delta z = s^{-1}$ in the region of overlap of the two crystals. Thus the fringe separation decreases with increasing distance of the reciprocal point from the reflecting sphere, i.e. with increasing deviation from the Bragg angle.

This result may be illustrated graphically in the following way. The intensity of the diffracted wave in the upper half of the crystal is proportional to $\{\sin(\pi t's)/\pi s\}^2$ i.e. it varies sinusoidally and has nodes at spacings

$\Delta z = \Delta t' = s^{-1}$. This oscillation and the corresponding variation of intensity of the direct wave are shown schematically in fig. 3 (*a*). At a depth $t' = n/s$ (where n is an integer) the diffracted wave has zero intensity,

Fig. 2

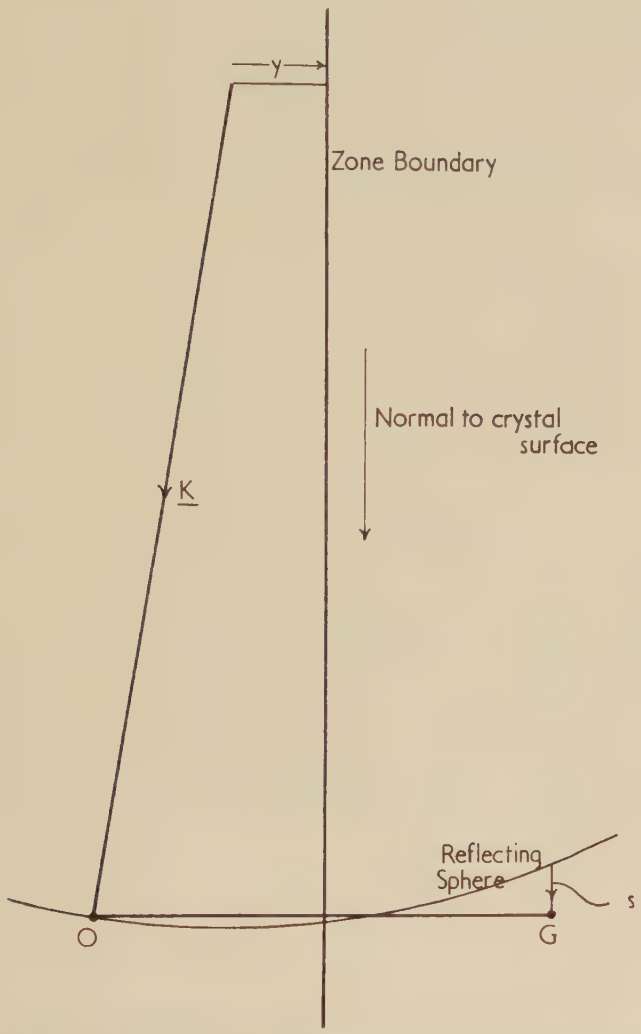

Reflecting sphere construction in the symmetrical Laue case, showing the relation between the parameter s of the kinematical theory and the parameter y of the dynamical theory. The direction of s is normal to the crystal surface, i.e. parallel to the Brillouin zone boundary.

and the intensity of the wave along the direction of incidence is equal to that of the wave incident on the crystal. A fault at this depth can then give rise only to a change of phase of the reflected and transmitted waves, but the intensity remains unaffected. If the fault occurs at any other depth t', the waves reflected on the two sides of the fault have a

phase difference α, and the final intensity at depth t will be different and will depend on t'. Hence a fringe system is formed with periodicity $\Delta z = s^{-1}$. The actual intensity can be obtained from eqn. (2), or by application of the conventional amplitude-phase diagram.

As s decreases the periodicity increases, but for small s dynamical effects become important. In this region the intensity of the reflected wave still varies sinusoidally with depth, but is now proportional to

$$\sin^2 [(\pi t'/t_0)\sqrt{\{1+(t_0 s)^2\}}]/\{1+(t_0 s)^2\}$$

where t_0 is the upper limit of the depth periodicity given by the dynamical theory, and is known as the extinction distance for the particular Bragg

Fig. 3

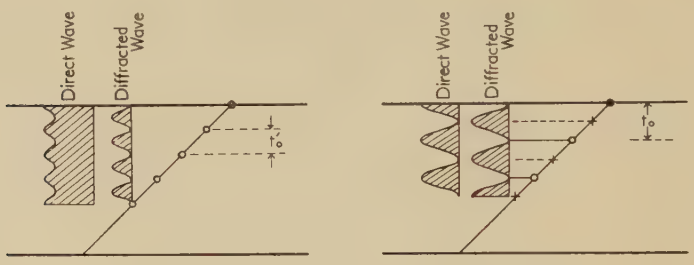

(*a*) (*b*)

(*a*) Schematic diagram of the intensity variation of the direct and diffracted waves in the upper crystal on the kinematical theory ($s \gg 0$). At the points marked with circles the diffracted beam is zero, and the final intensity at the lower surface is the same as for the unfaulted crystal.
(*b*) At the reflecting position, $s=0$, the direct and diffracted waves are equivalent on the dynamical theory. At the points marked with crosses and circles the intensities of direct and diffracted beams are zero. Hence the spacing of the fringes is half that of the corresponding wedge fringes obtained if one half of the faulted crystal is removed.

reflection. Thus, as s decreases, the periodicity of the fringes should increase to $\Delta z = t_0$. When $s=0$ however, the dynamical theory shows that the intensity of the diffracted wave reaches unity, and in fact the direct and diffracted waves are completely equivalent in the crystal in the sense that one has zero intensity when the other has an intensity of unity. In this case therefore the intensity of the transmitted wave will become zero at depths half way between the zeros of the reflected wave, and a fault occurring at these depths will again leave the final intensity unaffected. Therefore, at $s=0$ the periodicity of the fringes will be $\Delta z = \Delta t' = \frac{1}{2}t_0$ as shown schematically in fig. 3 (*b*).

In this simple way it is easy to see how the fringes in the kinematical region are related to those in the dynamical region. The detailed intensity distribution near the reflecting position can however only be obtained from the complete theory.

§ 3. General Dynamical Theory

The dynamical theory of electron diffraction as developed by Bethe (1928) for the Bragg case, has been extended by several authors, notably Thomson and Cochran (1939), MacGillavry (1940), Heidenreich (1949), and Kato (1952 a, b), to cover the Laue case. In this section the theory as developed by Kato is outlined, since it forms the most useful starting point for a discussion of faulted crystals. The notation is similar to but not identical with that employed by Kato.

The dynamical theory of electron diffraction deals with the possible self consistent wave fields which may exist inside a crystal. These are given by the wave functions $\psi(\mathbf{r})$ satisfying the Schrödinger equation

$$\nabla^2\psi(\mathbf{r})+\frac{8\pi^2me}{h^2}[E+V(\mathbf{r})]\psi(\mathbf{r})=0. \quad . \quad . \quad . \quad . \quad . \quad (3)$$

The periodic lattice potential $V(\mathbf{r})$ is written as a Fourier series

$$V(\mathbf{r})=\sum_{-\infty}^{+\infty}V_h \exp\{2\pi i\mathbf{h}\cdot\mathbf{r}\}$$

where $\mathbf{h}$ denotes a vector in the reciprocal lattice vector. There exist solutions of (3) of the form

$$\psi(\mathbf{r})=\sum_g \psi_g \exp\{2\pi i\mathbf{k}_g\cdot\mathbf{r}\}$$

where $\mathbf{k}_g=\mathbf{k}_0+\mathbf{g}$. On substitution of the expressions for $\psi(\mathbf{r})$ and $V(\mathbf{r})$ in (3), one arrives at a system of linear homogeneous equations

$$(K^2-k_g^2)\psi_g+\sum_h{}'\psi_{g-h}U_h=0 \quad . \quad . \quad . \quad . \quad . \quad . \quad . \quad (4)$$

where the prime indicates that summation over $h=0$ is omitted. The solution of the eqns. (4) gives the Fourier amplitudes ψ_g and the energy E for a value $\mathbf{k}_0$ of the crystal wave vector. The assumption is now made that only the amplitudes ψ_0 and ψ_g have appreciable values. Physically this approximation means that only one Bragg reflection is excited in the crystal. Experiments by the authors have shown that this is a reasonable approximation in most regions where interference effects are observed for the case of foils about 1000 Å thick.

The secular eqn. (4) then reduces to

$$\begin{pmatrix} (K_0^2-k_0^2) & U_{0g} \\ U_{g0} & (K_g^2-k_g^2) \end{pmatrix}\begin{pmatrix} \psi_0 \\ \psi_g \end{pmatrix}=0 \quad . \quad . \quad (5)$$

where $$K_0^2=\chi^2+U_{00}, \quad K_g^2=\chi^2+U_{gg}.$$

The quantities U_{ij}, called the dynamical potentials, are related to the lattice potentials U_i by the equations

$$\left.\begin{aligned} U_{00}&=U_0-\sum_h{}''U_hU_{-h}/(K^2-k_h^2)\\ U_{gg}&=U_0-\sum_h{}''U_{h-g}U_{g-h}/(K^2-k_h^2)\\ U_{0g}&=U_{-g}-\sum_h{}''U_{-h}U_{h-g}/(K^2-k_h^2)\\ U_{g0}&=U_g-\sum_h{}''U_hU_{g-h}/(K^2-k_h^2)\end{aligned}\right\} \quad . \quad . \quad . \quad . \quad (6)$$

where the double prime indicates that summation over $h=0$, and $h=g$ is omitted. The energy values E belonging to $\mathbf{k}_0$ are then given by the solutions of

$$\begin{vmatrix} (K_0^2-k_0^2) & U_{0g} \\ U_{g0} & (K_g^2-k_g^2) \end{vmatrix}=0. \quad . \quad . \quad . \quad . \quad (7)$$

We first note that K_0, K_g, K, k_0 and k_g do not differ appreciably owing to the smallness of the lattice potentials ($\sim$10 volts) compared to the initial electron accelerating potential ($\sim 10^5$ volts). Furthermore, for the case of fast electrons ($E\sim$80 kv) the difference between the dynamical and lattice potentials becomes negligible for the case of one strong Bragg reflection because of the magnitude of the factors $(K^2-k_h^2)$.

Equation (7) then reduces to

$$(K-k_0)(K-k_g)=|U_g|^2/4K^2. \quad . \quad . \quad . \quad . \quad . \quad . \quad (8)$$

Equation (8) shows that the surface of constant energy in $\mathbf{k}$ space is hyperbolic close to a Bragg reflection, i.e. when $\mathbf{k}_0$ is near the Brillouin zone boundary associated with the reciprocal lattice point $\mathbf{g}$. This so called dispersion surface shown in fig. 4 has asymptotes $k_0=K$, $k_g=K$, which are strictly spheres of large radius centred about O and G. $S_0{}^d$ and $S_g{}^d$ represent the asymptotes of the dispersion surface near the zone boundary $\mathbf{g}$. D is a wave point on the dispersion surface so that $\overrightarrow{DO}$ and $\overrightarrow{DG}$ represent the wave vectors of the two large terms in the crystal wave function. They may be interpreted directly as incident and diffracted crystal waves. $S_0{}^k$ and $S_g{}^k$ represent the surfaces of constant energy on a kinematical theory where the lattice potentials U_h, including the refractive term U_0, are neglected. It will be noted that there are two branches of the dispersion surface $B^{(1)}$ and $B^{(2)}$, with corresponding wave vectors $\mathbf{k}_0{}^{(1)}$ and $\mathbf{k}_0{}^{(2)}$.

For any point D on the dispersion surface, a reflection coefficient $C^{(i)}$ for the wave $\mathbf{k}_0{}^{(i)}$ may be defined by

$$C^{(i)}=\psi_g{}^{(i)}/\psi_0{}^{(i)}.$$

It is convenient at this stage to introduce a parameter x which indicates a deviation from the Bragg angle θ. In fig. 4, y is the perpendicular distance of D from the zone boundary, and the deviation $\delta\theta$ of the crystal wave vector from the Bragg angle is marked.

In terms of y,

$$x=2y\tan\theta/\Delta k_0 \quad . \quad . \quad . \quad . \quad . \quad . \quad . \quad (9\,a)$$

where Δk_0 is the separation of the two branches of the dispersion surface at the zone boundary. In this paper the positive sense of x is taken as outwards through the zone boundary. Although the parameters y and $\delta\theta$, as introduced here, refer specifically to the crystal waves, consideration of the results of § 4 shows that to a good approximation, they may also be taken as referring to the incident and kinematically transmitted waves $\boldsymbol{\chi}$ and $\mathbf{K}$. The approximation holds near the symmetrical Laue case,

Fig. 4

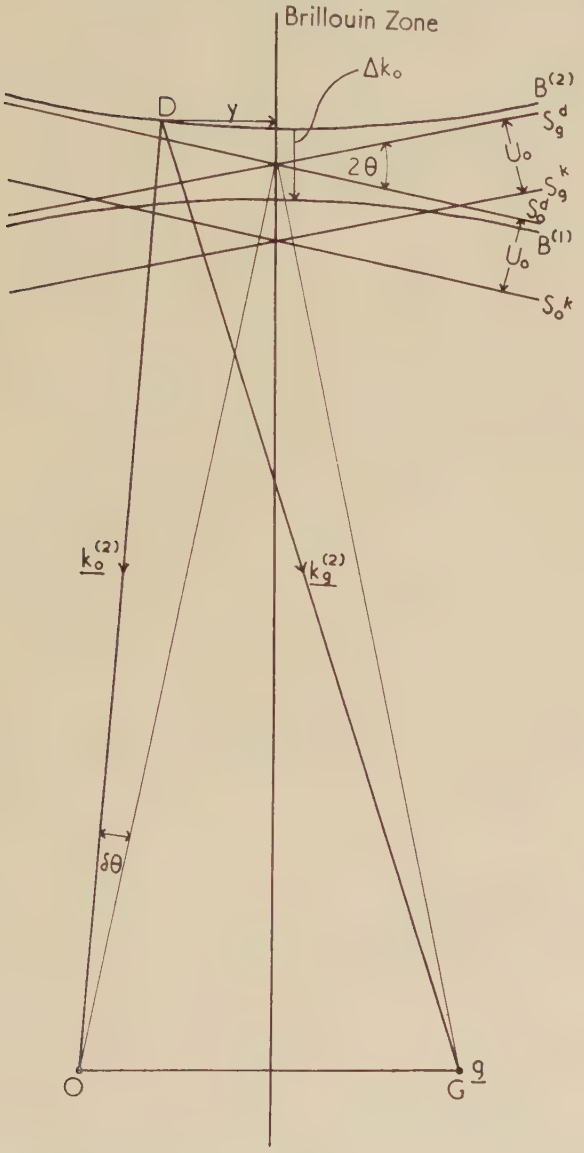

Dispersion surface of constant energy at the Brillouin zone boundary **g**. The complete surface is obtained by the revolution of the hyperbola about OG. D is a wave point on the surface, so that $\overrightarrow{DO}$ and $\overrightarrow{DG}$ are possible wave vectors $k_0^{(2)}$ and $k_g^{(2)}$ in the crystal. $S_0^{(k)}$, $S_0^{(d)}$ and $S_g^{(k)}$, $S_g^{(d)}$ are spheres of large radius χ and K centred about O and G.

and for fast electrons this implies that the incident wave vector $\boldsymbol{\chi}$ must be nearly perpendicular to the entrance surface of the crystal. In this approximation y may be written in terms of s defined in fig. 2.

$$y=s/2\tan\theta. \quad . \quad . \quad . \quad . \quad . \quad . \quad . \quad . \quad . \quad (9\,b)$$

Then (9 *a*) becomes

$$x=s'\Delta k_0=t_0 s \quad . \quad . \quad . \quad . \quad . \quad . \quad . \quad . \quad . \quad (9\,c)$$

where t_0 is the extinction distance defined as $(\Delta k_0)^{-1}$.
From eqn. (8) and fig. 4 it is seen that $\Delta k_0=|U_g|/K\cos\theta$, so that

$$t_0=K\cos\theta/|U_g| \quad . \quad . \quad . \quad . \quad . \quad . \quad . \quad . \quad . \quad (9\,d)$$

In terms of $\delta\theta$,

$$x=2Kt_0\sin\theta\,\delta\theta=K^2\sin 2\theta\,\delta\theta/|U_g|. \quad . \quad . \quad . \quad . \quad (9\,e)$$

Equation (7) then leads to

$$C^{(i)}=2K(k_0^{(i)}-K)/U_{-g}=U_g/2K(k_g^{(i)}-K). \quad . \quad . \quad (10\,a)$$

Consideration of the geometry of the dispersion surface then enables $(k_0^{(i)}-K)$ and $(k_g^{(i)}-K)$ to be expressed in terms of the parameter x leading to the following expression for $C^{(i)}$.

$$C^{(1)}=x-\sqrt{(1+x^2)}. \quad . \quad . \quad . \quad . \quad . \quad . \quad . \quad . \quad (10\,b)$$

$$C^{(2)}=x+\sqrt{(1+x^2)}. \quad . \quad . \quad . \quad . \quad . \quad . \quad . \quad . \quad (10\,c)$$

Then the general solution $\psi_c(\mathbf{r})$ of the wave equation in the crystal in the approximation considered is

$$\psi_c(\mathbf{r})=\sum_i \psi_0^{(i)}[\exp\{2\pi i\mathbf{k}_0^{(i)}\cdot\mathbf{r}\}+C^{(i)}\exp\{2\pi i\mathbf{k}_g^{(i)}\cdot\mathbf{r}\}]. \quad . \quad (11)$$

§ 4. Boundary Conditions

In the application of the dynamical theory to finite crystals account must be taken of the boundary conditions at the various crystal surfaces. In the Laue case a plane wave

$$\psi_I(\mathbf{r})=\psi_I\exp\{2\pi i\boldsymbol{\chi}\cdot\mathbf{r}\}$$

of vacuum wave vector $\boldsymbol{\chi}$ is incident on a plane surface of the crystal. The boundary conditions are

$$\psi_I(\mathbf{r}_s)=\psi_c(\mathbf{r}_s) \quad . \quad . \quad . \quad . \quad . \quad . \quad . \quad . \quad (12\,a)$$

$$\frac{\partial\psi_I(\mathbf{r}_s)}{\partial n_1}=\frac{\partial\psi_c(\mathbf{r}_s)}{\partial n_1} \quad . \quad . \quad . \quad . \quad . \quad . \quad . \quad . \quad (12\,b)$$

where $\mathbf{r}_s$ is a position vector of a point at the interface, and n_1 indicates differentiation along the normal.

In fig. 5, E is the wave point of the incident wave in vacuum so that EO represents the vacuum wave vector $\boldsymbol{\chi}$. It is then possible to satisfy (12 *a*) if crystal waves $\psi_0^{(1)}$ and $\psi_0^{(2)}$ are chosen which satisfy

$$\psi_0^{(1)}\exp\{2\pi i\mathbf{k}_0^{(1)}\cdot\mathbf{r}_s\}+\psi_0^{(2)}\exp\{2\pi i\mathbf{k}_0^{(2)}\cdot\mathbf{r}_s\}=\psi_I\exp\{2\pi i\boldsymbol{\chi}\cdot\mathbf{r}_s\} \quad (13\,a)$$

$$\psi_g^{(1)}\exp\{2\pi i\mathbf{k}_g^{(1)}\cdot\mathbf{r}_s\}+\psi_g^{(2)}\exp\{2\pi i\mathbf{k}_g^{(2)}\cdot\mathbf{r}_s\}=0. \quad . \quad (13\,b)$$

Equations (13 *a*) and (*b*) can be satisfied only when the components of $\boldsymbol{\chi}$, $\mathbf{k}_0^{(1)}$, $\mathbf{k}_0^{(2)}$ tangential to the surface are equal.

Then the wave points $D^{(1)}$ and $D^{(2)}$ of $\mathbf{k}_0^{(1)}$ and $\mathbf{k}_0^{(2)}$ lie at the intersections with the two branches of the dispersion surface of the normal $\mathbf{n}_1$ to the entrance surface passing through E. It should be noted that in general, if the normal to the entrance surface does not lie in the plane EOG, $D^{(1)}$ and $D^{(2)}$ will be outside the plane of fig. 5.

Fig. 5

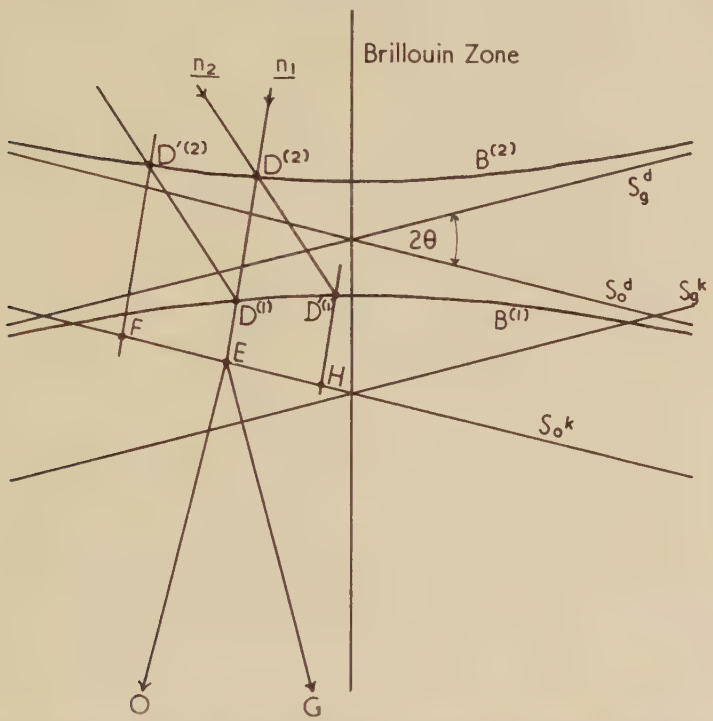

Dispersion surface construction for ensuring continuity of tangential components of wave vectors at the entrance surface and faulting plane. $\overrightarrow{EO}$ is the wave vector $\boldsymbol{\chi}$ of the incident wave. $\mathbf{n}_1$ and $\mathbf{n}_2$ are normal to the entrance surface and faulting plane. Note that in general $D^{(i)}$ and $D'^{(i)}$ do not lie in the plane EOG.

The wave functions thus obtained do not in general satisfy (12 *b*). This point has been considered more fully by Bethe (1928), Thompson and Cochrane (1939), and Kato (1952 a). When the normal components of the wave vectors are large compared with the normal components of their differences, the equality of tangential components implies continuity of the normal derivatives. The approximation, which is equivalent to neglecting surface reflected waves, is valid for the case of high energy electrons considered here. Furthermore, this approximation means that the crystal waves are determined only by the boundary conditions at the entrance surface, and are independent of those at the

exit surface, so that in considering the propagation of electrons in overlapping crystals the boundary conditions at the several interfaces may be applied consecutively and independently.

Equations (13 *a*) and (*b*) therefore reduce to

$$\psi_0^{(1)} \exp\{2\pi i \mathbf{k}_0^{(1)} \cdot \mathbf{n}_1\} + \psi_0^{(2)} \exp\{2\pi i \mathbf{k}_0^{(2)} \cdot \mathbf{n}_1\} = \psi_I \exp\{2\pi i \boldsymbol{\chi} \cdot \mathbf{n}_1\} \quad (14\,a)$$

$$C^{(1)}\psi_0^{(1)} \exp\{2\pi i \mathbf{k}_g^{(1)} \cdot \mathbf{n}_1\} + C^{(2)}\psi_0^{(2)} \exp\{2\pi i \mathbf{k}_g^{(2)} \cdot \mathbf{n}_1\} = 0. \quad (14\,b)$$

where $\mathbf{n}_1$ is the normal to the entrance surface from the origin of coordinates (O in fig. 1).

The solution of eqns. (14 *a*) and (*b*) gives

$$\psi_0^{(1)} = \frac{-C^{(2)}}{(C^{(1)} - C^{(2)})} \psi_I \exp\{2\pi i(\boldsymbol{\chi} - \mathbf{k}_0^{(1)}) \cdot \mathbf{n}_1\} \quad . \quad . \quad . \quad . \quad (15\,a)$$

$$\psi_0^{(2)} = \frac{C^{(1)}}{(C^{(1)} - C^{(2)})} \psi_I \exp\{2\pi i(\boldsymbol{\chi} - \mathbf{k}_0^{(2)} \cdot \mathbf{n}_1\} \quad . \quad . \quad . \quad . \quad . \quad (15\,b)$$

$$\psi_g^{(1)} = \frac{-C^{(1)}C^{(2)}}{(C^{(1)} - C^{(2)})} \psi_I \exp\{2\pi i(\boldsymbol{\chi} - \mathbf{k}_0^{(1)}) \cdot \mathbf{n}_1\} \quad . \quad . \quad . \quad . \quad (15\,c)$$

$$\psi_g^{(2)} = \frac{C^{(1)}C^{(2)}}{(C^{(1)} - C^{(2)})} \psi_I \exp\{2\pi i(\boldsymbol{\chi} - \mathbf{k}_0^{(2)}) \cdot \mathbf{n}_1\}. \quad . \quad . \quad . \quad . \quad (15\,d)$$

§ 5. The Case of a Crystal Containing a Stacking Fault

5.1. *Modification of Reflection Coefficients*

The extension of the theory to a crystal containing a stacking fault follows directly from the preceeding discussion. Figure 1, represents schematically a plane wave of vacuum wave vector $\boldsymbol{\chi}$ incident on a plate crystal containing a stacking fault on an intersecting plane P. The effect of the stacking fault is to translate region 1 relative to region 2 by a vector $\mathbf{R}$ which is not a lattice vector. It was shown in § 2 by a kinematical argument that interference effects are expected in the overlap region since the electrons scattered into the Bragg reflection by the regions 1 and 2 will be out of phase by a factor $\alpha = 2\pi \mathbf{g} \cdot \mathbf{R}$ owing to the relative shear. This phase factor enters into the dynamical theory also when we consider the Fourier expansion of the lattice potential in both halves of the crystal, where we have

$$V_1(\mathbf{r} + \mathbf{R}) = V_2(\mathbf{r})$$

which leads directly to

$$U_{2g} = U_{1g} \exp\{i\alpha\}$$

where the subscripts 1 and 2 refer to the two halves of the crystal.

Then the effect of the stacking fault may be included in the dynamical theory by introducing the phase factor into eqn. (10 *a*) as follows

$$C_2^{(i)} = U_{2g}/2K(k_g^{(i)} - K) = C_1^{(i)} \exp\{i\alpha\}. \quad . \quad . \quad . \quad . \quad (16)$$

5.2. *Crystal Wave Functions*

In accordance with the boundary conditions discussed in § 4 the wave points of the wave vectors in crystal 1 are given by $D^{(1)}$ and $D^{(2)}$ in

fig. 5. The possible wave points in crystal 2 derived from those in 1 are found by a similar construction using the normal $\mathbf{n}_2$ to the faulting plane P. In this way four wave points $D^{(i)}$ and $D'^{(i)}$ are obtained, lying in a plane containing the normals to the crystal surfaces. In the general case there are four such wave points for each side of the fault, this being the case when the waves in 2 propagate through a second parallel stacking fault. It is of interest for the discussion of overlapping stacking faults to derive equations for this general case, remembering that in crystal 1

$$\psi_0'^{(i)}=\psi_g'^{(i)}=0.$$

The corresponding wave functions are enumerated as follows

Crystal 1 : $\psi_0^{(i)} \exp\{2\pi i\mathbf{k}_0^{(i)}\cdot\mathbf{r}\}$, $\psi_0'^{(i)} \exp\{2\pi i\mathbf{k}_0'^{(i)}\cdot\mathbf{r}\}$ } Direct waves

$\psi_g^{(i)} \exp\{2\pi i\mathbf{k}_g^{(i)}\cdot\mathbf{r}\}$, $\psi_g'^{(i)} \exp\{2\pi i\mathbf{k}_g'^{(i)}\cdot\mathbf{r}\}$ } Diffracted waves

Crystal 2 : $\phi_0^{i} \exp\{2\pi i\mathbf{k}_0^{(i)}\cdot\mathbf{r}\}$, $\phi_0'^{(i)} \exp\{2\pi i\mathbf{k}_0'^{(i)}\cdot\mathbf{r}\}$ } Direct waves

$\phi_g^{(i)} \exp\{2\pi i\mathbf{k}_g^{(i)}\cdot\mathbf{r}\}$, $\phi_g'^{(i)} \exp\{2\pi i\mathbf{k}_g'^{(i)}\cdot\mathbf{r}\}$ } Diffracted waves.

The continuity of the tangential components of wave vectors then gives the following relations for wave amplitudes on either side of the fault.

$$\left.\begin{aligned}
&\psi_0^{(1)} \exp\{2\pi i\mathbf{k}_0^{(1)}\cdot\mathbf{n}_2\}+\psi_0'^{(2)} \exp\{2\pi i\mathbf{k}_0'^{(2)}\cdot\mathbf{n}_2\}\\
&\quad=\phi_0^{(1)} \exp\{2\pi i\mathbf{k}_0^{(1)}\cdot\mathbf{n}_2\}+\phi_0'^{(2)} \exp\{2\pi i\mathbf{k}_0'^{(2)}\cdot\mathbf{n}_2\}\\
&\psi_0^{(2)} \exp\{2\pi i\mathbf{k}_0^{(2)}\cdot\mathbf{n}_2\}+\psi_0'^{(1)} \exp\{2\pi i\mathbf{k}_0'^{(1)}\cdot\mathbf{n}_2\}\\
&\quad=\phi_0^{(2)} \exp\{2\pi i\mathbf{k}_0^{(2)}\cdot\mathbf{n}_2\}+\phi_0'^{(1)} \exp\{2\pi i\mathbf{k}_0'^{(1)}\cdot\mathbf{n}_2\}\\
&\psi_g^{(1)} \exp\{2\pi i\mathbf{k}_g^{(1)}\cdot\mathbf{n}_2\}+\psi_g'^{(2)} \exp\{2\pi i\mathbf{k}_g'^{(2)}\cdot\mathbf{n}_2\}\\
&\quad=\phi_g^{(1)} \exp\{2\pi i\mathbf{k}_g^{(1)}\cdot\mathbf{n}_2\}+\phi_g'^{(2)} \exp\{2\pi i\mathbf{k}_g'^{(2)}\cdot\mathbf{n}_2\}\\
&\psi_g^{(2)} \exp\{2\pi i\mathbf{k}_g^{(2)}\cdot\mathbf{n}_2\}+\psi_g'^{(1)} \exp\{2\pi i\mathbf{k}_g'^{(1)}\cdot\mathbf{n}_2\}\\
&\quad=\phi_g^{(2)} \exp\{2\pi i\mathbf{k}_g^{(2)}\cdot\mathbf{n}_2\}+\phi_g'^{(1)} \exp\{2\pi i\mathbf{k}_g'^{(1)}\cdot\mathbf{n}_2\}
\end{aligned}\right\} \quad (17)$$

For the case of a single stacking fault eqns. (17), with the help of eqns. (15) and (16), lead to the following expressions for the wave amplitudes in crystal 2. The origin of coordinates is taken at Q, fig. 1, and the subscript j is dropped from the terms $C_j^{(i)}$ after application of (16)

$$\phi_0^{(1)}=\frac{C^{(1)}C^{(2)}}{(C^{(1)}-C^{(2)})^2}\left[\frac{C^{(2)}}{C^{(1)}}-\exp\{-i\alpha\}\right]\psi_{\mathrm{I}} \quad . \quad . \quad . \quad (18\,a)$$

$$\phi_0'^{(1)}=\frac{C^{(1)}C^{(2)}}{(C^{(1)}-C^{(2)})^2}[\exp\{-i\alpha\}-1]\psi_{\mathrm{I}} \quad . \quad . \quad . \quad . \quad . \quad (18\,b)$$

$$\phi_0^{(2)}=\frac{C^{(1)}C^{(2)}}{(C^{(1)}-C^{(2)})^2}\left[\frac{C^{(1)}}{C^{(2)}}-\exp\{-i\alpha\}\right]\psi_{\mathrm{I}} \quad . \quad . \quad . \quad (18\,c)$$

$$\phi_0'^{(2)}=\frac{C^{(1)}C^{(2)}}{(C^{(1)}-C^{(2)})^2}[\exp\{-i\alpha\}-1]\psi_{\mathrm{I}}. \quad . \quad . \quad . \quad . \quad . \quad (18\,d)$$

The assumption has been made that the $C^{(i)}$'s are the same for both wave points $D^{(i)}$ and $D'^{(i)}$ on a branch of the dispersion surface, and an average x representing the four wave points is used. The approximation is justified by the following argument. With high energy electrons the Bragg angles are small, and if the incident beam is approximately normal to the plane of the foil, $\mathbf{n}_1$ in fig. 6 is practically parallel to the zone boundary. Figure 6 shows the group of four wave points $D^{(i)}$ and $D'^{(i)}$ at a mean distance y from the zone boundary. The angle ϕ is the wedge angle of fig. 1. If the plane containing $D^{(i)}$ and $D'^{(i)}$ makes an angle γ with the Brillouin zone boundary, it is seen that the separation Δy of $D^{(2)}$ and $D'^{(2)}$ is given by $\Delta y = \Delta k_1 \tan\phi \sin\gamma$ where Δk_1 is the wave vector difference indicated in fig. 6 (equal to $D^{(2)}D^{(1)}$).

Fig. 6

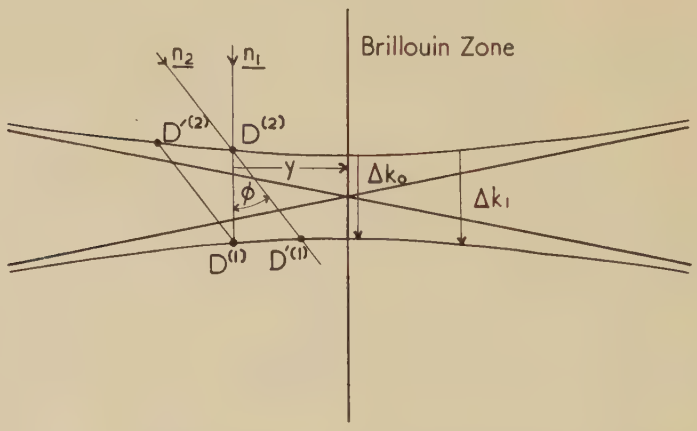

Near the symmetrical Laue case, for high energy electrons, the electron beam is almost perpendicular to the foil, and $\mathbf{n}_1$ is nearly parallel to the incident beam and the zone boundary. Hence $D^{(1)}D'^{(1)}D^{(2)}D'^{(2)}$ is practically a parallelogram. The plane containing $D^{(i)}$ and $D'^{(i)}$ makes an angle γ with the zone boundary in the general case, so that $D'^{(1)}$ and $D'^{(2)}$ do not lie in the plane of the paper.

The geometry of the dispersion surface leads to the following expression for Δk_1 in terms of x

$$\Delta k_1 = \Delta k_0 \sqrt{(1+x^2)}. \quad . \quad . \quad . \quad . \quad . \quad . \quad . \quad (19)$$

Then for $D^{(2)}$ and $D'^{(2)}$,

$$\Delta x = 2 \tan\theta \sqrt{(1+x^2)} \tan\phi \sin\gamma.$$

Putting $C^{(2)} = x + \sqrt{(1+x^2)}$ it is found that $\Delta C^{(2)}/C^{(2)} = 2 \tan\theta \tan\phi \sin\gamma$. In practice the Bragg angles are small ($\theta \sim 10^{-2}$ radians), therefore $\Delta C^{(2)}$ can be neglected provided the wedge angle ϕ is not too close to $\frac{1}{2}\pi$. Similar considerations hold for $C^{(1)}$ and the approximation is justified.

5.3. *Wave Functions at the Lower Crystal Surface*

It is possible by a procedure similar to that used at the entrance surface to find the wave points and amplitudes of the vacuum wave functions at the lower surface of the crystal. However, since the object of this paper is to predict theoretically the contrast effects expected on well focused transmission electron micrographs it is sufficient to evaluate the wave function $\Phi(\mathbf{r}_e)$ at points $\mathbf{r}_e$ on the lower surface of the crystal.

Putting $\Phi_0(\mathbf{r}_e)/\psi_I=\xi_0(\mathbf{r}_e)$ eqns. (18) give

$$\xi_0(\mathbf{r}_e)=\frac{C^{(1)}C^{(2)}}{(C^{(1)}-C^{(2)})^2}\Big[\exp\{\pi i(\mathbf{k_0}^{(1)}+\mathbf{k_0}^{(2)})\cdot\mathbf{r}_e\}\Big[\Big(\frac{C^{(1)}}{C^{(2)}}-1\Big)$$
$$\times\exp\{\pi i(\mathbf{k_0}^{(2)}-\mathbf{k_0}^{(1)})\cdot\mathbf{r}_e\}+\Big(\frac{C^{(2)}}{C^{(1)}}-1\Big)\exp\{-\pi i(\mathbf{k_0}^{(2)}-\mathbf{k_0}^{(1)})\cdot\mathbf{r}_e\}\Big]$$
$$+2\exp\{\pi i(\mathbf{k_0}^{(1)}+\mathbf{k_0}^{(2)})\cdot\mathbf{r}_e\}[1-\exp(-i\alpha)]\cos\pi(\mathbf{k_0}^{(2)}-\mathbf{k_0}^{(1)})\cdot\mathbf{r}_e$$
$$-2\exp\{\pi i(\mathbf{k_0}'^{(1)}+\mathbf{k_0}'^{(2)})\cdot\mathbf{r}_e\}[1-\exp\{-i\alpha\}]$$
$$\cos\pi(\mathbf{k_0}'^{(2)}-\mathbf{k_0}'^{(1)})\cdot\mathbf{r}_e\Big]. \quad . \quad . \quad (20)$$

In practice, for high energy electrons incident almost normal to the crystal, the geometry of the dispersion surface is such that $D^{(1)}D'^{(1)}D^{(2)}D'^{(2)}$ is practically a parallelogram (fig. 6). Hence $\mathbf{k_0}^{(1)}-\mathbf{k_0}'^{(1)}\simeq\mathbf{k_0}'^{(2)}-\mathbf{k_0}^{(2)}$ and therefore $\mathbf{k_0}^{(1)}+\mathbf{k_0}^{(2)}\simeq\mathbf{k_0}'^{(1)}+\mathbf{k_0}'^{(2)}$. Furthermore,

$$\pi(\mathbf{k_0}^{(2)}-\mathbf{k_0}^{(1)})\cdot\mathbf{r}_e=\pi\Delta k_1 t$$

where $\Delta\mathbf{k}_1=\mathbf{k_0}^{(2)}-\mathbf{k_0}^{(1)}=\overrightarrow{D^{(2)}D^{(1)}}$, t=thickness of the crystal, and

$$\pi(\mathbf{k_0}'^{(2)}-\mathbf{k_0}'^{(1)})\cdot\mathbf{r}_e=\pi(\overrightarrow{D^{(2)}D^{(1)}}+2\overrightarrow{D'^{(2)}D^{(2)}})\cdot\mathbf{r}_e=\pi\Delta k_1(t-2t'),$$

where t'=thickness of crystal 1 above the point $\mathbf{r}_e$.

Putting $\frac{1}{2}t-t'=z$ as in § 2, fig. 1, it is seen that

$$\pi(\mathbf{k_0}'^{(2)}-\mathbf{k_0}'^{(1)})\cdot\mathbf{r}_e=2\pi\Delta k_1 z.$$

Using the values of $C^{(i)}$ given in (10 *b*, *c*) eqn. (20) reduces to the sum of three terms

$$\xi_0(\mathbf{r}_e)=\phi_{01}+\phi_{02}+\phi_{03},$$

where

$$\phi_{01}=\cos\pi\Delta k_1 t-i\frac{x}{\sqrt{(1+x^2)}}\sin\pi\Delta k_1 t \quad . \quad . \quad . \quad . \quad (21\,a)$$

$$\phi_{02}=\frac{-1}{(1+x^2)}(\sin\tfrac{1}{2}\alpha+i\cos\tfrac{1}{2}\alpha)\sin\tfrac{1}{2}\alpha\cos\pi\Delta k_1 t \quad . \quad . \quad (21\,b)$$

$$\phi_{03}=\frac{1}{(1+x^2)}(\sin\tfrac{1}{2}\alpha+i\cos\tfrac{1}{2}\alpha)\sin\tfrac{1}{2}\alpha\cos 2\pi\Delta k_1 z. \quad . \quad (21\,c)$$

In these wave functions, which are the direct transmitted waves, the factor $\exp\{\pi i(\mathbf{k}_0^{(1)}+\mathbf{k}_0^{(2)})\cdot\mathbf{r}_e\}$ has been omitted. This does not affect the intensity distribution.

The wave functions corresponding to the diffracted beams $\phi_g^{(i)}$ and $\phi_g'^{(i)}$ may be derived in a similar way. We find that

$$\xi_g(\mathbf{r}_e)=\Phi_g(\mathbf{r}_e)/\psi_I=\phi_{g1}+\phi_{g2}+\phi_{g3}$$

where, apart from the phase factor

$$\exp\{\pi i(\mathbf{k}_g^{(1)}+\mathbf{k}_g^{(2)})\cdot\mathbf{r}_e\},$$

which has been omitted throughout,

$$\phi_{g1}=\frac{i}{\sqrt{(1+x^2)}}\sin\pi\Delta k_1 t \quad . \quad . \quad . \quad . \quad . \quad (22\,a)$$

$$\phi_{g2}=\frac{-i\exp\{i\tfrac{1}{2}\alpha\}\sin\tfrac{1}{2}\alpha}{(1+x^2)}[x\cos\pi\Delta k_1 t-i\sqrt{(1+x^2)}\sin\pi\Delta k_1 t] \quad (22\,b)$$

$$\phi_{g3}=\frac{i\exp\{i\tfrac{1}{2}\alpha\}\sin\tfrac{1}{2}\alpha}{(1+x^2)}[x\cos 2\pi\Delta k_1 z+i\sqrt{(1+x^2)}\sin 2\pi\Delta k_1 z]. \quad (22\,c)$$

It can be verified that the relation $|\xi_0|^2+|\xi_g|^2=1$ is satisfied in agreement with the general principle of conservation of electron intensity in the Fraunhofer pattern, assuming no absorption.

5.4. *Reflecting Sphere Construction*

It is convenient for the interpretation of electron diffraction photographs to consider the dynamical wave vectors of fig. 5 from the point of view of the reciprocal lattice and reflecting sphere construction. Figure 7 shows how this is obtained. The upper part of the figure shows the dispersion surface construction for determining the wave points $D^{(i)}$ and $D'^{(i)}$. $\overrightarrow{EO}$ represents the incident wave vector $\boldsymbol{\chi}$. $\overrightarrow{LG}$, $\overrightarrow{MG}$ and $\overrightarrow{JG}$ represent the directions of the three diffracted waves in the vacuum region below the crystal. Each diffracted wave vector is then transferred parallel to itself so that its origin coincides with E; their extremities then lie on the reflecting sphere of radius $\boldsymbol{\chi}$, centre E, passing through O but not through G. The following displacements at G occur.

$$\overrightarrow{GA}_1=\overrightarrow{LE}, \qquad \overrightarrow{GA}_2=\overrightarrow{ME}, \qquad \overrightarrow{GA}_3=\overrightarrow{JE}.$$

As E moves along $S_0{}^k$, i.e. as the inclination of the incident beam is varied, A_1, A_2, A_3 move along three curves near G. It is easily seen that the locus of A_1 is a line through G parallel to $\mathbf{n}_1$. The locus of A_3 may be obtained by considering the locus of $\overrightarrow{JE}$.

We have

$$\overrightarrow{JE}=\overrightarrow{JS}+\overrightarrow{SR}+\overrightarrow{RE}=\overrightarrow{PQ}+\overrightarrow{SR}.$$

Fig. 7

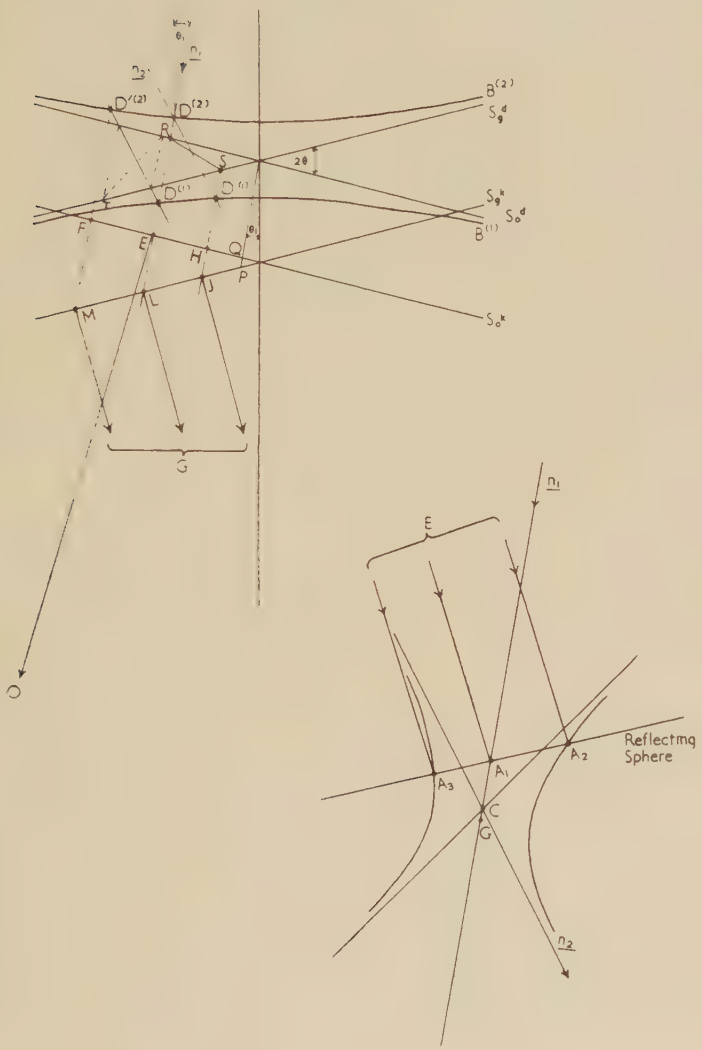

The dynamical construction on the dispersion surface in the upper half of the figure may be transferred to the reflecting sphere construction shown in the lower half (see text). The amplitude function in reciprocal space around G in the kinematical region, $|x| \gg 1$, is then effectively limited to spikes along the directions $\mathbf{n}_1$ and $\mathbf{n}_2$, i.e. normal to the entrance surface and faulting plane respectively.

It may be shown from the geometry of dispersion surface that $\overrightarrow{SR}$ describes one branch of a hyperbolic curve. The asymptotes of this hyperbola are the diagonals of the quadrilateral formed by ${S_0}^d$, ${S_g}^d$ and the dotted lines parallel to $\mathbf{n}_1$ in fig. 7. One asymptote is therefore parallel to the normal $\mathbf{n}_2$ to the stacking fault. Similar considerations show that the locus of A_2 is derived similarly from the other branch of the hyperbola. Furthermore the centre of this hyperbola near G is displaced from G by the vector $\overrightarrow{GC}$, where $\overrightarrow{GC}=\overrightarrow{PQ}$. However in the symmetrical Laue case, which is the case of interest here, $\mathbf{n}_1$ is parallel to the zone boundary so that $PQ=0$, and the effect is unimportant. In this case also the inclination of both asymptotes to the direction $\mathbf{n}_1$ is then equal to the wedge angle ϕ of fig. 6.

From the reflecting sphere construction therefore it is seen that the dynamical theory limits the interference function near G to the loci of the three points A_1, A_2, A_3.

The amplitude associated with the three points is obtained directly from eqns. (22). The amplitude at A_1 is $(\phi_{g1}+\phi_{g2})$, while that at A_2 and A_3 is obtained by writing ϕ_{g3} in terms of the two interfering plane waves. We then obtain the following expressions for the amplitudes at A_1, A_2, and A_3.

$$A_1: \quad \frac{i \sin \pi \Delta k_1 t}{\sqrt{(1+x^2)}} - \frac{i \exp\{i\tfrac{1}{2}\alpha\} \sin \tfrac{1}{2}\alpha}{(1+x^2)} [x \cos \pi \Delta k_1 t - i\sqrt{(1+x^2)} \sin \pi \Delta k_1 t] \quad . \quad . \quad . \quad . \quad . \quad . \quad (23\,a)$$

$$A_2: \quad \frac{i \exp(i\tfrac{1}{2}\alpha) \sin \tfrac{1}{2}\alpha}{2(1+x^2)} (x+\sqrt{(1+x^2)}). \quad . \quad . \quad . \quad . \quad . \quad . \quad . \quad . \quad . \quad (23\,b)$$

$$A_3: \quad \frac{i \exp\{i\tfrac{1}{2}\alpha\} \sin \tfrac{1}{2}\alpha}{2(1+x^2)} (x-\sqrt{(1+x^2)}). \quad . \quad . \quad . \quad . \quad . \quad . \quad . \quad . \quad . \quad (23\,c)$$

The first term in (23 *a*) is the amplitude function for an unfaulted crystal. This gives rise to a spike in reciprocal space perpendicular to the crystal surface. The second term in (*a*) is a modification due to the stacking fault. Examination of (23 *b*) and (*c*) shows that the amplitude function is larger near the n_2 asymptote than near the other asymptote, except near $x=0$, when all three diffracted waves may be of comparable magnitude. Hence in the kinematical region, i.e. when $x \gg 1$, (23 *b*) and (*c*), effectively reduce to a single spike in reciprocal space normal to the faulting plane.

A similar construction for the three directly transmitted waves may be performed at the point O.

§ 6. Discussion

6.1. *General*

Equations (21) representing the direct wave, together with eqns. (22) representing the diffracted wave, give the wave functions Φ_0 and Φ_g

at the lower crystal surface as the sum of three terms, the physical significance of which will now be examined.

ϕ_{01} is the wave function obtained if the stacking fault is removed, and represents the total transmitted wave function in the region where the crystals do not overlap.

At $x=0$, i.e. at the Bragg angle,

$$|\phi_{01}|^2=\cos^2\pi(t/t_0)$$

where $t_0=(\Delta k_0)^{-1}$ and $|\phi_{g1}|^2=\sin^2\pi(t/t_0)$. It is seen that the direct and diffracted beams oscillate in depth in antiphase between zero and unit intensity with a depth periodicity of t_0. This characteristic interchange of intensity between the direct and diffracted beams is an example of the well known phenomenon of extinction. Away from the Bragg position the oscillations occur with a periodicity

$$t_0'=(\Delta k_1)^{-1}=\{\Delta k_0\sqrt{(1+x^2)}\}^{-1}$$

i.e. the extinction distance is reduced to $t_0'=t_0/\sqrt{(1+x^2)}$. Using eqn. (9 *c*) it is seen that

$$|\phi_{g1}|^2=\sin^2\{\pi(t/t_0)\sqrt{1+(t_0s)^2}\}/\{1+(t_0s)^2\},$$

a result which was assumed in discussing the transition between kinematical and dynamical theory in § 2.

The term ϕ_{02} is a modification of the term ϕ_{01} present only in the region of overlap, which appears as a result of the phase difference α due to the stacking fault.

ϕ_{03} is a term present only in the overlap region due to the phase factor α. It is responsible for the appearance of interference fringes on bright field electron micrographs, analogous to the thickness fringes of a wedge crystal. The fringes are contours of constant z (fig. 1), so that they run parallel to the line of intersection of the stacking fault with the crystal surface. It can be seen that the form of the expression ϕ_{03} as a function of z implies that the number of fringes seen in the overlap region depends only on the crystal thickness t and on the parameter x, and is independent of the wedge angle ϕ of fig. 1. The interference fringes can be regarded as arising directly from the three coherent vacuum waves on the lower side of the crystal with wave points FE and H in fig. 5. Physically the problem is therefore one of the interference of three coherent electron waves, which distinguishes it from the case of the wedge crystal where only two waves are involved (Kato 1952 a). It will be noticed that at $z=\frac{1}{2}t$ and $z=-\frac{1}{2}t$ the term ϕ_{03} cancels the term ϕ_{02}, so that the wave function inside the region of overlap joins continuousiy that outside. It also follows from the form of the eqns. (21) and (22) that for $\frac{1}{2}\alpha=\pi\mathbf{g}\cdot\mathbf{R}=n\pi$ a stacking fault has no effect on the reflection. The unaffected reflections depend on the shear $\mathbf{R}$ and can be used to deduce the latter.

6.2. *Intensities*

The wave function intensity derived from eqns. (21) is

$$|\xi_0|^2=\left[\cos\beta_1+\frac{\sin^2\frac{1}{2}\alpha}{(1+x^2)}(\cos\beta_2-\cos\beta_1)\right]^2$$
$$+\left[\frac{\sin\frac{1}{2}\alpha\cos\frac{1}{2}\alpha}{(1+x^2)}(\cos\beta_2-\cos\beta_1)-\frac{x}{\sqrt{(1+x^2)}}\sin\beta_1\right]^2 \quad . \quad (24)$$

where $\beta_1=\pi\Delta k_1 t=\pi t\sqrt{(1+x^2)}/t_0$; $\beta_2=2\pi\Delta k_1 z=2\pi z\sqrt{(1+x^2)}/t_0$.

(i) At the Bragg reflecting position, $x=0$, the expression (24) reduces to

$$|\xi_0|^2=\cos^2\tfrac{1}{2}\alpha\cos^2\pi t/t_0+\sin^2\tfrac{1}{2}\alpha\cos^2 2\pi z/t_0. \quad . \quad . \quad . \quad (25)$$

It is seen that the interference fringes are of the cosine squared type, the spacing being given by $\Delta z=\frac{1}{2}t_0$. In this case therefore the spacing is half that of the corresponding wedge fringes obtained if one half of the faulted crystal is removed, in agreement with the simple argument presented in § 2.

(ii) For small x, the fringe profile becomes complicated but the periodicity is still given by $\Delta z=t_0/\sqrt{(1+x^2)}$. These fringes will be discussed in detail for the case of a close packed lattice in the following paper.

(iii) At large deviations from the Bragg position ($x\gg 1$) an asymptotic expansion of (24) may be obtained

$$|\xi_0|^2=1-x^{-2}[\sin^2\tfrac{1}{2}\alpha+\sin^2(\pm\pi\Delta k_1 t-\tfrac{1}{2}\alpha)$$
$$+2\sin\tfrac{1}{2}\alpha\sin(\pm\pi\Delta k_1 t-\tfrac{1}{2}\alpha)\cos 2\pi\Delta k_1 z] \quad . \quad . \quad . \quad . \quad (26)$$

where the positive sign is taken for $x>0$ and the negative sign for $x<0$. Putting $x=t_0 s$, where $t_0=K\cos\theta/|U_g|$ it is seen that for large $|x|$

$$\pm\pi\Delta k_1 t\simeq\pi ts$$

where s is positive for positive x and negative for negative x. (26) then reduces to

$$|\xi_0|^2=1-|U_g|^2K^{-2}\cos^{-2}\theta s^{-2}[\sin^2\tfrac{1}{2}\alpha+\sin^2(\pi ts-\tfrac{1}{2}\alpha)$$
$$+2\sin\tfrac{1}{2}\alpha\sin(\pi ts-\tfrac{1}{2}\alpha)\cos 2\pi zs]. \quad . \quad . \quad . \quad . \quad . \quad (27)$$

The second term in (27) represents the intensity of the reflected beam on the kinematical theory, and is identical with the expression derived in § 2.

6.3. *Overlapping Stacking Faults*

The problem of a crystal containing two or more stacking faults on parallel crystal planes can also be treated on the dynamical theory by successive applications of eqns. (17) to the lamellar regions between

the faults. Figure 8 shows stacking faults on planes P_1 and P_2 separated by a distance $\delta\mathbf{n}_2$. In using eqns. (17) to determine the wave amplitudes in region 3, complications arise owing to wave propagation factors of the form

$$\exp\{2\pi i\mathbf{k}_g^{(i)}\cdot\delta\mathbf{n}_2\} \qquad \text{and} \qquad \exp\{2\pi i\mathbf{k}_g'^{(i)}\cdot\delta\mathbf{n}_2\}.$$

For the case of a single fault it was possible to avoid wave propagation factors in eqns. (17) by choosing a special origin at Q in fig. 1. For two or more faults it is not possible to choose an origin which renders the eqns. (17) equally simple at either fault. However for the case of two faults on closely spaced planes, the total vector shear is $\mathbf{R}=\mathbf{R}_1+\mathbf{R}_2$ where

Fig. 8

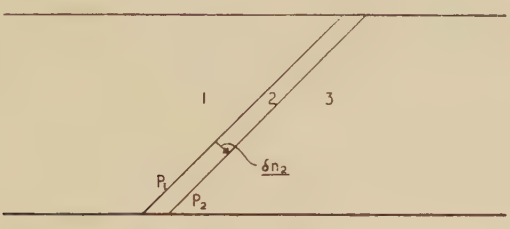

Crystal containing two stacking faults on planes P_1 and P_2.

$\mathbf{R}_1$ and $\mathbf{R}_2$ are the shears at each fault. If this shear is imagined to occur on one plane, the phase factor of the resultant fault is simply the sum of the phase factors of the two separate faults. It is therefore clear that the case of overlapping faults on neighbouring atomic planes can be treated by applying the theory for a single fault, using a phase factor which is the sum of phase factors of the individual faults. The approximation is valid for the case of stacking faults on neighbouring atomic planes, when factors of the form $\exp\{2\pi i\Delta\mathbf{k}_1\cdot\delta\mathbf{n}_2\}\sim 1$. The application of this result to the case of overlapping faults in close packed lattices will be considered in the following paper.

Acknowledgments

The authors wish to express their thanks to Professor N. F. Mott, F.R.S., Dr. W. H. Taylor and Dr. V. E. Cosslett for encouragement and helpful discussion during the course of this work. One of us (M. J. W.) acknowledges the receipt of a maintenance grant from the Department of Scientific and Industrial Research.

References

Bethe, H. A., 1928, *Ann. Phys., Lpz.*, **87**, 55.

Bollmann, W., 1957, *Proceedings of the Stockholm Conference on Electron Miscroscopy* (Stockholm : Almquist and Wiksell), p. 316.

Dowell, W. C. T., Farrant, J. L., and Rees, A. L. G., 1956, *Proceedings of the International Conference on Electron Microscopy* (London), p. 279 ; 1957, *Proceedings of the regional Conference on Electron Microscopy* (Tokyo), in the press.

Gard, J. A., 1956, *International Union of Crystallography*, Symposium (Madrid).
Hashimoto, H., and Uyeda, R., 1957, *Acta Cryst.*, **10**, 143.
Heidenreich, R. D., 1949, *J. appl. Phys.*, **20**, 993.
Hillier, J., 1954, *National Bureau of Standards Circular*, No. 527, ' Electron Physics Colloquia ', p. 413.
Hirsch, P. B., Horne, R. W., and Whelan, M. J., 1956, *Phil. Mag.*, **1**, 677.
Kato, N., 1952 a, *J. phys. Soc. Japan*, **7**, 397 ; 1952 b, *Ibid.*, **7**, 406 ; 1953, *Ibid.*, **8**, 350.
MacGillavry, C. H., 1940, *Physica*, **7**, 329.
Mitsuishi, T., Nagasaki, H., and Uyeda, R., 1951, *Proc. Jap. Acad.*, **27**, 86.
Pashley, D. W., Menter, J. W., and Bassett, G. A., 1957, *Nature, Lond.*, **179**, 752.
Seki, Y., 1953, *J. phys. Soc. Japan*, **8**, 149.
Thomson, G. P., and Cochrane, W., 1939, *Theory and Practice of Electron Diffraction* (Macmillan), p. 283.
Whelan, M. J., Hirsch, P. B., Horne, R. W., and Bollmann, W., 1957, *Proc. roy. Soc.* A, **240**, 524.

Polarization of μ-Mesons Observed in a Propane Bubble Chamber†

By Margaret H. Alston, W. H. Evans, T. D. N. Morgan,
R. W. Newport and P. R. Williams
Nuclear Physics Research Laboratory, University of Liverpool

and A. Kirk
Applied Mathematics Department, University of Liverpool

[Received June 21, 1957]

Abstract

3734 π^+–μ^+–e^+ decays have been observed in a propane bubble chamber and the angular distribution of the positions found to be

$$(dN/d\Omega) \propto 1-(0{\cdot}16\pm 0{\cdot}04)\cos\theta.$$

The decay and absorption of μ^--mesons in propane have also been investigated.

The angular distribution of positrons resulting from π^+–μ^+–e^+ decays at rest is now known to be asymmetric and of the form $(1+\alpha\cos\theta)$ (Garwin *et al.* 1957, Cassels *et al.* 1957, Bhownik *et al.* 1957, Biswas *et al.* 1957, Castagnoli *et al.* 1957, Chadwick *et al.* 1957, Freedman and Telegdi 1957, Abashian *et al.* 1957); where θ is the angle between the muon spin direction and the positron momentum. The coefficient α depends upon the polarization of the muon and the momentum of the positron (Lee and Yang 1957). The value of α, for the whole positron spectrum, has been measured in propane at 62°C and 200 p.s.i. using a bubble chamber.

π^+-mesons from the Liverpool, 156 in. synchrocyclotron were stopped in the propane bubble chamber previously described (Alston *et al.* 1957). The stray magnetic field in the chamber was reduced to less than 0·25 gauss. Two plane projections, at 90° to each other, were photographed and then back projected onto a translucent screen for analysis. Measurements were made on the two projections separately of the μ-meson range and the angles of both the initial μ-meson direction and the initial positron direction relative to the line of intersection of the two projection planes (reference axis). The true angles between the muon and reference axis and the muon and positron were computed using the Manchester University MK II Electronic computor.

3734 π^+–μ^+–e^+ decays were measured. The angular distribution of the positron with respect to the initial direction of the muon is shown in fig. 1 and the angular distribution of the μ^+-mesons about the reference axis in

---

† Communicated by Professor H. W. B. Skinner.

fig. 2. The μ^+-meson distribution should be isotropic since the π-meson decays at rest† ; fig. 2 shows that there is some scanning bias in the forward and backward directions. This is caused by the shortness of the muon

Fig. 1

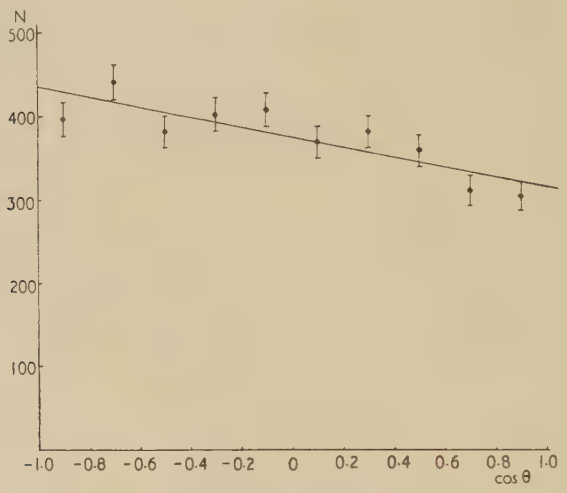

Positron distribution.

Fig. 2

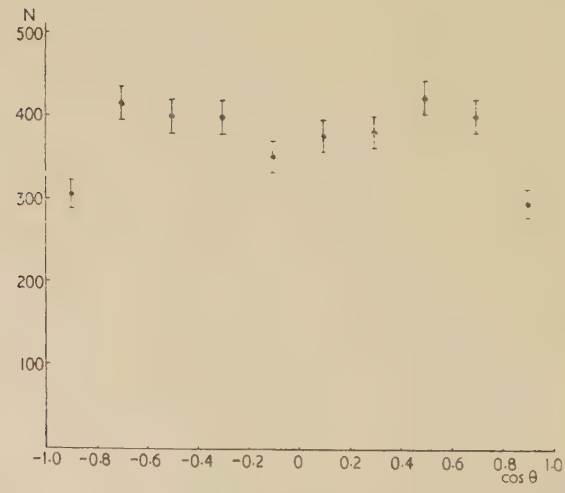

Muon distribution.

track (~3·2 mm) and the similarity between its ionization and that of the pion which makes it difficult to distinguish a π^+–μ^+ decay with certainty at these angles. This bias does not exist in the μ^+–e^+ case where the

† *Note added in proof.*—The angular distribution of muons has been the subject of recent dicussions. Our results do not support the existence of an appreciable cos θ term.

ionization of the muon and positron are very different. A least squares fit to the positron distribution of the form $(1+\alpha\cos\theta)$ gives $\alpha=-0{\cdot}16\pm0{\cdot}04$ and the probability of the experimental distribution arising from an isotropic distribution is $<10^{-4}$. The value of α obtained from the forward-backward ratio is $-0{\cdot}17\pm0{\cdot}03$. The range of the μ-mesons was also calculated from the measurements and the density of propane at the operating conditions of 62°c and 200 p.s.i. was found to be 0·43 g/cm³.

The value of α found is less than that obtained by Garwin (Garwin *et al.* 1957) and Cassels (Cassels *et al.* 1957) for copper and carbon and shows that propane depolarizes the muons. It agrees with the value of $-(0{\cdot}18\pm0{\cdot}05)$ obtained in propane by the M.I.T., Chicago and Harvard Group (Pless 1957).

Another consequence of parity non-conservation in weak interactions (Lee 1957, Uberall 1957) is that neutrons emitted as a result of the capture of polarized μ^--mesons by protons should show an asymmetry about the muon spin direction, and the sign of the asymmetry depends upon the type of Fermi interaction involved. Since the absorption of muons in hydrogen is very infrequent it is more practicable to observe the absorption of muons in heavier nuclei. The distribution of one pronged stars, produced by the collision of an emitted neutron with a proton inside the nucleus, should also be asymmetric.

In a preliminary survey, the propane bubble chamber was exposed to the 95 MeV π^--meson beam with sufficient copper absorber inserted to stop μ^--mesons in the chamber. The resulting μ^-–e^- decays and μ^--absorption in the carbon of the propane (C_3H_8) were observed. The results are shown in the table. Some of the forward going particles of

Number of pictures 2500			Zero prong stars		107
μ^-–e^- decays, Forward	285		1 prong stars, Forward	9	
Backward	298	617	Backward	8	17
90°	34		2 prong star		1

Average energy of 1 prong stars=15 MeV.

the one pronged stars could be due to the scattering of the muon in the last few millimetres of its range followed by a zero prong star. Measurements on muon scatterings near the end of their ranges give an estimate of 4 such events. Unfortunately the results are inconclusive because of the poor statistics. For 100% polarized muons the neutron distribution should be $(1-\cos\theta)$ for S and V and $(1+\frac{1}{3}\cos\theta)$ for A and T couplings. Since in our case the final muon polarization in propane is not expected to be much greater than 10% (Holt, private communication) about 1000 stars would be required to distinguish between the two possible couplings. The experiment has been abandoned since the absorption of muons in much heavier nuclei, where the absorption rate is higher, and the direct measurement of the emitted neutrons seems a more feasible method of obtaining sufficient data.

Acknowledgments

The authors would like to thank Professor H. W. B. Skinner for his interest and Professor J. M. Cassels for suggesting the second experiment and for many helpful discussions during both experiments. We also thank Mr. B. Halliday and the cyclotron crew for their cooperation during the cyclotron run and Mr. R. A. Brooker of the Manchester University Computing Laboratory allowing us use of the computor. R. W. N. and T. D. N. M. wish to thank D. S. I. R. and Liverpool University, respectively, for maintenance grants.

References

Abashian, A., Adair, R. K., Cool, R., Erwin, A., Kopp, J., Leipuner, L., Morris, T. W., Rahm, D. C., Rau, R. R., Thorndike, A. M., Wittemore, W. L., and Willis, W. J., 1957, *Phys. Rev.*, **105,** 1927.

Alston, M. H., Collinge, B., Evans, W. H., Newport, R. W., Williams, P. R., 1957, *Phil. Mag.*, **2,** 820.

Bhownik, B., Evans D., and Prowse, D. J., 1957 (in the press).

Biswas, N. N., Ceccarelli, M., and Crussard, J., 1957, *Nuovo Cim.* **5,** 756.

Cassels, J. M., O'Keeffe, T. W., Rigby, M., Wetherell, A. M., and Wormald, J. R., 1957, *Proc. phys. Soc. Lond.* A, **70,** 543.

Castagnoli, C., Franzinetti, C., and Manfredini, A., *Nuovo Cim.*, 1957, **5,** 684.

Chadwick, G. B., Durrani, S. A., Eisberg, L. M., Jones, P. B., Wignall, J. W. G., and Wilkinson, D. H., 1957, *Phil. Mag.*, **2,** 684.

Freedman, J. I., and Telegdi, V. L., 1957, *Phys. Rev.*, **105,** 1681.

Garwin, R. L., Lederman, L. M., and Weinrich, M., 1957, *Phys. Rev.*, **105,** 1415.

Lee, T. D., and Yang, S. N., 1957, *Phys. Rev.*, **105,** 1671.

Lee, T. D., *Rochester Conference,* April, 1957.

Pless, I. A., *Rochester Conference,* April, 1957.

Uberall, H., 1957 (to be published).

A Proposal for Determining the Fermi Surface by Magneto-Acoustic Resonance†

By A. B. Pippard
Royal Society Mond Laboratory, Cambridge

[Received July 13, 1957]

§ 1. Introduction

It has been observed by Bömmel (1955) that the attenuation of ultrasonic waves in a pure tin crystal at 4°K is affected by a transverse magnetic field in a manner which is periodic with the field strength. The probable origin of the effect may be understood by considering a free-electron model of a metal, carrying transverse ultrasonic waves of wavelength short compared with the electronic free path. Associated with the particle velocity of the wave is an electric field (Pippard 1955) as shown in the figure. If we remember that the velocity of sound is usually several hundred times less than the electronic velocity at the Fermi surface we may conveniently imagine the field distribution to be effectively stationary in space ; it is now possible to adjust the diameter of an electronic orbit so that it equals one half-wavelength, and can continuously extract energy from the ultrasonic field. Under these conditions we may expect an enhanced attenuation, but clearly the effect demands a free path at least as long as the perimeter of the orbit. If a very long path can be achieved, subsidiary attenuation peaks should be observed at lower field strengths, when the orbit diameter is an odd multiple of half-wavelengths, so that the attenuation should be a regular periodic function of $1/H$, just like the de Haas-van Alphen effect. So too, as in the latter effect (Onsager 1952) the periodicity is determined by the electrons in the neighbourhood of any extremal areas of the Fermi surface when intersected by a plane normal to H. To see if the proposed explanation gives the correct order of magnitude for the field strengths required let us assume for tin a spherical Fermi surface containing one electron per atom; then at 10·3 Mc/s, the frequency of Bömmel's experiment, the principal resonance (one half-wavelength) should occur in a field of 800 gauss. In fact it probably lies between 300 and 400 gauss. This is not unsatisfactory, in view of the crude assumption of a free-electron gas, and lends confirmation to the idea that we have here a new type of cyclotron resonance. It is interesting to note that the resonance concerns the spacial extension of the electron orbits, and has nothing to do with the frequency with which the orbits are traversed.

If the Fermi surface is not spherical the electron orbits will not be circular helices, but of a more complex form depending on the shape of the

† Communicated by the Author.

Fermi surface, perhaps as sketched in the figure. But the periodicity of the attenuation in $1/H$ will still be determined by the electrons around an extremal cross section, and from the figure it appears that the resonance condition is governed by the total extension Z of the orbit in the direction of wave propagation, i.e. for a maximum of attenuation $Z=(n+\frac{1}{2})\lambda$ (in the figure the resonance with $n=0$ is shown). The particular extremal cross section determining resonance will be that of stationary Z, rather than of stationary area as in the de Haas–van Alphen effect. Now the cross section of the Fermi surface in p-space responsible for a given orbit in real space has the same shape as the orbit but is scaled by a factor eH/c and rotated through a right-angle (Onsager 1952). Thus if the overall dimension of the Fermi surface, in a direction normal both to H and the wave-vector, is P, the resonance condition is that $cP/(eH)=(n+\frac{1}{2})\lambda$, so that the periodicity in $1/H$,

$$\Delta(1/H)=e\lambda/(cP).$$

Clearly then a study of single crystals in all orientations can give a great deal of detailed information about the shape of the Fermi surface.

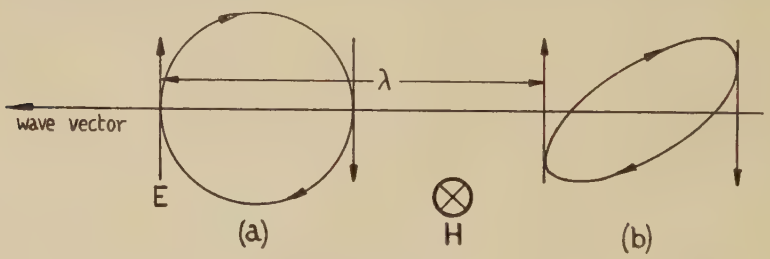

Field distribution for observing magneto-acoustic resonance.
(*a*) orbit for free electron ;
(*b*) schematic orbit for non-spherical Fermi surface.

These intuitive ideas need refinement, particularly as regards the details of the resonance condition for non-spherical Fermi surfaces, but the method looks promising enough in principle. It should be pointed out that Bömmel's measurements were made with longitudinal, not transverse, waves. In an elastically isotropic medium no effect should be observed, but real metals are far from isotropic and in general one may expect transverse fields associated with nominally longitudinal waves, except for propagation along certain symmetry axes. Finally, we may remark that the function of the ultrasonic wave is simply to set up a rotational electric field and to act as a resonance detector. It is possible that quite other means might be devised to achieve the same end.

References

Bömmel, H. E., 1955, *Phys. Rev.*, **100**, 758.
Onsager, L., 1952, *Phil. Mag.*, **43**, 1006.
Pippard, A. B., 1955, *Phil. Mag.*, **46**, 1104.

The Nature and Formation of the Photographic Latent Image†

By J. W. Mitchell
H. H. Wills Physical Laboratory, Royal Fort, Bristol, 8

and N. F. Mott
Cavendish Laboratory, Cambridge

[Received June 24, 1957]

Summary

A review is given of a theory of the nature and mode of formation of the photographic latent image and of the experimental evidence on which the theory is based. Earlier hypotheses due to Eggert and to Gurney and Mott are used, according to which the primary action of the light is to free photoelectrons and positive holes and the formation of silver specks involves the movement of silver ions. The stable latent image is seen as a positively charged silver speck on the surface of a halide grain, or in the case of internal image at a dislocation. The minimum stable image is a positively charged group of four silver atoms (Ag_4^+), the formation of which requires three electrons. The sub-image is a neutral pair of silver atoms and requires two electrons for its formation. A main role of silver sulphide is to provide traps for positive holes; after doing so the sulphide molecule dissociates into AgS and an interstitial cation. In terms of this model a discussion is given of reciprocity failure, development, the role of iodide and of other phenomena.

§ 1. Introduction

In 1938 the late Dr. Gurney and one of the present authors published a theory of the processes leading to the formation of the photographic latent image (Gurney and Mott 1938). Since then much experimental and theoretical work has been done on this subject (see Mitchell 1957 a, b, e for a review) and there has also been a very considerable development in the concepts of the physics and chemistry of the solid state on which this work was based. The purpose of the present paper is to review the state of the theory in the light of all these advances in our knowledge, and to give an outline of the movements of ions and electrons which now appear to us as the most likely to occur during latent image formation.

The original theory can be summarized as follows. On the basis of the work of Pohl's school, silver bromide was known to be a photoconductor

† Communicated by the Authors.

at the temperature of liquid air, each quantum of light absorbed producing an electron and positive hole (halogen atom). At this temperature, the electrons were shown to be mobile and to be trapped easily by colloidal silver if present. This was assumed to be their normal fate also at room temperature in the presence of such silver ; in its absence they were thought to be trapped, in a sensitized silver bromide grain, by the ' sensitivity specks ' introduced into photographic thinking by Shepherd and identified with silver sulphide. The positive holes were assumed to have some mobility at room temperature (Mott 1948), though Pohl's work at low temperatures provided no evidence for this, and it was suggested that they would move at random till they reached the surface and that halogen would then escape. The primary result of exposure of an emulsion to light or to ionizing radiation would thus be to transfer a negative charge to the silver or sensitivity specks. This would then be neutralized by the movement to the speck of interstitial silver ions. In this way a particle of silver would grow.

All the evidence now available to us suggests the correctness of the principle that both electrons and silver ions move over considerable distances in silver halide grains under illumination. Although prior to 1938 it was generally assumed that the liberation and displacement of electrons occurred during the formation of the latent image, the only reference to motion of silver ions published before then is due to Eggert (1926), who recognized that silver atoms were formed by the combination of silver ions and electrons on nuclei of metallic silver. The paper by Gurney and Mott was the first to introduce interstitial silver ions into the mechanism of the photochemical reaction and to recognize that the displacement of electrons would create a potential difference which would cause these ions to drift.

Some evidence that illumination produces mobile electrons both in normal and dye-sensitized emulsions is summarized in § 2. Although there is little clear evidence for the motion of holes, escape of halogen would scarcely be possible if they could not move. As regards the mechanism of their production, we shall in § 3 give a more detailed description than was possible in 1938 of how this occurs.

Apart from the general principle of the motion of ions and electrons, we believe that for the printing out process, that is to say, for the photochemical formation of silver once metallic particles containing many atoms have been formed, the model presented by Gurney and Mott is not far from the truth. One major modification is introduced ; silver in contact with silver halide carries a positive charge, so that we may regard this as attracting the photoelectrons rather than a negatively charged speck attracting the interstitial cations. This point is of importance ; positive holes cannot reach positively charged silver specks in equilibrium with silver halide, and this is the reason why stable centres do not act as centres of recombination of electrons and holes, as surface traps and dislocations do in germanium.

The theory of latent image formation which has been proposed by one of the present authors (Mitchell 1957 a, b, e) and is reviewed here, however, differs considerably from that of Gurney and Mott. There is no evidence that stable *electron* traps play any role in photographic sensitivity at room temperature, and some to the contrary. We believe that the first step in setting up the latent image is the formation of what we shall call a pre-image speck, the combination of a silver ion adsorbed on the surface, probably near a kink site, with an electron. The pre-image speck is very unstable, having a life time of from 10^{-5} to 1 second, so that latent image formation is not possible, unless

(*a*) the positive hole is firmly trapped ;

(*b*) some movement of ions or atoms occurs (such as escape of halogen) which prevents the electron from recombining with it.

We emphasize that (*b*) is necessary as well as (*a*) for *latent* image formation, because at this stage there are no electron traps and the formation of the latent image is a slow process involving two or more electrons. We shall suggest that a kink site occupied by a bromide ion provides only a shallow trap for a positive hole, and the process by which halogen molecules (Br_2) are formed and escape involves *two* holes and has low probability. Adsorbed Ag_2S, on the other hand, provides deep traps for holes, and, by the escape of an interstitial silver ion from Ag_2S^+ to form AgS, makes recombination with an electron impossible except when an interstitial ion is in the neighbourhood. This we believe to be the main role of sulphur sensitization.

The steps in the formation of the latent image are then :

(i) The formation of the ' pre-image speck ', as already stated, i.e. a silver ' atom ' probably adsorbed at a kink site terminated by a silver ion. This involves the cooperation of one electron and one interstitial ion. The pre-image speck has a lifetime of 1 to 10^{-5} sec. The lifetime of an electron trapped at a kink site without the cooperation of an additional silver ion must be negligibly small, say 10^{-8} sec.

(ii) The formation of the ' sub-image ', a neutral complex Ag_2 adsorbed at a kink site. This involves the utilization of a second photoelectron and a second interstitial silver ion. The sub-image has a lifetime of days and can be developed.

(iii) The formation of the stable latent image. This utilizes a further electron and two interstitial silver ions, and gives in equilibrium a positively charged group of *four* silver atoms Ag_4^+.

From this point onwards any further growth of the silver speck will occur as described above by the Gurney–Mott mechanism.

§ 2. Evidence for the Gurney–Mott Principle

In this section we review some of the evidence that the primary action of the light is to produce photoelectrons, and that the photoelectrons produced allow the formation of aggregations of silver atoms, i.e. of photolytic silver.

Observations of photoconductivity of silver halides at room temperature were first made by Arrhenius (1887) and detailed work was done by Toy and Harrison (1930). The work of Pohl's school before 1939 (see for example Mott and Gurney 1948) showed that silver bromide at low temperatures is a photoconductor, giving something near quantum equivalence (one electron per photon absorbed) ; this work need not be reviewed here. Recent work that we may mention is the confirmation by West and Carroll (1947) that the long-wave limits for photoconductivity, optical absorption and photographic sensitivity are the same (4900 Å for silver bromide), and West's (1951) work on photoconductivity in emulsions, which shows that with or without either chemical or optical (dye) sensitization the formation of the latent image is accompanied by photoconductivity.

Strong evidence for the validity of the Gurney–Mott principle (see Mitchell 1957 b) comes from experiments which show the ability of an electric field to displace print-out silver or the developable latent image away from the point of illumination. Of these the first were due to Haynes and Shockley (1948, 1951). By observations of the formation of photolytic silver, these authors showed that electrons, liberated in crystals of silver chloride by light flashes of short duration, could be displaced through at least 1·5 cm by the application of synchronized pulsed electric fields. Webb (1955) has since observed a similar displacement of photolytic silver in large crystals in emulsions by synchronized pulsed fields. The first observations of the displacement of a developable latent image were made by Hedges and Mitchell (1953 b) and Evans, Hedges and Mitchell (1955) in large thin single crystals of fused silver bromide. Since then, Hamilton *et al.* (1956) have observed the displacement of the latent image in microcrystals in photographic emulsions.

The conclusion to be drawn from all these observations is that the formation of the latent image and of photolytic silver at room temperature involves the participation of mobile electrons separated from the corresponding positive charge. Hamilton *et al.* have also observed phenomena which must be attributed to the displacement of positive holes by electric fields (see also Luckey and West 1956). We shall therefore base our discussion of the formation of the latent image upon the assumption that independently mobile electrons and positive holes are liberated by the absorption of energy in crystals of silver halides at room temperatures.

Nevertheless, in the absence of an applied field there is no formation of surface latent image outside the illuminated areas of either chemically sensitized large single crystals (Evans, Hedges and Mitchell 1955) or large microcrystals (Mitchell 1957 a). Internal latent image is formed outside the illuminated areas and up to depths of at least 40 μ below the surfaces of large crystals (Clark and Mitchell 1956, West and Saunders 1957). The absence of surface image outside the illuminated area is probably because most of the light is absorbed within a micron of the

surface, and further, as we shall show, it takes at least three electrons to form a latent image. The chance of forming an image will therefore fall off as a high power of the density of electrons, and will thus occur mainly in the region where much light is absorbed, unless a strong field is applied to the crystal.

Early evidence for the occurrence of some two-stage process was provided by the work of Berg and others on illumination at low temperatures (see Mott and Gurney 1948), suggesting that electron movement could occur under these conditions and subsequent ionic movement on warming up. However, in view of more recent work by Farnell (1952) and by Biltz (1952) there is some uncertainty in the detailed interpretation of this work, which will not be discussed further here.

§ 3. Mobilities and Properties of Ions

All work on photochemical processes in silver halides is based on the assumption that they contain Frenkel defects, that is interstitial silver ions and an equal number of vacant cation sites, the association in equilibrium being negligible. A recent review of the evidence for this, together with the activation energies involved, has been given by Ebert and Teltow (1956, see also Mitchell 1955, 1957 e).

Some useful figures are for silver bromide :

Number of Frenkel defects per cm^3 at room temperature	10^{12}
Number of jumps per sec for an interstitial ion	4×10^{10}
Activation energy for movement of interstitial ion (ev)	0·11.

It is important for our purpose, also, to consider the surface mobility both of silver ions and silver atoms adsorbed on a clean surface. Both are believed to be high. A review of the evidence together with some numerical values has been given by Shapiro and Kolthoff (1947), who deduced the following equation for the surface ionic conductivity of a powder

$$\sigma=\text{constant } S \exp(-W/kT)$$

where S is the surface per unit mass of the powder and $W=0{\cdot}36$ ev is an activation energy. W is thus the energy required to move a cation from a kink site to an adsorbed site, together with the activation energy for its movement over the surface. These values are not relevant to emulsions, however, on account of the influence of gelatine on the surface mobility.

Another important concept is that of a kink site (fig. 1). At a kink site may be either a cation or anion. Cations may pass from kink sites into solution at a halide–liquid interface, into an adsorbed position as Q, or into interstitial positions in the crystal. Jogs on dislocations have

properties very similar to kink sites, in that they can act as sources or sinks for interstitial ions.

We have already emphasized that massive silver is positively charged in contact with silver bromide. We shall be much concerned with the binding energies of silver ions to *small* aggregates Ag, Ag_2 and Ag_3, all adsorbed on a halide surface, and shall come to the conclusion that Ag_3 is the smallest aggregate where the binding is stable at room temperature (Mitchell 1956, 1957 a, b, e) and which therefore carries a positive charge as Ag_4^+.

Fig. 1

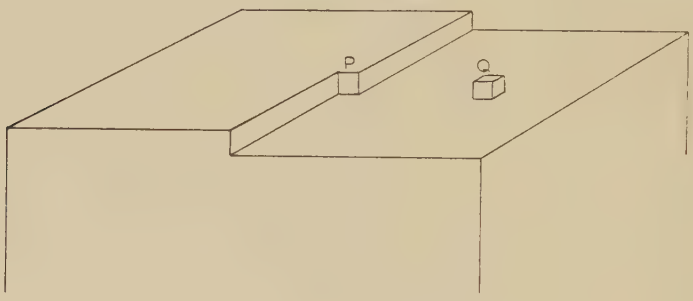

A kink site P, and an adsorbed atom Q.

§ 4. Energy Levels and Mobilities for Electrons in Silver Bromide

A level scheme of the conventional kind is given for silver bromide in fig. 2. Photoconductivity, optical absorption and photographic sensitivity agree in giving the width of the forbidden band as 2·5 ev (West and Carroll 1947). At low temperatures Okamoto (1956) obtains a displacement of the long wave limit of absorption to 2·7 ev. Taft and Apker's (1957) work on photo-emission gives the energy required to remove an electron from the top of the full band into vacuum as 6·0 ev, so the bottom of the conduction band has energy (in ev)

$$6{\cdot}0-2{\cdot}5=3{\cdot}5.$$

Since the work function of massive silver is 4·3 ev, it might be thought that the threshold for emission from massive silver into the conduction band would be about 0·8 ev. This, however, neglects the double layer at the interface, which will increase it, so that we cannot without knowing its magnitude predict the threshold for electron emission from silver into silver bromide.

The width of the valence band is shown by the breadth of the corresponding x-ray emission band (O'Bryan and Skinner 1940) to be about 3 ev.

We have also to ask whether ' excitons ' play any role ; it is a marked property of the absorption spectra of *alkali* halides that excitons† are

† For recent discussions of excitons in alkali halides, cf. Overhauser (1956).

formed for quantum energies *less* than AB in fig. 2 (compare Mott and Gurney 1948). Figure 3 shows a recent observation made in Göttingen of the absorption spectrum of silver bromide due to Okamoto (1956 ;

Fig. 2

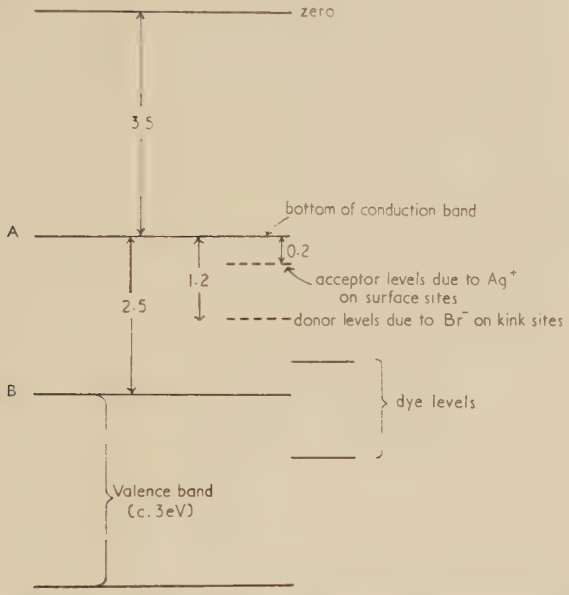

Level scheme based on experimental data for crystalline silver bromide. The zero is the energy of an electron at rest outside the crystal.

Fig. 3

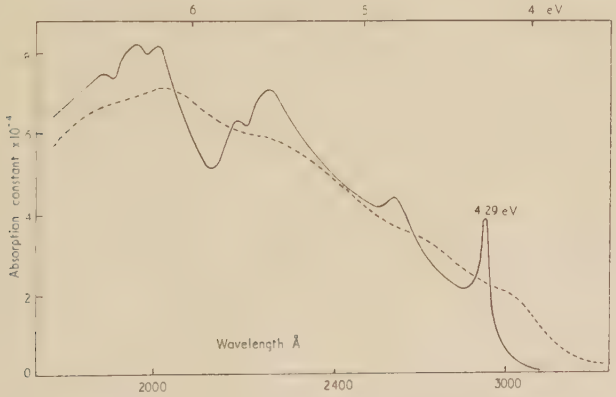

Absorption spectrum of silver bromide (after Okamoto).
– – – at room temperature (293°K).
——— at 20°K.

see also Tutihasi 1957). It will be seen that exciton lines, showing the doublet characteristic of the bromide atom, appear at low temperatures, though they are relatively weaker than for the alkali halides, as one

expects for a material with a higher dielectric constant. A difference between the silver and alkali halides is that, as far as one knows, photoconduction appears for all wavelengths for the former. It may be that, for the silver halides, forbidden transitions between a relatively broad valence band and the conduction band overlap the optically allowed exciton band.

This is more likely to be so for silver bromide than for potassium bromide, for example, because of the more covalent character of the binding ; in other words because the p-orbitals of Br$^-$ overlap the Ag$^+$ ions and hence overlap each other. Since under these conditions an exciton will rapidly dissociate, we may assume that the absorption of a quantum *always* produces a free electron and a free hole.

The long-wave limit of the absorption band will, if our hypothesis is correct, be due to forbidden transitions (i.e. those for which the wave vector **k** is not conserved), and which are possible only because of thermal agitation. The situation is similar to that which has been discussed in great detail for germanium (cf. Fan 1955).

Apart from the characteristic absorption, we need to consider the absorption due to atoms on certain special sites, notably *halide* ions at kink sites on the surface or at jogs in dislocations (the two are similar). These should produce normally occupied levels somewhat above the full band. No sign of their effect on the optical absorption or on the sensitivity has been observed, perhaps because of a low oscillator-strength for transitions from such levels to the conduction band ; they are, however, believed to play an essential role in dye-sensitization as follows :

The dye molecules are adsorbed to the surface of a grain, sometimes as a monolayer but the optimum quantum efficiency is obtained for a much lower concentration. With less than a monolayer we can expect preferential adsorption near kink sites. The levels will be as shown in fig. 2 ; after absorption of a quantum it is not possible for the dye to lose an electron to the conduction band, as originally suggested by Gurney and Mott. For monolayers the excitation may perhaps be passed from molecule to molecule ; whether this occurs is not known and such a process is not essential. What is essential is this : if an excited molecule is less than about 5×10^{-7} cm from a kink site, the excited molecule will hand over its energy to an electron there before itself falling to the ground state. The electron is then thrown into the conduction band. This role of the effect of dyes has already been proposed (Franck and Teller 1938, Mott 1948) ; it is similar to the phenomenon observed by Apker and Taft (1951), where energy absorbed in the exciton band of alkali halide crystals is transferred to F-centres, from which electrons are ejected out of the crystal.

Emulsions can be sensitized down to 13 000 Å (about 1 ev) but here the sensitivity may be temperature sensitive, and it would seem that thermal oscillations must help the dipole field from the excited dye molecule to throw an electron from the halide ion into the conduction

band. A reasonable assumption, then, is that some of these occupied levels are about 1·2 ev below the conduction band, as suggested in fig. 2.

An electron and hole having been formed, we have to ask what their mobilities may be, both as free particles, and as affected by traps. We consider first electrons. Here the most direct evidence is from the work of Haynes and Shockley (1948, 1951) already referred to. These authors used the print-out effect within large single crystals of silver chloride (at room temperature) to determine both the Hall mobility and the drift mobility of photo-electrons. Some of their results are :

Drift mobility	49·5 cm^2/volt sec
Hall mobility	51·3 cm^2/volt sec
Mean free path	33 Å
Time for one free path	3×10^{-14} sec
Number of lattice constants traversed before final trapping	2×10^9.

The last figure suggests that an electron which meets a dislocation in which silver particles have already separated is trapped, it being reasonable to suppose that one ion pair in 10^9 is on a dislocation.

The close equality between the drift and Hall mobilities shows clearly that trapping is *not* important until the electron arrives finally at the colloidal metal. One ion in 10^{14} is an interstitial ion : these ions at room temperature must, however, be very ineffective traps. Simpson (1955) calculates on theoretical grounds a value of about 0·1 ev for the trapping energy. If this is correct an electron would remain in such a trap at room temperature only for the time required for two or three mean free paths, so the effect would be negligible.

We are interested in other trapping centres, particularly those on the surface. For instance, we may consider kink sites occupied by a cation. The field round such a point is equivalent to that round *half* an electronic charge, so that, especially in the presence of gelatine which ensures a high dielectric constant on both sides of the kink site, we should not expect a deep trap here, perhaps not much deeper than that due to an interstitial ion. Probably the deepest traps are those due to adsorbed silver ions not at kink sites, and it may well be that the first process in the formation of surface latent image is the trapping of an electron here, to form an adsorbed silver atom, It will be realized that this differs from a free atom, the wave function being greatly distorted by the crystal.

One or other of these sites produces traps about 0·2 ev in depth. The evidence comes from observations on the space charges produced by illumination of crystals of silver bromide in electric fields at liquid air temperature. The rate of decay of the space charge at a temperature of −140°c, after removal of the field points to a trap depth of this order (Braun and Mitchell 1957).

If the formation of the latent image starts by the movement of an electron, liberated say $\frac{1}{2}$ micron from the surface, to an adsorbed ion on the surface, we may estimate the time involved. If the ion is the only trap within a micron, the electron will have to wander over say 10^{10} atomic sites to find it, or a total distance of about 10^2 cm. With a thermal velocity of about 10^7 cm/sec this should take 10^{-5} sec. The sort of field F required to pull it across a grain in this time (as in the experiments of Webb), with a grain size $10\,\mu$ and mobility 50, is given by the following equation

$$F \times (50 \text{ cm}^2/\text{volts cm}) \times (10^{-5} \text{ sec}) = 10^{-3} \text{ cm}$$

whence

$$F \sim 1 \text{ volt/cm}$$

Webb's fields are considerably greater than this.

We now consider the mobility of a positive hole. That of an electron should of course *increase* at low temperatures. It is very likely on the other hand that, owing to its comparatively high effective mass, the hole will polarize its surroundings and form a *polaron* (Mitchell 1957 b, cf. also the review by Allcock 1956). In that case the mobility will become *small* at low temperatures, though it will probably exceed that of an interstitial ion. A similar suggestion could account for the activation energies in the mobilities of positive holes (Ni^{3+} ions) in nickel oxide and in α–Fe_2O_3 (Morin 1954).

Fig. 4

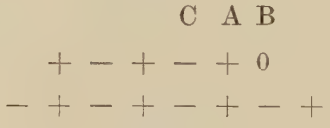

Ions at a kink site.

We now turn to the question of the trapping of positive holes, particularly by surface sites such as kink sites occupied by bromide ions, or adsorbed silver sulphide. Here we have two questions to ask:

(i) Is the positive hole trapped ?

(ii) Does the positively charged centre so formed dissociate, in the sense that a positive ion moves away ? If so, a centre is produced which cannot trap an electron, so that recombination cannot occur in the presence of a mobile electron. If not, as at low temperatures, recombination can occur between the trapped hole and a free electron, giving the luminescence and low photochemical efficiency observed at liquid air temperatures (Meidinger 1944, Farnell *et al.* 1950, Biltz 1952).

Consider then a hole which comes to a bromide ion at a kink site. There will certainly be a trap here, but it cannot be a stable trap, because we know that, when Br_2 is adsorbed on silver bromide, holes can diffuse in and oxidize internal silver. Thus the hole can either move away again,

or stay there (at the point B in fig. 4) until the cation A diffuses away, for example into an interstitial position. Then the molecule Br_2 (at a kink site) is formed, and this may well be relatively stable. Br_2 will then be formed if another hole comes to the same point. But the situation cannot be entirely stable unless the bromine molecule escapes, because as we have seen adsorbed bromine will attack even internal silver (Mitchell 1957 a, b, e).

Consider now the case of adsorbed silver sulphide (Ag_2S). The effect of sulphur sensitization is to allow the formation of surface image, particularly at low intensities of illumination. It seems then that Ag_2S provides a *stable* trap for positive holes (unlike a bromine ion at a kink site), which does not allow the positive holes to move away and attack neighbouring sub-image.

The dissociation process which occurs when Ag_2S traps a positive hole, thus making it impossible for it to accept a photoelectron, must, we suggest, be the diffusion away of a silver ion to leave a divalent AgS molecule (Mitchell 1956).

§ 5. The Photochemical Process

Illumination of a silver halide crystal produces, we have seen, mobile electrons and positive holes ; the latter we believe to have some mobility if the temperature is not too low. The silver bromide crystal also contains mobile interstitial ions and silver ions mobile on the surface and along edge dislocation lines. The photochemical process involves a discussion of the following points :

(*a*) Unless the positive holes diffuse to the surface and are trapped, and halogen escapes, or some other reaction occurs to prevent recombination with an electron, no latent image or photolytic silver can be formed, since the holes and electrons will eventually recombine. Some indication of how this occurs has already been given.

(*b*) Both internal and surface silver are formed ; it is surface silver that is important for latent image formation using developers that do not dissolve the halide.

We need to discuss

(i) Photolysis, i.e. the growth of silver specks when already nucleated, and also solarization, which is the transference of surface silver to internal sites (Mitchell 1957 b).

(ii) Nucleation, i.e. the initial formation of the ' latent sub-image ', which, following Webb (1950 a, b) and Katz (1949, 1950), we believe to be a pair of silver atoms, and its subsequent growth to a stable latent image, which we shall give evidence to suggest consists of not less than three silver atoms adsorbed to the surface of the silver bromide.

Having already discussed the escape of halogen, we shall consider the formation of photolytic silver first. Here the Gurney–Mott principle is well established and the theory originally proposed by Gurney and Mott essentially correct ; we need only modify it by pointing out again that photolytic silver is positively charged, so that instead of saying that the photoelectrons charge silver specks negatively, and the interstitial ions are attracted, we prefer to present the phenomenon the other way round ; the specks attract the photoelectrons. Evidence of the positive charge on internal silver is provided by the slowness of its rehalogenation, a process which is rapid in the case of surface silver. Here we suppose that halogen molecules are dissociated on the surface and that halogen atoms are adsorbed at kink sites, which are transformed into ions (Br^-) by positive holes diffusing inwards. These cannot get to the internal silver, because of its positive charge. The slow oxidation probably takes place through the diffusion to it of holes together with cation vacancies, which will remove the silver ion and the electron.

One of the outstanding successes of recent research is the demonstration (Hedges and Mitchell 1953 a, b, Evans and Mitchell 1955, Mitchell 1957 c, e) that inside both large single crystals and photographic grains, visible photolytic silver is usually formed along dislocations. This is in fact one of the most powerful methods of decorating dislocations and perhaps the only one that operates at room temperature. Here one has to do with specks of silver containing many atoms (probably 10^6 or more). We believe the dislocations play their role in promoting *nucleation*, but here, as in other methods of decoration where gold is allowed to diffuse into dislocations (Barber *et al.* 1957), there is some uncertainty as to how the halogen escapes to make room for the silver. It is not of course sufficient that positive holes should diffuse away ; halogen nuclei must move too.

Consider now a crystal grain which is under illumination, and in which internal and surface silver is growing. The halogen has to escape from the *surface* (Br^- ions there being turned into atoms by positive holes). If bromine or a positive hole meets a silver speck, it oxidizes it. (A hole will lead to the escape of a metal ion which ultimately recombines with a halide ion at a kink site.) We see therefore that there is a strong tendency for growth of internal silver to lead to oxidation of surface silver.

In fact, without sulphur sensitization, *no* surface silver is formed. A role of the silver sulphide, then, must be to prevent positive holes from oxidizing surface silver. This has already been stated in the last section. And solarization occurs, we conclude, when all the silver sulphide has been used up, so that holes coming from the interior can do nothing but attack the surface silver.

Finally, to understand photolysis, we need a mechanism for the escape of halogen when positive holes diffuse to the surface. This too has been outlined in the last section (see also Mitchell 1957 a, b, e for a fuller discussion).

§ 6. Latent Image Formation

In this work we distinguish between the latent sub-image and the latent image. The latent sub-image has the following characteristics (Berg 1948).

Grains carrying a sub-image are only developed with a long induction period or a vigorous developer.

Post-exposure or latensification may render such grains developable.

Illumination with radiation such that $h\nu$ exceeds 1·54 ev may make such grains developable, or may induce Herschel effect (transference of silver to the internal image).

Flash illumination at high intensities produces a preponderance of sub-image.

Storage of an exposed emulsion with sub-image may produce normal latent image.

We next give a review of the evidence obtained by Evans, Hedges and Mitchell (1955) by evaporating silver on to a silver bromide surface. The evidence establishes :

(*a*) The mobility of silver atoms on a *clean* (i.e. free of gelatine) surface at room temperature.

(*b*) A layer of less than 10^{14} atoms cm^2 gives the effects of a sub-image ; that is to say it will develop only with a long induction period unless an active developer is employed, but on storage becomes easily developable. Photographic evidence reviewed below will suggest that the sub-image is a pair of atoms, that these are not stable and slowly (in hours or days) coagulate into larger specks.

(*c*) The deposition of gelatine stabilizes the surface sub-image but does not affect the internal sub-image.

(*d*) The deposition of more than 10^{15} atoms cm^2 produces a stable latent image immediately developable ; photographic evidence reviewed below will suggest that the minimum stable developable image is *three* silver atoms, probably with an adsorbed ion (Ag_4^+).

This work shows clearly for the first time that the latent image *is* silver in clusters of a few atoms adsorbed on silver bromide, and we shall proceed on this assumption.

We shall consider single adsorbed atomic clusters of two, three, four and so on. From the behaviour of the silver–silver bromide electrode, it may be deduced that massive silver in contact with silver bromide acquires a positive charge (for a theoretical treatment see Grimley and Mott 1947). On the surface of a bromide grain there are positive ions, which can combine with one of these aggregates to give it a charge ; it is to be expected that the binding energy will increase with the size of the aggregate. We shall give evidence to suggest that a silver atom adsorbed adjacent to a kink site occupied by a silver ion (pre-image speck) dissociates in from 10^{-5} to 1 sec, that Ag_2 (the sub-image) is not charged for most of its time, but Ag_3 (the smallest stable image) will

absorb and hold an ion to form Ag_4^+, this being the smallest aggregate that is charged most of the time (Mitchell 1957 a, b, e).

We discuss now the initiation of a silver particle on the surface of silver bromide when photo-electrons are produced within the crystal. It is reasonable to suppose that the first process is the trapping of an electron by an excess silver ion. We have already deduced from the experiments of Haynes and Shockley and the calculations of Simpson (1955) that interstitial ions will give very shallow traps, and ions at kink sites, carrying a half-charge only, are likely to provide a very shallow trap too. The deepest traps will probably be due to adsorbed silver ions, though these are not deep enough to give stable trapping at room temperature. We have already suggested a trap depth of 0·2 ev. An adsorbed silver atom, then, will rapidly dissociate into an ion and an electron in the conduction band.

We tentatively assume, then, that the sequence of events is the following (Mitchell 1951, 1952, 1957 a, b).

(1) A photo-electron after it is produced is momentarily trapped by a silver ion at a site adjacent to a kink site occupied by a silver ion to form an adsorbed silver atom, with a short life time at room temperature though it may be stable at low temperatures. This process may take several milliseconds, since the chance of an extra ion being close to any kink site is small†. We shall deduce below from an interpretation of the reciprocity curve that this aggregate has a mean life time of from 1 to 10^{-5} sec, according to the kind of site occupied, dissociating into a silver ion and an electron in the conduction band. Such a silver atom adsorbed at a kink site we shall call a 'pre-image speck'.

(2) If another silver ion and electron arrive before the pre-image speck dissociates, a much more stable aggregate of two silver atoms, Ag_2, is formed. This we believe to be the sub-image. Emulsions exposed so that the sub-image only is formed are, as we have seen, developable only with a long induction period except in a vigorous developer. In § 9 we shall interpret this as showing that they do not normally carry a positive charge; the binding energy is not yet strong enough for Ag_3^+ to be stable. Also we have seen above that post-exposure makes the emulsion easily developable; the mechanism proposed is that, after losing electrons into the conduction band, the sub-image specks split up into ions and electrons which gives them a chance to combine into larger aggregates. Alternatively the electrons may be transferred to the internal image, resulting in bleaching when a surface developer is used (Herschel effect). It should be noticed that Herschel effect occurs only with the sub-image; emulsions with stable internal or surface image do not show it, because, as emphasized already, they carry a positive charge, so a greater energy is required to eject an electron into the conduction band of the silver halide.

† In Webb's work on the displacement of photolytic silver by a pulsed field, if the pulse is delayed by about 1 microsecond after illumination, no displacement is observed. However, in this work photolytic silver already was present.

The sub-image, if the emulsion is stored for days, decomposes into a stable image. In the absence of gelatine, sub-image specks should not be so stable and would aggregate quickly into larger aggregates. This is perhaps why sub-image is seldom formed in the interior.

The next step in the formation of the latent image is probably the adsorption by the sub-image of a silver ion, and during the comparatively short life time of the configuration Ag_3^+ the addition of another photo-electron. The stable latent image Ag_3 is then formed. It is likely that it will combine with an ion Ag^+ and form a stable tetrahedral arrangement Ag_4^+ (Burrow and Mitchell 1954).

Fig. 5

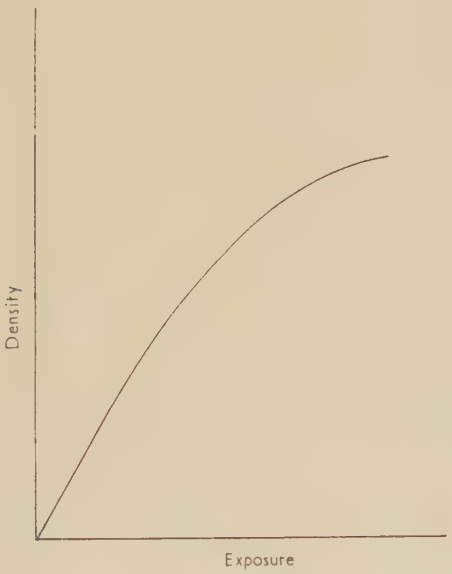

Relation between developed density and exposure for an emulsion containing sub-image (Berg 1948).

There is good evidence that aggregates of *three atoms* can form a stable latent image. This is as follows: Sub-image can be formed all over a grain by a short exposure of high intensity. After such an exposure an emulsion has a *linear* characteristic curve for small exposure times, as in fig. 5 (see Berg 1948). This shows that only a *single* process in each grain is necessary to make it easily developable; hence we deduce as above that one atom added to the sub-image forms a stable latent image.

We must now consider again the escape of halogen. In a grain there will normally be formed, at the same time, internal image and surface image. From the internal image positive holes will be streaming out to the surface. The sub-image, which (unlike the internal image) does *not* carry a positive charge, will provide deep traps for these holes, and as

soon as a sub-image speck receives one it will dissociate (i.e. be destroyed). Surface image will not have a chance to form unless something is done on the surface to dispose of these holes. Kink sites are not enough, even though on a rough surface there are likely to be many more of them than of sub-image specks, because we have seen that they cannot stabilize the hole unless Br_2 actually escapes and to form Br_2 takes two holes. It appears that adsorbed Ag_2S, if present in a sufficient quantity on the surface, *does* trap holes, and also makes recombination with another electron unlikely, since the Ag_2S^+ will dissociate into AgS and an interstitial silver ion.

Silver sulphide plays another role. To show this we may quote further experimental results of Evans, Hedges and Mitchell (1955, see also Mitchell 1957 a, b, d). If silver (less than a monolayer) is evaporated on crystals of silver bromide, some diffuses (along dislocations) into the interior ; this is shown by the fact that after dissolving the surface, the crystals are fogged—i.e. can be developed. But if Ag_2S is deposited on the surface first, this does not occur. Thus Ag_2S on the surface stabilizes silver atoms there. In emulsions this will occur too ; if emulsions are sensitized under reducing conditions silver atoms will be formed and adsorbed to silver sulphide on the surface, and in any case those formed photolytically will be prevented from diffusing into the interior. Russian workers (e.g. Chibisov 1956) believe that chemical sensitization is due only to silver formed on the surfaces of the crystals and that silver sulphide only plays a secondary role. We are unable to accept this viewpoint.

In the original Gurney–Mott theory it was assumed that the role of silver sulphide was to trap electrons. There is no evidence that it does this and some evidence against. If otherwise identical sulphur-sensitized and non-sensitized emulsions are compared, the latter has no surface image but the amounts of internal image in the two are often practically identical. Our hypothesis is that the sulphide prevents holes (or halogen) escaping from the internal image from oxidizing the surface sub-image. If the role of Ag_2S was to trap electrons on the surface, thus producing surface image, we should expect it to lead to a compensating reduction in the intensity of the internal image, which is often not observed (see Mitchell 1957 e for further discussion).

§ 7. Reciprocity Failure

The main features of reciprocity failure can be explained in terms of the model we have put forward (Mitchell 1957 a, b, e), and the study of this phenomenon gives us a good deal of information about the formation of the latent and sub-images.

What is meant by reciprocity failure is illustrated by the curves shown in fig. 6. Here I is the intensity of exposure and t the time of exposure, so that It is the energy falling on the emulsion. What is plotted is the

value of It required to give a certain developed density against I (or the reciprocal of t). The points to note are :

(*a*) High intensity failure occurs only for incomplete development, and is thus due to the use of all or nearly all the absorbed light in forming the sub-image.

(*b*) The turn-over point X occurs at times of the order 10^{-5} sec at room temperature.

(*c*) Internal image does not show high intensity failure ; it will be remembered that sub-images (Ag_2) are stabilized only by gelatine, and are not stable but form larger aggregates on internal surfaces.

Fig. 6

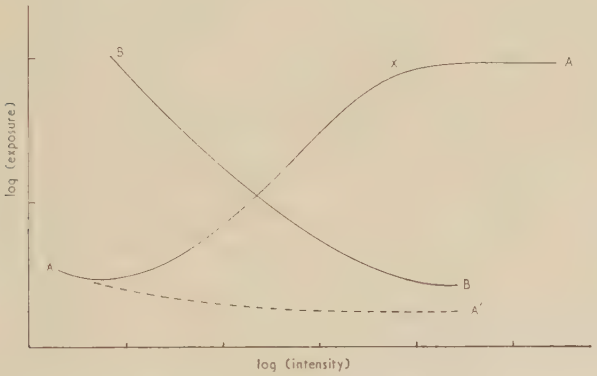

Types of curve showing failure of reciprocity at room temperature
AA', Surface latent image, incomplete development.
AA, Surface latent image, complete development.
BB, Internal image.

(*d*) Low intensity failure is shown both by surface and internal latent images, more strongly by internal image.

(*e*) Webb (1950 a) has measured the temperature-dependence of the curve. As the temperature is raised or lowered the curve, for a given emulsion and developed density, is shifted to the right or left as a whole. Thus the whole curve at high and low intensities must depend on the time taken by the same temperature-dependent processes. Assuming that the times depend on temperature according to a formula of the type $\tau_0 \exp\{W/kT\}$, Webb obtains the following rough values of W

Surface image	0·77 ev
Internal image	0·65 ev.

With a reasonable value of τ_0 (say 10^{-12} sec), the former would give times of about 20 sec.

We believe that the process concerned is the dissociation of a silver atom adsorbed at a kink site adjacent to a silver ion on the surface of the grain ; this is a latent pre-image speck which is formed when the first electron combines with an interstitial silver ion next to a kink site occupied

by another silver ion (Mitchell 1957 b). It cannot be the dissociation of the sub-image, which takes days. The activation energy might well be higher on the surface than in the interior (on dislocations) because of the stabilizing effect of gelatine. We do not wish to imply that there will be, precisely, a single activation energy for this process ; the various states of roughness of the surfaces of different grains must give some range of energies. The flattening of the curve for high values of $I(t \sim 10^{-5}$ sec) suggests that on some sites the times are as low as 10^{-5} sec, which would correspond to about 0·4 ev.

The detailed explanation is then as follows. Low intensity failure is due to the slow recombination, with the help of ionic movement, of electrons with positive holes—in whatever form the positive holes are, for instance in the sulphide traps already described. It will be remembered that to form a sub-image *two* electrons are required, the first forming a latent pre-image speck ; if this dissociates before the second electron arrives, the first electron is thrown back into the conduction band and has another chance of recombination. It will be realized that, since the (positively charged) trapped hole has dissociated into neutral AgS and interstitial Ag^+, this will require the cooperation of an interstitial ion, and may be a slow process. But at very low intensities the electron will be thrown back hundreds of times, and so normally disappear before the next one comes. This applies to surface and internal image.

With high intensity exposures many adsorbed silver atoms will combine with a second silver ion and electron before they dissociate, and by the time that the sub-image has collected another ion to form Ag_3^+, there are no electrons left to form the stable image Ag_3. If the flash is shorter than the dissociation time for all the adsorbed silver atoms, the curve flattens out. The optimum is when the silver atoms normally dissociate before a second electron comes along, so that a photo-electron is thrown back into the conduction band several times, not doing this often enough to give a very high chance of recombination, but often enough to have a good chance of finding a group of silver atoms Ag_3^+ and so forming an easily developable latent image.

§ 8. Dislocations and the Role of Iodide

All the discussion up to this point has emphasized the importance of surface kink sites for the formation of surface latent image. They may have the following roles.

(*a*) To provide sites from which silver ions can move, with low activation energy, towards the surface latent image.

(*b*) To provide sites from which halogen can escape.

At first sight it might be thought that the presence of Ag_2S adsorbed to the surface of sulphur-sensitized grains would make the second role unimportant ; but there is evidence (Evans, Hedges and Mitchell 1955) that on a smooth surface the Ag_2S forms aggregates which can initiate development, giving fog. On a rough surface a monolayer can be formed,

probably because kink sites serve as centres at which the formation of the monolayer can begin.

Tabular grains of silver bromide contain a region in the middle which has a higher sensitivity than elsewhere. This was shown directly in experiments already referred to (Mitchell 1957 a) in which illumination with a point of light near the centre of a large grain produced more latent image and print out silver (in the illuminated region) than illumination near the edges. This central region has been called the sensitivity centre. It is here that internal as well as surface silver is formed.

Fig. 7

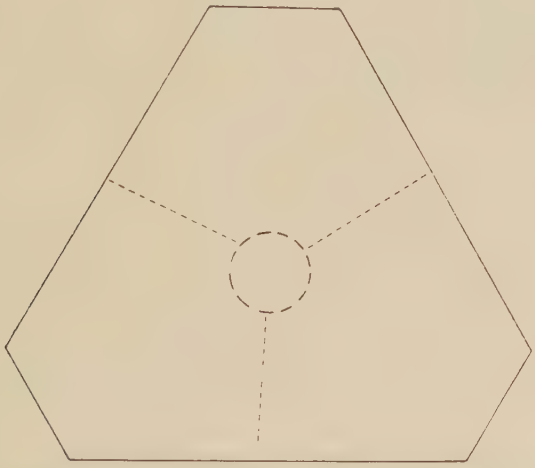

Tabular grain showing sensitive centre (the dotted curve) and three dislocations with screw components (on dotted lines).

A typical tabular grain with an octahedral surface may be as in fig. 7. Three screw dislocations determine the pattern of growth and may be decorated by illumination and seen under the microscope (the crystals may be etched at the points where these screws meet the surface or silver whiskers deposited on them). As for the central region, since

(*a*) it shows surface sensitivity ;

(*b*) internal silver separates there ;

(*c*) there is no evidence of spiral growth patterns centred there in the octahedral faces.

We believe that this region contains mainly *edge* dislocations perpendicular to the octahedral planes. These would serve as nuclei for internal silver, and roughen the surface by serving as centres of shallow etch pits formed during ripening ; such pits have been observed (Evans and Mitchell 1955).

The majority of photographic emulsions of high sensitivity consist of crystals of bromo-iodide suspended in gelatine, and there is evidence that a main role of the iodide is to introduce crystal imperfections In many emulsions, the nuclei upon which the microcrystals grow may

consist of silver iodide with the wurtzite structure, the layers subsequently deposited upon these nuclei being richer in silver bromide (Chateau and Pouradier 1954, Raynaud and Pouradier 1955, Berry and Marino 1955). Between nucleation and the completion of crystal growth, a re-arrangement of the nucleus may occur apparently giving a transformation to the rock salt structure. Both on account of the strains set up and the sharp concentration gradient, many dislocations will be introduced (Mitchell 1957 a, b, e).

A further effect of iodine is the optical sensitization of silver bromide crystals which results from the incorporation of silver iodide in them. The edge of the lattice absorption band is extended to longer wavelengths because of the lower electron affinity of iodine atoms compared with bromine atoms. A consequence of this is also that positive holes are trapped by surface iodide ions in silver bromo-iodide crystals so that iodine is liberated from their surfaces (Pouradier and Chateau 1954).

§ 9. Development

Development, once the process has started, may be described as follows. Developed silver is present in a highly dispersed crystalline form. Silver in the presence of developer acquires a negative charge, electrons being transferred from the developer to the metal and a double layer set up. On the other hand, as we have seen, silver in contact with silver halide acquires a positive charge, silver ions being transferred from the halide to the metal. (In our discussion in § 2 we referred to the adsorption of silver ions from the silver bromide ; here silver ions will move through the liquid presumably from halide kink sites to the silver, halide ions going into solution.) The silver will thus grow.

The form of the developed silver will depend on the reduction potential of the developer. For amidol this is high, and one gets the filamentary form shown first with the electron microscope. This is believed to be because the developer is active enough to keep the silver negatively charged, so that silver ions are attracted to the ends of filaments where the field is strongest. For the less active metol-hydroquinone, on the other hand, the silver is positively charged ; there is thus no tendency to filamentary growth and hence spongy masses of polycrystalline silver are formed (Keith and Mitchell 1953, Mitchell 1955).

For the purpose of this paper the most important point is to understand the long induction period for the development of grains containing only a sub-image. Here the key fact is this ; we have given evidence to suggest that the sub-image consists of a pair of uncharged silver atoms adsorbed to the surface of the bromide crystal. It is hardly likely that so small an aggregate has a level for a further electron below the bottom of the conduction band, so however great the reduction potential of the developer it cannot acquire a negative charge. We must assume that the stable latent image (with a minimum size of three neutral atoms and one ion) has such a level and can, on account of its positive charge.

Thus for development induced by a sub-image we have to wait until a mobile silver ion is momentarily in contact with the latent sub-image (forming Ag_3^+, which we have seen to be unstable) and at the same time a molecule of developer is in position to hand over an electron. This we believe accounts for the induction period (Mitchell 1957 a, b, e).

The initiation of rapid development by a latent sub-image, then, is preceded by a relatively long induction period due to the low heat of adsorption of silver ions to the pairs of silver atoms of the sub-image and to the inability of these pairs to trap electrons from developer molecules. The induction period may be reduced by gold sensitization or by gold latensification which leads to the formation of latent sub-image specks containing gold atoms. It is likely that a *pair* of metal atoms of which one is gold may be able to hold a third for a much longer time (say as Ag_2Au^-), so as to form a centre capable of accepting an electron and initiating development (Burrow and Mitchell 1954).

References

Allcock, G. R., 1956, *Advanc. Phys.*, **5**, 412.

Apker, L., and Taft, E., 1951, *Imperfections in nearly Perfect Crystals* (New York : John Wiley), p. 246.

Arrhenius, S., 1887, *S.B. Akad. Wiss. Wien*, **96**, 831.

Barber, D. J., Harvey, K. B., and Mitchell, J. W., 1957, *Phil. Mag.*, **2**, 704.

Berg, W. F., 1948, *Rep. Progr. Phys.*, **11**, 248.

Berry, C. R., and Marino, S. J., 1955, *Photogr. Sci. Technique*, **2**, 149.

Biltz, M., 1952, *J. opt. Soc. Amer.*, **42**, 1952.

Braun, E. A., and Mitchell, J. W., 1957, *Phil. Mag.*, to be published.

Burrow, J. H., and Mitchell, J. W., 1954, *Phil. Mag.*, **45**, 208.

Chateau, H., and Pouradier, J., 1954, *Sci. Industr. Photogr.* (2), **25**, 3.

Chibisov, K. V., 1956, *Z. wiss. Photogr.*, **51**, 59.

Clark, P. V. McD., and Mitchell, J. W., 1956, *J. Photogr. Sci.*, **4**, 1.

Ebert, I., and Teltow, J., 1955, *Ann. Phys. Lpz.*, (6), **15**, 268.

Eggert,. 1926, *Z. Electrochem.*, **32**, 49.

Evans, T., Hedges, J. M., and Mitchell, J. W., 1955, *J. Photogr. Sci.*, **3**, 73.

Evans, T., and Mitchell, J. W., 1955, *Defects in Crystalline Solids* (London : Physical Society), p. 409.

Fan, H. Y., 1955, *Solid State Physics* (New York : Academic Press), **1**, 283.

Farnell, G. C., 1952, *Phil. Mag.*, **43**, 289.

Farnell, G. C., Burton, P. C., and Hallama, R., 1950, *Phil. Mag.*, **41**, 157, 545.

Franck, J., and Teller, E., 1938, *J. chem. Phys.*, **6**, 861.

Grimley, T. B., and Mott, N. F., 1947, *Disc. Faraday Soc.*, **1**, 3.

Gurney, R. W., and Mott, N. F., 1938, *Proc. roy. Soc.* A, **164**, 151.

Hamilton, J. F., Hamm, F. A., and Brady, L. E., 1956, *J. appl. Phys.*, **27**, 874.

Haynes, J. R., and Shockley, W., 1948, *Report on Conference on Strength of Solids* (London : Physical Society), p. 151 ; 1951, *Phys. Rev.*, **82**, 935.

Hedges, J. M., and Mitchell, J. W., 1953 a, *Phil. Mag.*, **44**, 223 ; 1953 b, *Ibid.*, **44**, 357.

Katz, E., 1949, *J. chem. Phys.*, **17**, 1132 ; 1950, *Ibid.*, **18**, 499.

Keith, H. D., and Mitchell, J. W., 1953, *Phil. Mag.*, **44**, 877.

Luckey, G. W., and West, W., 1956, *J,. chem. Phys.*, **24,** 879.
Meidinger, W., 1944, *Fortschr. Photogr.* **3,** 1.
Mitchell, J. W., 1951, *Bull. Soc. Roy. Sci. Liège*, **20,** 300 ; 1952, *Sci. Industr. Photogr.* (2), **23,** 457 ; 1955, *Chemistry of the Solid State* (London : Butterworths), p. 311 ; 1956, *Z. Elektrochem.*, **60,** 557 ; 1957 a, *Die photographische Empfindlichkeit* (Darmstadt : Verlag Helwich) ; 1957 b, *J. Photogr. Sci.*, **5,** 49 ; 1957 c, *Dislocations and Mechanical Properties of Crystals* (New York : John Wiley), in the press ; 1957 d, *Proceedings International Conference on Scientific Photography, Cologne*, 1956 (Darmstadt and Vienna : Photographische Korrespondenz) ; 1957 e, *Rep. Progr. Phys.* (London : Physical Society), **20,** in the press.
Morin, F. J., 1954, *Phys. Rev.*, **93,** 1195.
Mott, N. F., 1948, *Photogr. J.* B, **88,** 119.
Mott, N. F., and Gurney, R. W., 1948, *Electronic Processes in Ionic Crystals*, 2nd Edn. (Oxford : Clarendon Press).
O'Bryan, H. M., and Skinner, H. W. B., 1940, *Proc. roy. Soc.* A, **176,** 229.
Okamoto, Y., 1956, *Nachr. Akad. Wiss. Göttingen*, No. 14, p. 275.
Overhauser, A. W., 1956, *Phys. Rev.*, **101,** 1702.
Pouradier, J.. and Chateau, H., 1954, *Sci. Industr. Photogr.* (2), **25,** 188.
Raynaud, H., and Pouradier, J., 1955, *Sci. Industr. Photogr.* (2), **26,** 206.
Shapiro, I., and Kolthoff, I. M., 1947, *J. chem. Phys.*, **15,** 41.
Simpson, J. H., 1955, *Proc. roy. Soc.* A, **231,** 308.
Taft, E., and Apker, L., 1957, *Bull. Amer. Phys. Soc.*, in the press
Toy, F. C., and Harrison, G. B., 1930, *Proc. roy. Soc.* A, **127,** 613, 629.
Tutihasi, S., 1957, *Phys. Rev.*, **105,** 882.
Webb, J. H., 1950 a, *J. opt. Soc. Amer.*, **40,** 3 ; 1950 b, *Ibid.*, **40,** 197 ; 1955, *J. appl. Phys.*, **26,** 1309.
West, W., 1951, *Fundamental Mechanisms of Photographic Sensitivity* (London : Butterworths), p. 99.
West, W., and Carroll, B. H., 1947, *J. chem. Phys.*, **15,** 529.
West, W., and Saunders, V. I., 1957, *Proceedings of International Conference on Scientific Photography, Cologne*, 1956 (Darmstadt and Vienna : Photographische Korrespondenz), in the press.

A Note on Single Crystals in Polymers : Evidence for a Folded Chain Configuration†

By A. Keller
H. H. Wills Physics Laboratory, University of Bristol

[Received July 22, 1957]

Summary

The morphology and orientation of a number of polymers as crystallized from solution was studied with the electron microscope combined with selected area electron diffraction. In the course of this work single crystals could be prepared which were most striking in the case of straight chain polyethylenes. There is evidence among others, that the fibrillar (sheaf-type, spherulitic) crystallization, characteristic of polymers, develops through formation of flat single crystals. The single crystals contain screw dislocations and grow by spiral terraces. The observed orientation and the minimum thickness of the crystals leads to the inescapable conclusion that the molecules must bend sharply back on themselves forming a regular folded configuration. Accordingly the strength of the dislocation, consequently the height of growth step, would correspond to the distance between successive bends. Various other observations are consistent with this new concept.

Following up some earlier work (Keller 1955) the author has carried out an investigation on the morphology and crystal orientation of polymers with the aid of combined electron microscopy and electron diffraction. Here a preliminary account will be given of some principal conclusions.

The materials examined were polyethylenes, polyamides (nylons) and guttapercha. The samples were prepared from solution. It was found that thin films, deposited from solutions, showed fibre type orientation with the axis of rotation normal to the film surface. In guttapercha and linear polyethylenes localized regions of the film were identified as single crystals by electron diffraction. In thicker parts of the films or in some specimens crystallized in the form of a suspension within the liquid sheaf type and spherulitic aggregates appeared. It could be seen that these aggregates consisted essentially of curled, coiled or irregularly crumpled flat sheets, and these observations suggest that they arise through a more or less regular rolling up of flat single crystals. What appears to be basic is the flat sheet form of the initial product of crystallization. It is worth mentioning that it has been found by Rhodes *et al.* (1927) that the needle-like habit sometimes found in paraffins results from a regular rolling up of the tabular paraffin crystals. This indicates a

---

† Communicated by F. C. Frank, F.R.S.

plausible link between the flat habit of crystals consisting of long but not polymeric molecules and the fibrillar morphology of polymers.

The most striking observations were made on the linear polyethylene Marlex 50. At first the specimens were prepared by evaporation of the hot solvent (xylene). In this way self-supporting films were obtained. These films showed a polygonal structure with a line pattern (fig. 1†). The films broke along the boundaries of the polygons and pulled threads across the gaps which formed (fig. 2). These polygons were identified as single crystals. It was found by selected area electron diffraction that the *c* axis (the direction of the molecular chains) was either perpendicular to the surface of the film or nearly so, the *b* axis staying in the plane of the film ; and further that the striations were along the *b* axis. It can be deduced from other considerations (Frank, Keller and O'Connor, in preparation) that the *b* direction is that of easiest slip. Accordingly we may have identified slip lines in polymer crystals.

In another method of preparation the polymer was allowed to crystallize in the liquid by cooling the solution under controlled conditions. The resulting suspension was deposited on a supporting film. In this way separate single crystals were obtained. Formation of single crystals in this way has been reported by Till (1957) quite recently after the present observations were complete. Because of Till's publication, description of some of the observations is no longer topical. However, the following addition will be made to what has been reported already.

It was found that if crystallized from sufficiently dilute solutions the crystalline sediment was of uniform appearance. Two types of systematic variation were seen to occur. When crystallized at high temperatures in low concentrations the sediment consisted of lozenge shaped crystals (fig. 3). When temperature of crystallization was lowered, or the concentration increased, or both, the crystals forming became increasingly dendritic in appearance. Figures 3, 4, 5 and 6 show a few stages of this change in habit.

A second phenomenon observed was a central thickening of the crystals in the form of a fold or roll roughly parallel to the *b* axis, becoming more pronounced under suitable conditions of crystallization, and then acquiring a branched sheaf-like appearance (figs. 3 and 7). It is thought that this is the same sheaf-like structure as is recognized to be the initial stage in the development of polymer spherulites (Keller 1955). Within limits this thickening appeared to be promoted by increasing temperature of crystallization and increasing concentration. The fact that this folding or rolling up of the thickened centre of the crystal occurs predominantly along the *b* axis is probably significant, as it might be responsible for the radial *b* axis orientation in the developed spherulites which are known to consist of radiating fibrous units. In dilute solutions the degree of thickening was about uniform throughout the preparation. In more concentrated solutions different stages of thickening could be observed together. Thus fig. 7 shows three lozenges in different stages of

† All figures are plates.

development side by side. The one on the top left has a number of small pyramids growing out of it, the pyramids being formed by spiral terraces. Across each pyramid the above mentioned line of thickening just about appears. The big lozenge on the right is in about the same stage of development as the one in fig. 3, the sheaf shape of the thickened line becoming apparent. In the aggregate on the bottom left the centre has become too thick for any detail to be seen with the electron microscope, but observations made with the optical microscope indicate further development of the sheaf structure in this type of specimen. The details of this sheaf formation are being investigated; it will only be added here that we are not dealing with two different crystal habits or fractions of the material; in the intermediate stage of sheaf formation the lozenge and the sheaf growing out of it form one and the same entity. In samples like that of fig. 7 occasionally completely flat diamond-shaped crystals could also be seen (fig. 8). It was ascertained with reasonable certainty that the observations just listed were characteristic of the whole material and were not given by a particular molecular weight fraction only.

Where the lozenge or dendrite is still flat a system of spiral terraces characteristic of growth by screw dislocation is noticeable (e.g. fig. 5). Till distinguishes growth by screw dislocation (in very low molecular weight material) from growth by layering observed in the bulk of the specimen. Based on the present observations such a distinction does not seem to be justified as spiral terraces can be observed all through the material. These spirals are not immediately conspicuous at the large flat edges of the dendrites where the crystal is only one or two steps thick and the spiral only starts developing from the straight initial ledge.

The most striking feature is the orientation of the molecules. It is found by selected area electron diffraction that the c axis (the direction of the molecular chains) is perpendicular to the surface of the crystal, the a and b axes being respectively along the long and short diagonals of the lozenge. The diffraction patterns are extraordinarily sharp: high orders and secondary reflections also occur (fig. 9). In general the sharpness of the patterns was surprising not only in these but in all the other samples investigated in the course of this work in view of the traditional belief that polymers are necessarily poorly crystalline.

Perpendicular c axis orientation was also found in single crystals of guttapercha. Further it was found with ordinary polythene that the c axes were strongly tilted approaching the perpendicular orientation. Essentially similar observations were made earlier by Storks (1938) and Charlesby (1955) on films as a whole, i.e. not in conjunction with the study of the morphology with the electron microscope. However, the problem of how the long molecules can be accommodated by thin films in this orientation has not been given sufficient attention. At first the exact thickness of the film has to be known. Interferometric methods

proved to be somewhat inconclusive because of big local variations. However, in electron micrographs as in fig. 3 the minimum thickness can be clearly measured. The thickness of the basic layer is about 100 Å. In places it can be smaller, 60–80 Å ; sometimes it is somewhat larger up to about 150 Å. Successive steps or layers are of the same magnitude. In places subterraces of 10–20 Å can be seen bordering the main steps. Secondly the length of the molecules has to be assessed. In the case of guttapercha the possibility of appreciable degradation cannot be overlooked. With polyethylenes this doubt does not arise with the present method of preparation. (Some of our specimens were prepared with the complete exclusion of oxygen which had no effect on the appearance of the crystals.) The molecular weight distribution of Marlex 50 has been determined quite recently (Tung 1957). The results expressed in terms of molecular length show that 6% of the material consists of molecules the length of which is 200 Å or less ; 17, 48 and 29% of the material consists of molecules which have lengths between 200–1000, 1000–7000 and above 7000 Å respectively. The effects observed in the present experiments were characteristic of the entire crystalline sediment not only of a small proportion of it. The same was borne out by our observations on fractions obtained by Richard's method (1946). Consequently it can be stated that the phenomena observed were typical of molecules many hundred and thousand ängströms long. Once this is established the exact length is of no consequence for the picture to be proposed.

The above findings lead to the inescapable conclusion that the long chain molecules must bend back on themselves forming a folded configuration. (This was first suggested by Storks as early as 1938.) This bending back must be sharp otherwise the orientation could not be as perfect as observed. When such bending occurs the free energy per unit weight of the crystallized material must contain a positive term proportional to the number of bends, i.e. inversely proportional to the distance between successive bends (to be referred to as ' bend period ' in the following). If this is small compared with the chain length the crystals should thus be more stable, and less soluble, the longer their bend periods. In the Marlex crystals formed in suspension the thickness of the basic layer hence also that of the successive growth steps would correspond to the bend period. In each particular crystal pyramid the bend period must correspond to the strength of the central dislocation. In those cases (evidently frequent, from the photographs) in which the dislocation forms at the edge of a thin crystal sheet, the dislocation strength will be equal to, or less than, the thickness of the sheet. The latter is probably determined by the nature of a foreign nucleus. The rough uniformity in the observed step heights may therefore be explained by supposing that the crystallites with largest bend period grow preferentially, but that the likelihood of nucleation diminishes rapidly with increasing bend period.

There is further evidence which fits into the picture of single crystals consisting of folded chains. As seen in fig. 2 fine threads can be pulled out sideways from the crystals, and similarly threads can also be pulled out from the more regular-shaped lozenges of the type shown by fig. 3. The specimen was metal shadowed. A periodicity of about 100–300 Å is observable along the threads. Such threads from single crystals could be expected if the chains are folded. The periodicity along the threads would be the consequence of folding. The shadowing metal can only deposit on the top surface of the crystal. When the folds are pulled out there will be metal coated regions at regular distances containing two bend periods.

It is tempting to quote the problem of low angle x-ray scattering at this stage. In practically all crystalline polymers there is a characteristic discrete long angle reflection at a Bragg angle corresponding to about 70–180 Å in different specimens. This is indicative of a structural discontinuity of this magnitude, which appears to be quite general and basic. No satisfactory general explanation exists so far. Low angle x-ray experiments now in progress indicate that it is possible that chain folding is connected with this phenomenon. It will only be mentioned that deformation processes will obviously be deeply affected by the presence of chain folding. In addition to the usual orientation of the crystallites one would expect also an unfolding of the molecules which could occur by slip or other means.

Acknowledgments

The author is greatly indebted to Professor F. C. Frank for frequent advice and numerous stimulating discussions, and to Dr. K. Little for her interest and guidance throughout the electron microscope work.

References

Keller, A., 1955 *J. Polym. Sci.*, **17,** 291, 351.
Keller, A., and Waring, J. R. S., 1955, *J. Polym. Sci.*, **17,** 447.
Rhodes, F. H., Mason, C. W., and Sutton, W. R., 1927, *Ind. Eng. Chem.*, **19,** 935.
Till, P. H., 1957, *J. Polym. Sci.*, **24,** 301.
Storks, K. H., 1938, *J. Amer. chem. Soc.*, **60,** 1753.
Charlesby, A., 1955, *Proc. phys. Soc. Lond.*, **59,** 496.
Tung, L. H., 1957, *J. Polym. Sci.*, **24,** 333.
Richards, R. B., 1946, *Trans. Faraday Soc.*, **42,** 10.
Pierce, R. H., Tordella, J. P., and Bryant, W. M. D., 1952, *J. Amer. chem. Soc.*, **74,** 282.

REVIEWS OF BOOKS

Heat and Thermodynamics. 4th Edition. By M. W. Zemansky. (New York : McGraw-Hill Book Company, Inc.) [Pp. 484.] Price $7.50 (£2 16*s.* 6*d.*).

The fact that this book has been through four editions since it first appeared in 1937 is some indication of its success. Its success is deserved, for it is one of the best accounts of thermodynamics at an intermediate level ; it is lucid and readable, with the right degree of emphasis on rigorous argument. The only misleading thing about it has been its name, since it could never claim to cover ' Heat ' as well or as thoroughly as ' Thermodynamics '. The changes that have been made since the first edition seem designed to counter this criticism, but although they have made the book bigger and more expensive they have not made it better. The edition under review has been diluted with a sixty-page chapter on the physics of very low temperatures, much of which would be quite out of place in any textbook. There is also a section on the Onsager reciprocal relations, where the argument runs distinctly shallow. Such tit-bits may perhaps whet the appetite of some readers, but they weaken the impact of the book as a whole. T. E. F.

Mathematics and Computers. By G. R. Stibitz and J. A. Larivee. (New York : McGraw-Hill Book Company, Inc.) [Pp. 221.] Price $5.00 (£1 17*s.* 6*d.*).

This book gives an excellent general introduction to computers, both of the analogue and digital classes, and to the kinds of work for which such equipment can effectively be used. It is written primarily for the layman, and includes some explanation of mathematical concepts such as complex numbers, functions, and integrals, and of how they occur in the quantitative formulation of practical problems, and also some discussion of what is meant by a ' solution ' of a problem expressed in such a form.

It is concerned with numerical methods, as well as with the principles, and some of the mechanical and electrical details, of both analogue and digital computing equipment. The treatment of numerical methods is illustrated by well-chosen, simple examples, and is carried far enough to include the ideas of ' Monte Carlo ' processes and the generation of sequences of ' pseudo-random ' numbers. In addition to a chapter on the history of computers (digital and analogue) from the abacus onwards, there are two chapters on automatic digital computers (one on components and one on logical designs—which includes programming) and one on analogue computers.

The whole presentation is admirably clear, fresh, and balanced, and free from irrelevancies and extravagances. The book will be found interesting and stimulating by scientists and engineers, as well as by the laymen for whom it is primarily intended. D. R. H.

[*The Editors do not hold themselves responsible for the views expressed by their correspondents.*]

Fig. 1

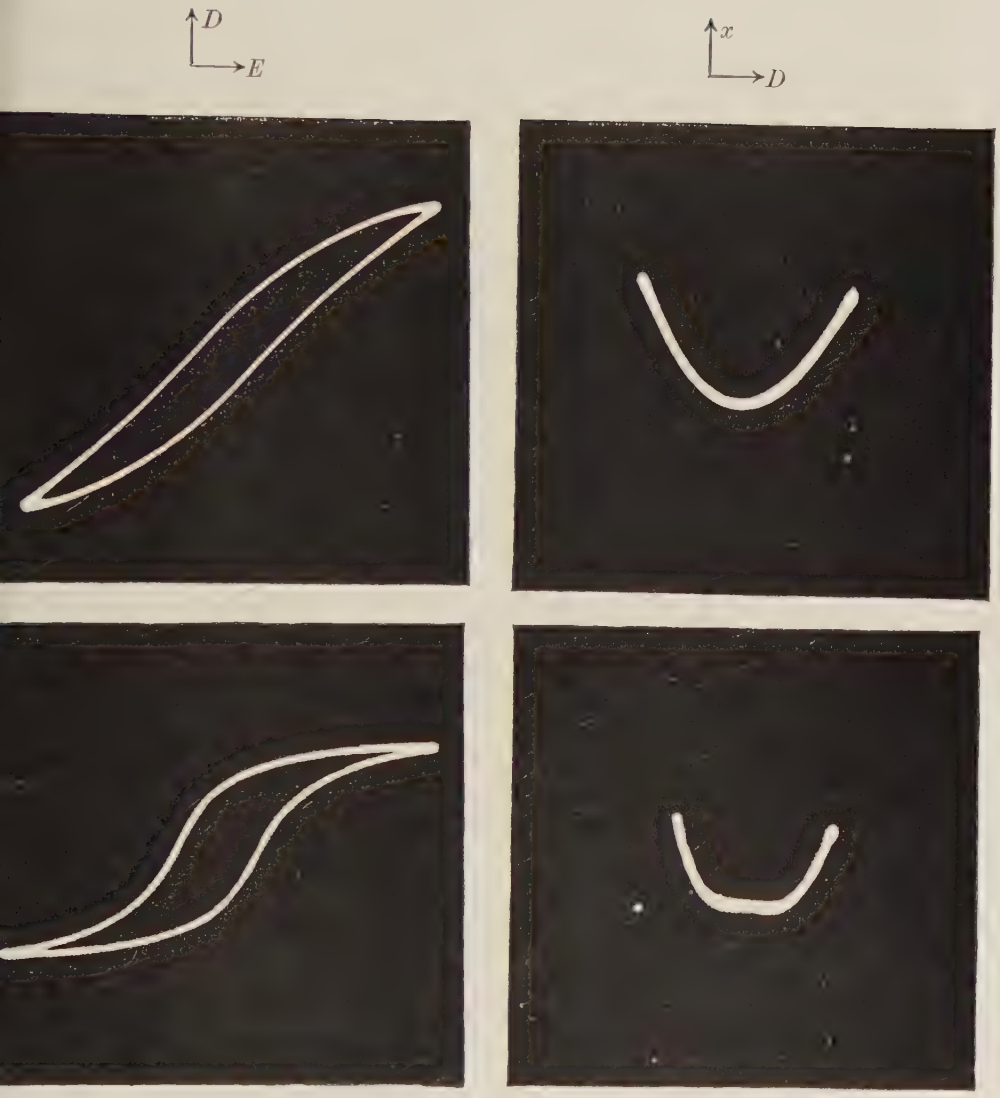

D/E and x/E curves for pure $BaTiO_3$ ceramic.

(*a*) Virgin specimen, not previously subjected to strong fields. $E = \pm 8{\cdot}8$ kv/cm. Polarization $= \pm 5{\cdot}0$ μc/cm^2. Total strain $= 1{\cdot}16 \times 10^{-4}$. (*b*) Same specimen after application of ± 16 kv/cm for 35 minutes. $E = \pm 9{\cdot}1$ kv/cm. Polarization $= \pm 9{\cdot}1$ μc/cm^2 (scale of D changed). Total strain $2{\cdot}5 \times 10^{-4}$.

Fig. 2

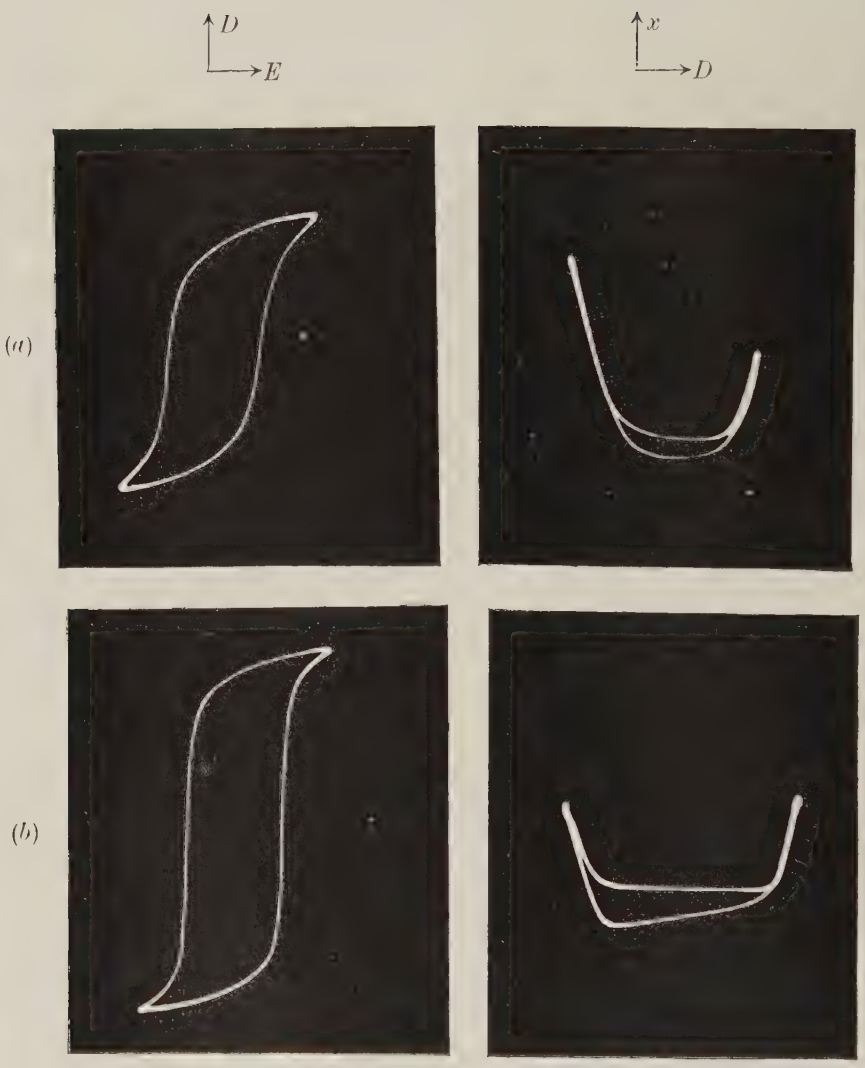

D/E and x/E curves for twinned single crystal of $BaTiO_3$.
(*a*) Virgin specimen. (*b*) After application of 8 kv/cm for 20 minutes.

Fig. 1

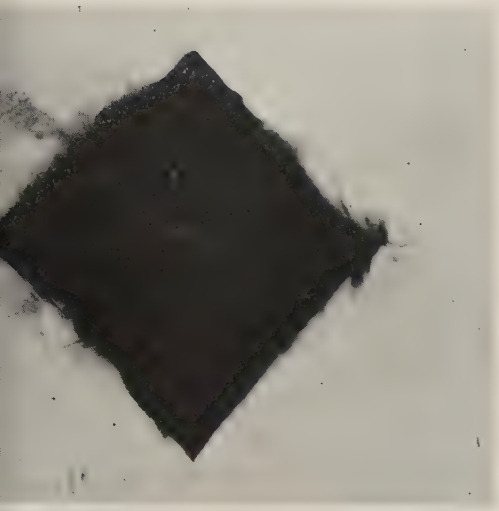

As electrolytically polished and annealed.

Fig. 2

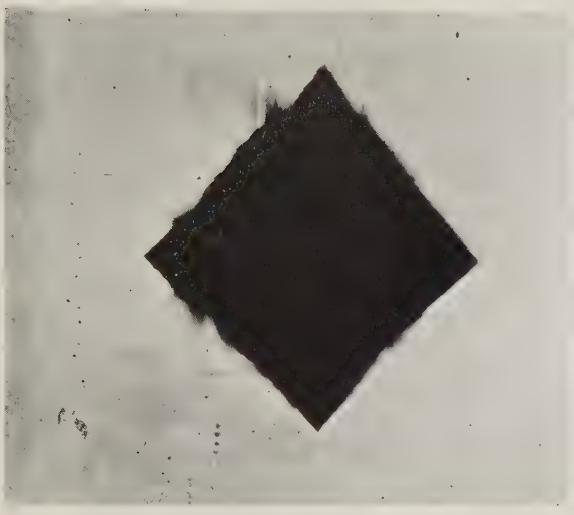

After 1% strain followed by repolishing.

Fig. 3

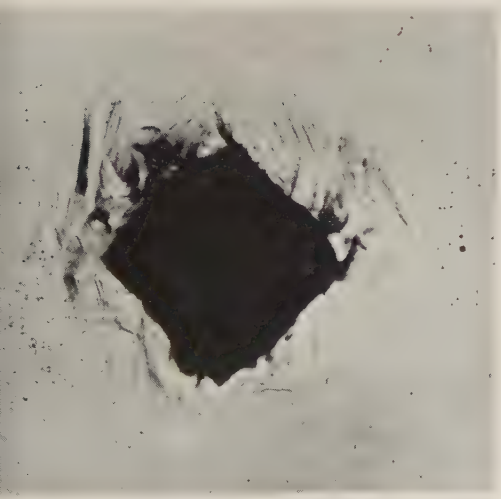

After 30% strain followed by repolishing.

Fig. 4

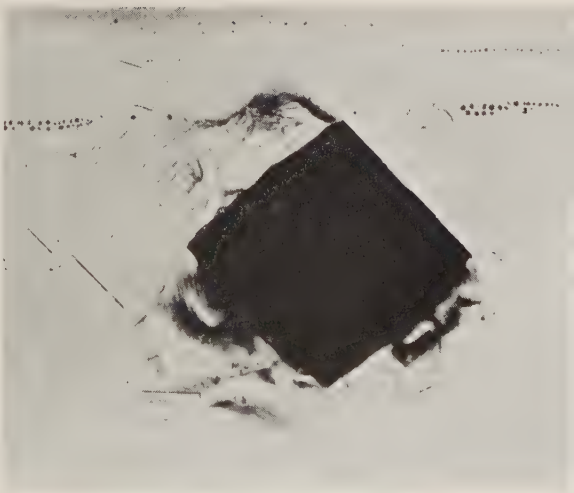

After 6×10^6 cycles at $\pm11\,000$ p.s.i. (20% of life) followed by repolishing

Vickers Hardness Impressions in Polycrystalline Copper ($2\frac{1}{2}$ kg load, 15 sec.) $\times150$.

Fig. 1

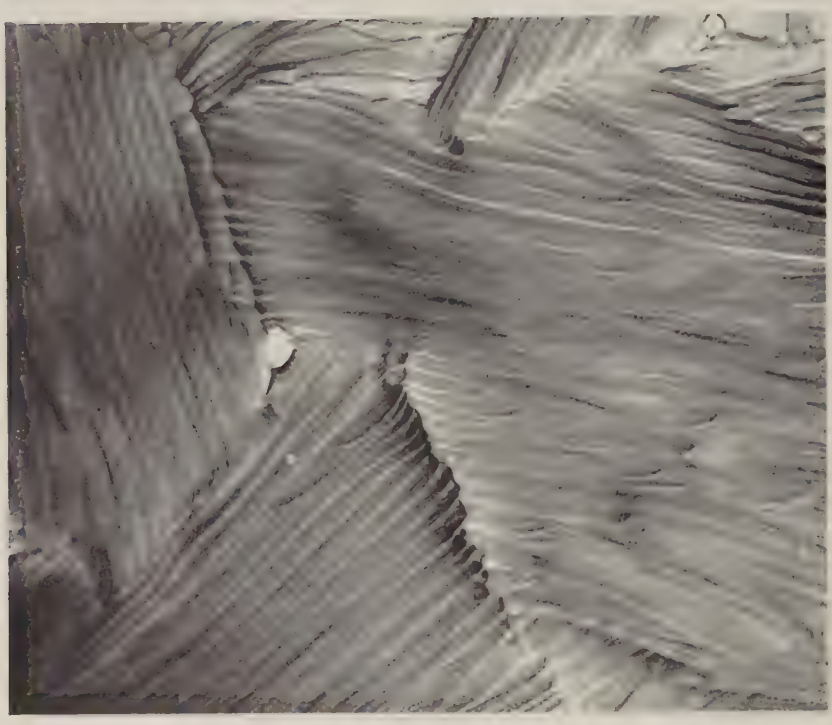

Electron micrograph of Marlex 50. Crystallized by evaporation of hot solvent (xylene). $\times 15\,500$, Au–Pd shadowed.

Fig. 2

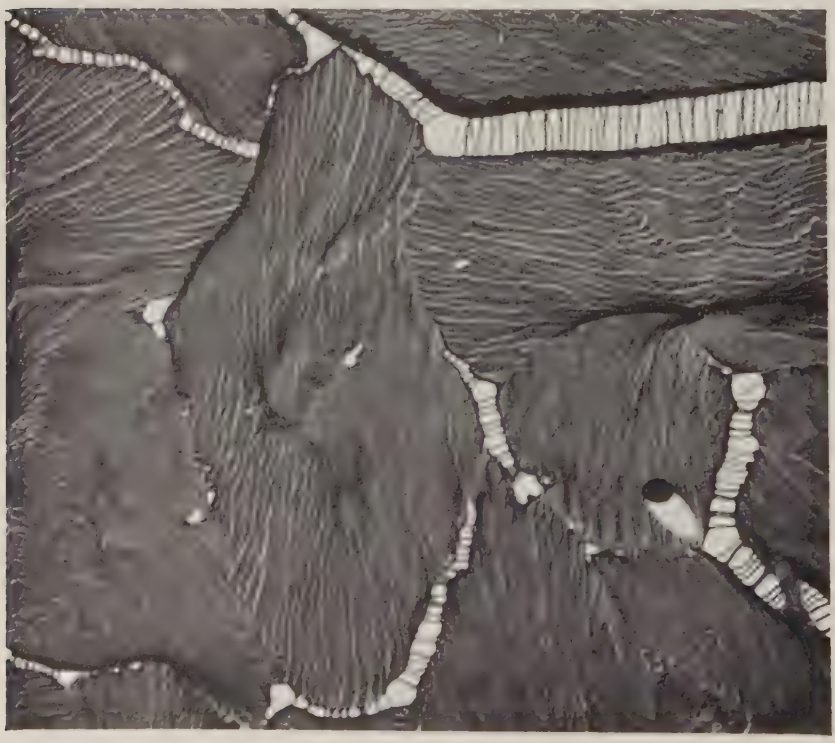

Electron micrograph of Marlex 50. Crystallized by evaporation of hot solvent (xylene). Film breaking up $\times 12\,000$, Au–Pd shadowed.

Fig. 3

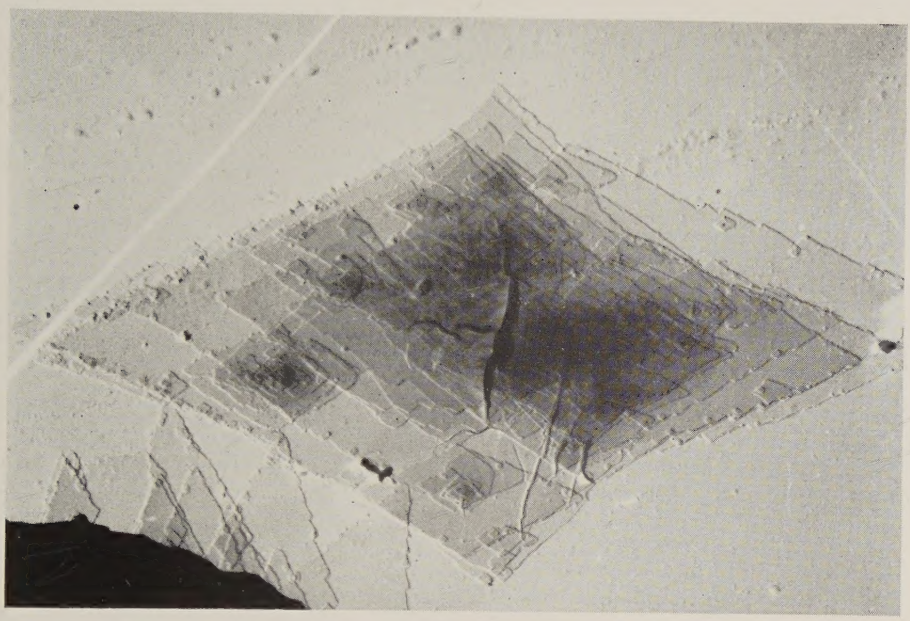

Electron micrograph of Marlex 50. Crystallized in the form of a suspension from 0·01% xylene solution at 78°C. ×5000, Au–Pd shadowed.

Fig. 4

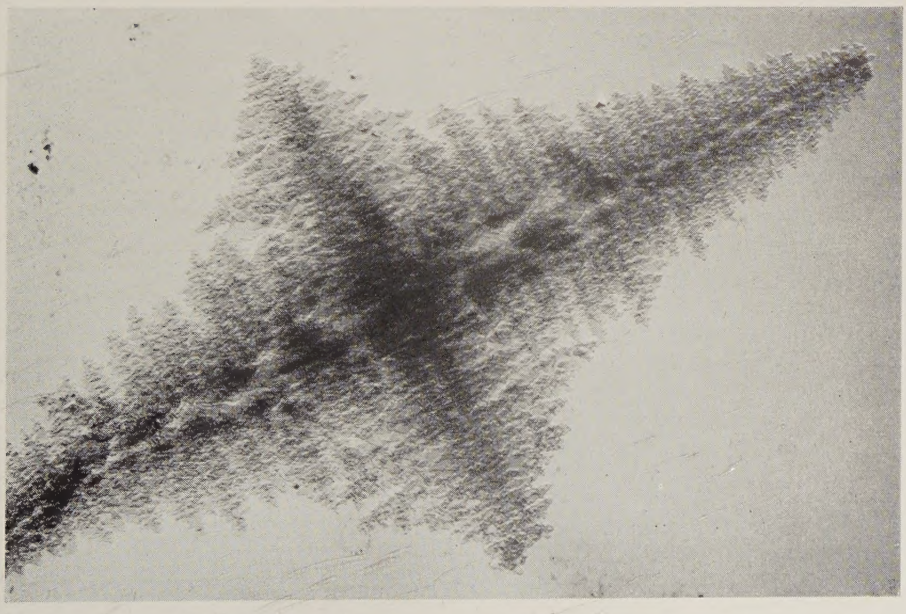

Electron micrograph of Marlex 50. Crystallized in the form of a suspension from 0·01% xylene solution at 69°C. ×3000, Au–Pd shadowed.

Fig. 5

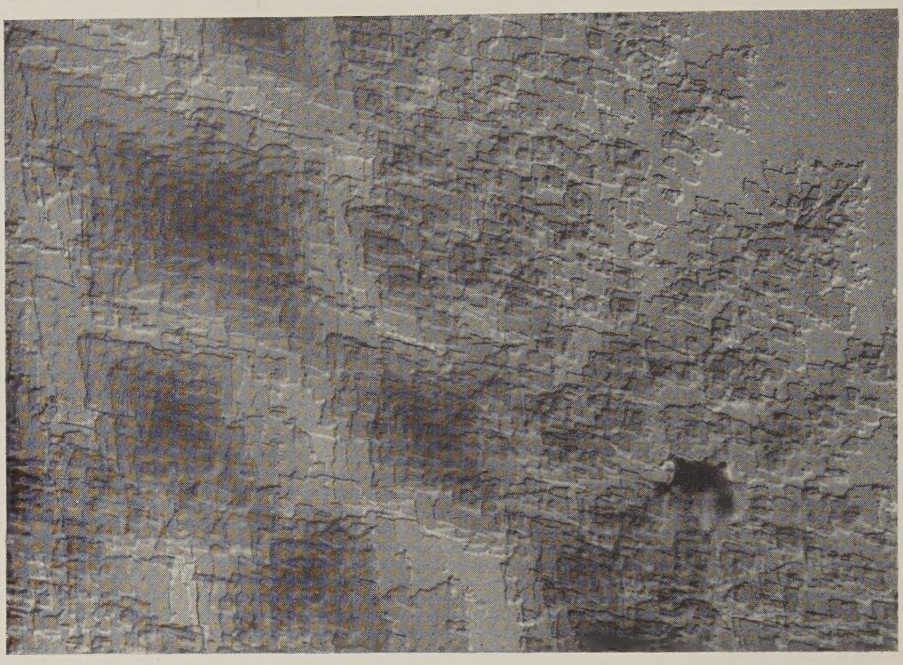

Electron micrograph of the sample as fig. 4, showing more detail. ×10 000, Au–Pd shadowed.

Fig. 6

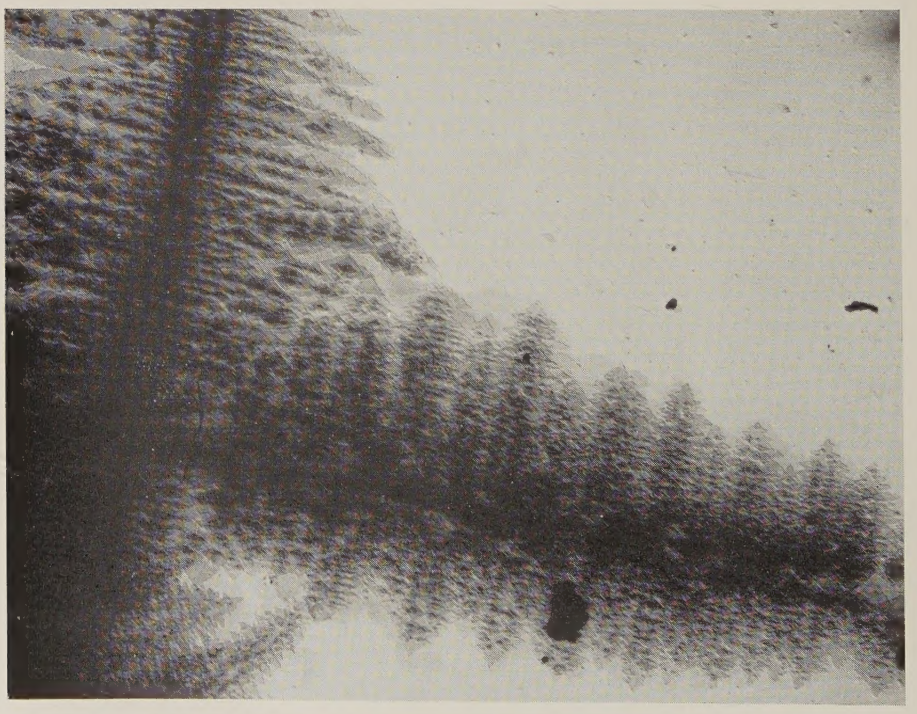

Electron micrograph of Marlex 50. Crystallized in the form of a suspension from 0·03% xylene solution at 69°c. ×3000, Au–Pd shadowed.

Fig. 7

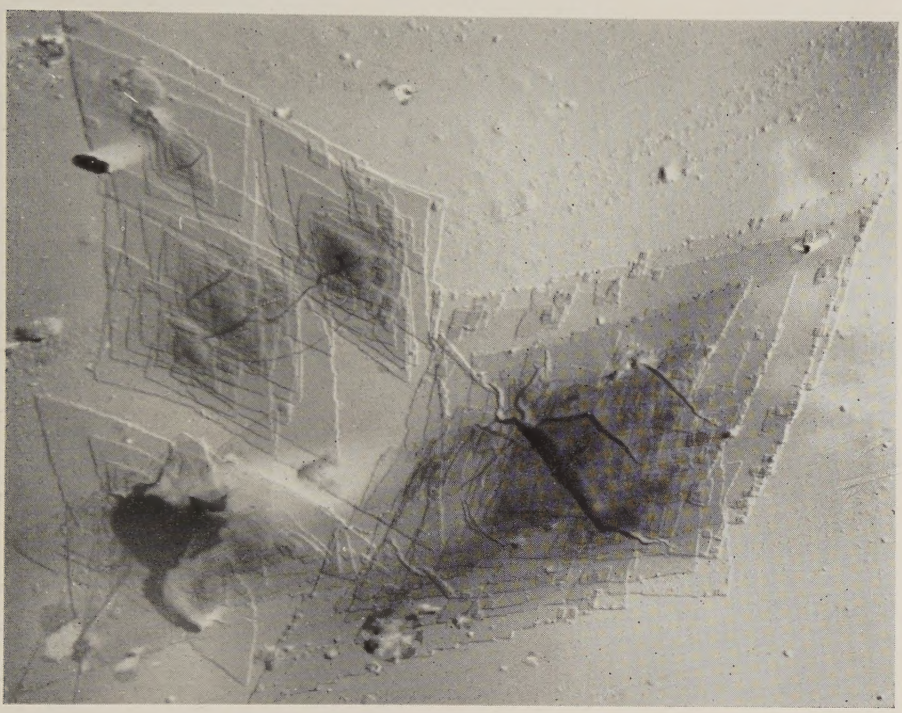

Electron micrograph of Marlex 50. Crystallized in the form of a suspension from 0·1% xylene solution at 89°c. ×4800, Au–Pd shadowed.

Fig. 8

Electron micrograph of different crystals in the same sample as fig. 7. ×20 000, Au–Pd shadowed.

Fig. 9

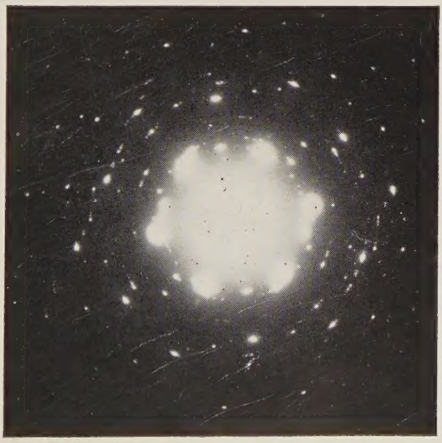

Electron diffraction pattern by the tip of a Marlex 50 dendrite